MULTI-SCALE MORPHOLOGY DEVELOPMENT IN SOLUTION COATED CONJUGATED POLYMERS

BY

GE QU

DISSERTATION

Submitted in partial fulfillment of the requirements
for the degree of Doctor of Philosophy in Chemical Engineering
in the Graduate College of the
University of Illinois at Urbana-Champaign, 2020

Urbana, Illinois

Doctoral Committee:

Assistant Professor Ying Diao, Chair
Professor Jonathan Higdon
Assistant Professor Simon Rogers
Professor Moonsub Shim

Abstract

Interfacial properties play a significant role in solution coating of conjugated polymers. On the one hand, interfacial molecular orientation and alignment critically influence the electronic performance in organic semiconductor thin films. On the other hand, the air-liquid meniscus instability lead to various coating morphology and drives morphology transition during conjugated polymer deposition.

We investigated the out-of-plane molecular orientation influenced by liquid crystalline mesophase and the in-plane crystalline polymer fiber alignment determined by fluid flow from solution coating. For out-of-plane molecular orientation study, we observe distinct edge-on orientation at the top interface compared to primarily face-on orientation at the bottom and the bulk film in solution coated poly[[2,5-bis(2-octadecyl)-2,3,5,6-tetrahydro-3,6-diketopyrrolo[3,4-c]pyrrole-1,4-diyl]-alt-(2-octylnonyl)-2,1,3-benzotriazole] (DPP-BTz) thin films from grazing incidence wide angle X-ray scattering (GIWAXS) measurements. Interestingly, we also observe smectic-like lyotropic liquid crystal mesophase of DPP-BTz appearing during solution coating and adopting edge-on orientation near the air-liquid interface with face-on orientation in the bulk liquid layer, characterized by solution state small angle X-ray scattering (SAXS) and in situ GIWAXS measurements. We attribute the edge-on LC orientation at the top interface to surface energy minimization of alkyl side chains, and the face-on LC orientation in the bulk liquid and bottom interface to symmetry braking effect near the substrate. The out-of-plane molecular orientation is preserved in the LC mesophase and is carried to the solid-state thin film, creating the distinct edge-on interfacial alignment at the thin film top surface. In the in-plane crystalline polymer fiber alignment study, we uncover significantly higher degree of alignment at the top interface of solution coated thin films, using a donor-acceptor conjugated polymer, poly(diketopyrrolopyrrole-

co-thiophene-*co*-thieno[3,2-b]thiophene-*co*-thiophene) (DPP2T-TT) as the model system. At the molecular level, we observe in-plane π-π stacking anisotropy of up to 4.8 near the top interface with the polymer backbone aligned parallel to the coating direction. At the mesoscale, we observe well-defined fibril-like morphology at the top interface with the fibril long-axis pointing towards the coating direction. The high degree of alignment at the top interface leads to a charge transport anisotropy of up to 5.4 compared to an anisotropy close to 1 on the bottom interface. We attribute the formation of distinct interfacial morphology to the skin layer formation associated with high Peclet number, which promotes crystallization on the top interface while suppressing it in the bulk. We further infer that the interfacial fibril alignment is driven by the extensional flow on the top interface arisen from increasing solvent evaporation rate closer to the meniscus front.

For meniscus instability, we first constructed a surface free energy model for speed-dependent film-to-stripe morphology transition, and generated a dimensionless group, morphology number, to describe film-to stripe morphology transition at various coating conditions. We observe a film-to-stripe morphology transition caused by stick-and-slip meniscus instability during solution coating seen in multiple donor-acceptor polymer systems. There is coexistence of film and stripe morphologies at the critical coating speed. Surprisingly, higher charge carrier mobility is measured in transistors fabricated from stripes despite their same deposition condition as the films at the critical speed. To understand the origin of the morphology transition, we further construct a generalizable surface free energy model to validate the hypothesis that the morphology transition occurs to minimize the system surface free energy. As the system surface free energy varies during a stick-and-slip cycle, we focus on evaluating the maximum surface free energy at a given condition, which corresponds to the sticking state right before slipping. Indeed, we observe increase of the maximum system surface free energy with increase in coating speed prior to film-

to-stripe morphology transition and abrupt drop in the maximum system surface free energy post-transition when the coating speed is further increased, which is associated with reduced meniscus length during stripe deposition. Such energetic change originates from the competition between pinning and depinning forces on a partial wetting substrate which underpins the film-to-stripe transition. To move a step further, we utilize meniscus guided solution coating to deposit conjugated polymers with various coating condition to study the meniscus instability driven morphology transition. We solution coated conjugated polymer DPP-TT on various substrate with various coating speed. We observe film-to-strip morphology transition on low surface energy substrates, while coating undergoes transition from evaporation to Landau-Levich regime on medium to high surface energy substrates. We constructed the dimensionless morphology number by multiplying evaporative Peclet number with modified capillary number to quantitatively describe the film-to-strip morphology transition. We observe a distinct decrease in the value of morphology number when film-to-stripe transition occurs. We validate with other coating condition that morphology number is capable of describing film-to-stripe transition, which may help with understanding morphology control in general conjugated polymer coating systems.

Acknowledgments

First and foremost, I want to express my sincere gratitude to my advisor, Professor Ying Diao. Her endless passion and energy in research, education and lifelong learning always inspire and motivate me through my PhD journey. She is a perfect role model not only in research but also in many other aspects in life that I look up to and aspire to approach. I have received tremendous help and support from her whenever I feel lost or lack of motivation. I believe that what I have learned from her will continue benefiting me in my entire life.

I would like to thank the rest of my committee, Professors Jonathan Higdon, Simon Rogers and Moonsub Shim, for reading my thesis, attending my final examination and most importantly, providing valuable feedback on my research. They have kindly served as my preliminary exam committee and gave me precious advice that helped me progress and achieve my goals in research.

Thanks to all the members in Diao Group who are constantly willing to help and discuss research or life matters with each other. One can always find a helping hand when needed or engaged in a quick discussion if any questions arises. Special thanks to my peer and friends Erfan Mohammadi and Hyunjoong Chung, who have been tremendously supportive and helpful in the past five years.

I also want to thank Lingxun for his constant support and encouragement during my PhD period. Finally, I would like to thank my parents and families for their love and support. I will not be able to achieve what I have today without them being by my side. This thesis is dedicated to them.

Table of Contents

Chapter 1

Lyotropic Liquid Crystalline Mesophase Governs Interfacial Molecular Orientation of Conjugated Polymer Thin Films[1]

1.1 Introduction

Solution processable conjugated polymers have been intensively studied as candidates for the next generation electronics owing to their rich chemical diversity and superior properties for fabricating light weight, flexible and high performing electronic devices. As a fabrication method adaptable to industrial scale manufacturing processes, meniscus-guided coating enables deposition of conjugated polymers with abundant tunable coating conditions. Many efforts has been made to design conjugate polymer molecules and modulate solution coating methods to attain desirable molecular structure and charge transport properties.[1, 2] Out-of-plane molecular orientation serves as a critical factor determining the electronic performance of organic electronic devices, which directly affects the ionization potential at the organic semiconductor (OSC) heterojunction interface,[3-5] as well as provides alternative charge transport pathways near the interface.[6, 7] Many methods have been adopted to tune the out-of-plane molecular orientation of organic semiconductors which can be mainly categorized into two groups: tuning molecular interaction and applying external treatment. Tuning molecular interactions includes tuning molecular self-interaction, molecule-solvent interaction and molecule-substrate interaction by molecular design,[8,

---

[1] The contents of this section appear in Qu, G.; Park, K.S.; Kafle, P.; Zhang, F.; Kwok, J.J.; Patel, B.B.; Smilgies, D.-M.; Thomsen, L.; McNeill, C.R.; Diao, Y. “Lyotropic Liquid Crystalline Mesophase Governs Interfacial Molecular Orientation of Conjugated Polymer Thin Films” Submitted to Chemistry of Materials

[9] solution environment selection,[10, 11] substrate modification,[12, 13] or a combination of multiple methods.[14] External treatments include thermal annealing to reach equilibrium morphology,[15, 16]as well as applying electric or magnetic field,[17, 18] Although out-of-plane molecular orientation serves as a critical factor determining the electronic performance of organic electronic devices, a lack of generic understanding and methods of controlling out-of-plane molecular orientation and ordering still remains as a key challenge.

Thermotropic liquid crystalline conjugated polymers have been investigated in the past few decades that thermal treatment is commonly used to induce LC phase transformation and enhance charge transport properties.[19-21] For instance, a commonly studied thermotropic LC conjugated polymer poly(2,5-bis(3-alkylthiophen-2-yl) thieno[3,2-b]thiophene) (pBTTT) shows a LC transition near 150 °C and a melting temperature near 250 °C from differential scanning calorimetry experiments, which an annealing temperature between 150 °C and 250 °C is usually selected for molecular reorganization and mobility enhancment.[19, 22] More recently, lyotropic conjugated polymer come to the attention of the field that lyotropic conjugated polymers enabled one-step solution fabrication of conjugated polymer thin films with superior molecular ordering and high electronic performances.[23-26] Conjugated polymer systems including PCDTPT,[23, 24] P(NDI2OD-T_2),[27] P3ATs,[28, 29] and DTFP based polymers[25, 26] are reported to show lyotropic liquid crystalline properties by utilizing specific solvent and/or molecular design. In the work by Kim et. al, a conjugated polymer is intentionally designed with components of planarized backbone and a geometrically constrained tetrahedral carbon attaching to bulky side chains. Therefore, controlled molecular structure in the designed polymer suppresses strong π-π aggregation and side chain interdigitation, promoting lyotropic LC behavior and resulting in high degree of alignment in the cased thin film compared to control polymers. However, it is believed that most of the donor-acceptor conjugated polymer are not lyotropic LCs. For instance, there is rarely discussion on the lyotropic LC behavior of diketopyrrolopyrrole (DPP) based high performance D-A polymers, and this polymer is most of the time not considered as so. On the other hand, how LC phase determines molecular orientation during meniscus guided solution coating is underexplored. In-plane alignment of lyotropic conjugated polymer has been previously discussed in multiple works.[24, 25, 27, 30] In our recent publication, we observe lyotropic LC mesophase in multiple conjugated polymer systems including poly[3,3'-bis(4-decyl-1-tetradecyl)- 6,6'-bis(thienyl-5-yl)-isoindigo] (PII-2T) and poly[[2,5-bis(2-octadecyl)-2,3,5,6-tetrahydro-3,6-diketopyrrolo[3,4-c]pyrrole-1,4-diyl]-alt-(2-octylnonyl)-2,1,3-benzotriazole] (DPP-BTz).[30] It is shown that the relative flexible backbone of PII-2T and DPP-BTz enables the transition of twist-bend nematic phase to planarized structure induced by fluid flow during solution coating, resulting in drastically different polymer alignment in the thin film.[30] Although recent works has reported the out-of-plane molecular orientation in solution coated lyotropic conjugated polymer thin films,[27, 30] the evolution of LC phase molecular orientation and its correlation with thin film molecular orientation has yet to be discussed. Additionaly, for the few reports of lyotropic LCs, the existance of LC mesophase is demonstrated while the structure of the LC phase is under characterized, which impedes the understanding how the LC structure carries over to the film.In this work, we prepare solution coated DPP-BTz thin films and observe distinct interfacial liquid crystalline mesophase directed out-of-plane molecular orientation in the thin film. We note that lyotropic LC induced in-plane alignment in solution coated conjugated polymer is investigated by our colleagues,[30] and we have previously discussed interfacial in-plane molecular alignment of solution coated conjugated polymer.[31] This work in particular studies the out-of-plane molecular orientation DPP-BTz is a high performance donor-acceptor conjugated polymer with potential high degree in crystallinity and alignment,[32] as well as the capability of adopting various out-of-plane orientation.[33] Characterized by grazing incidence wide angle X-ray scattering (GIWAXS) and near edge X-ray adsorption fine structure (NEXAFS) spectroscopy, DPP-BTz molecules show edge-on orientation at the top interface while residing with face-on orientation in the bulk and bottom interface. We performed solution state small angle X-ray scattering (SAXS) and in situ GIWAXS measurements during solution coating to discover lyotropic liquid crystalline mesophase of DPP-BTz appearing at the meniscus front during solution coating with smectic-like stacking in the liquid crystalline state. Based on our proposed liquid crystalline structure, we elucidate that DPP-BTz liquid crystals have preferred face-on orientation in the bulk and at the bottom of the liquid layer and predominantly edge-on orientation at the top air-liquid interface in the meniscus. Upon further solvent evaporation, the smectic-like liquid crystalline mesophase transfers its structural characteristics into dried polymer films, preserving the out-of-plane molecular orientation distribution. Studying the lyotropic liquid crystalline behavior of conjugated polymers enables new opportunities in understanding complex conjugated polymer assembly process during processing and modulating structure and properties of conjugated polymers at the molecular level.

1.2 Results

In this study, we deposited conjugated polymer thin films of DPP-BTz, onto the substrate using the method of meniscus guided coating (MGC) (**Figure 1.1a**).[30, 31, 34] The thin films are deposited from 10 mg/ml chlorobenzene solution at an elevated substrate temperature of 80 ^{o}C. We performed film deposition on SiO_2 substrate with a speed series from 0.5 mm/s to 100 mm/s to cover the evaporation regime and the Landau-Levich regime.[35] We also coated the films on a series of substrates with various surface energy, including octadecyltrichlorosilane (OTS) treated substrate, poly(vinylidene fluoride-co-hexafluoropropylene) (PVDF-HFP) coated substrate, phenyltrimethylsilane (PTS) treated substrate, (4-vinylphenol) with. 4,4´-(hexafluoroisopropylidene)diphthalic anhydride (PVP-HDA) coated substrate and SiO_2 substrate. We utilized cross-polarized optical microscopy to capture the appearance of mesophase in polymer solution, where misalignment of the average orientation of ordered species with respect of the microscope polarizer and analyzer resulted in the visualization of ordered structures. When monitoring the solution coating process under the cross-polarized microscope, a birefringent band appears at the front of the meniscus (**Figure 1.1b**), which is similar as the previous reported liquid-crystalline mesophase for conjugated polymers.[27, 30] The appearance of bulk lyotropic liquid-crystalline phase is further verified by cross-polarized microscopy measurements of highly concentration DPP-BTz bulk solution at 100 mg/ml (**Figure 1.1c**).

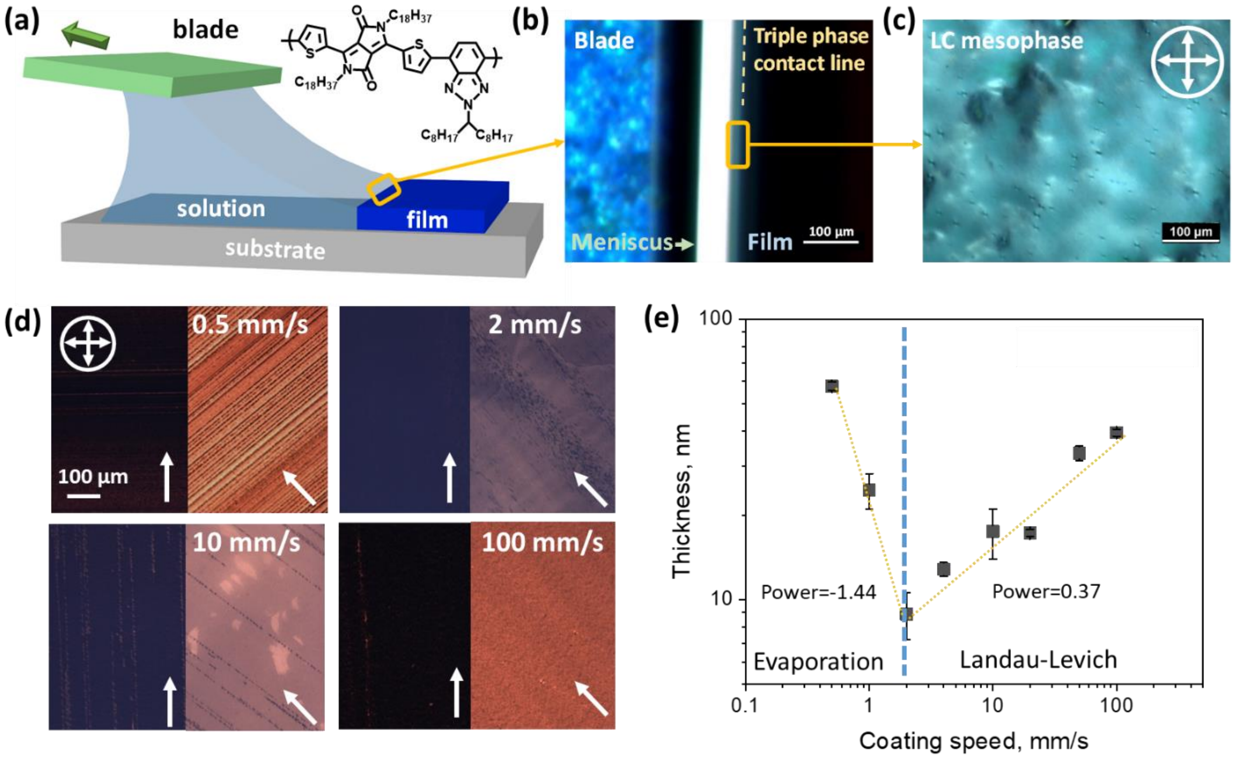

Figure 1.1. Solution coating of DPP-BTz polymer with liquid crystalline phase and speed series on SiO_2 substrate. (a) Schematic of meniscus guided coating of DPP-BTz conjugated polymer. Cross polarized microscopy images of (b) solution coating meniscus front with liquid crystalline phase and (c) high concentration 100 mg/ml solution with bulk liquid crystalline phase are included. The arrows indicate the orientation of the polarizer and the analyzer of the microscope and the scale bars are 100 µm. (d) Cross-polarized microscopy images of DPP-BTz thin films coated on SiO_2 substrates at 0.5 mm/s, 2 mm/s, 10 mm/s coating speed. The arrows indicate the coating direction. The cross refers to the orientation of the polarizer and the analyzer of the microscope. (e) Correlation between coated film thickness and coating speed. The black squares are experimental data and the dotted lines are fitted trend lines for thickness-coating speed relationship at the evaporation and Landau-Levich regimes.

To study the evolution of out-of-plane molecular orientation in DPP-BTz thin films, we perform DPP-BTz thin film deposition in a coating speed series ranging from 0.5 mm/s to 100 mm/s on SiO_2 substrates. Microscopy images are taken when the coating direction of the samples are oriented 0^o and 45^o with respect to the either the polarizer or the analyzer to observe birefringence and to infer alignment of crystalline domains (**Figure 1.1d**). The birefringence between the 0^o and the 45^{o} images indicated moderate in-plane polymer backbone alignment within the coated film, which will be discuss in following contents. The atomic force microscopy (AFM) measurements at the cross section of the films show the decreased and then increased film thickness. The film thickness follows a power-law dependence with respect to the coating speed, which can be divided into two regimes (**Figure 1.1e**).[35] The low speed evaporation regime is governed by mass transport from evaporation driven capillary flow, where the film thickness decreases with increasing coating speed. The high speed Landau-Levich regime is dominated by viscous force dragged convective flow, where film thickness increases with increasing coating speed. In this case, the transition coating speed is at 2 mm/s with the lowest film thickness at 8.9 nm. The data points in both evaporation regime and Landau-Levich regime is fitted to obtain the power-law exponent. The exponent in the evaporation regime is -1.44 and in the Landau-Levich regime is 0.37, both deviated from the theoretical value of -1 and 0.67, respectively.[35] The difference between the experimental and the theoretical may result from the non-ideal conditions during solution coating, such as partial wetting and stick-slip instability,[36] Marangoni flow,[35] skin layer formation,[31] and dependence of assembly pathways (and therefore viscosity) on coating regimes,[30] etc.

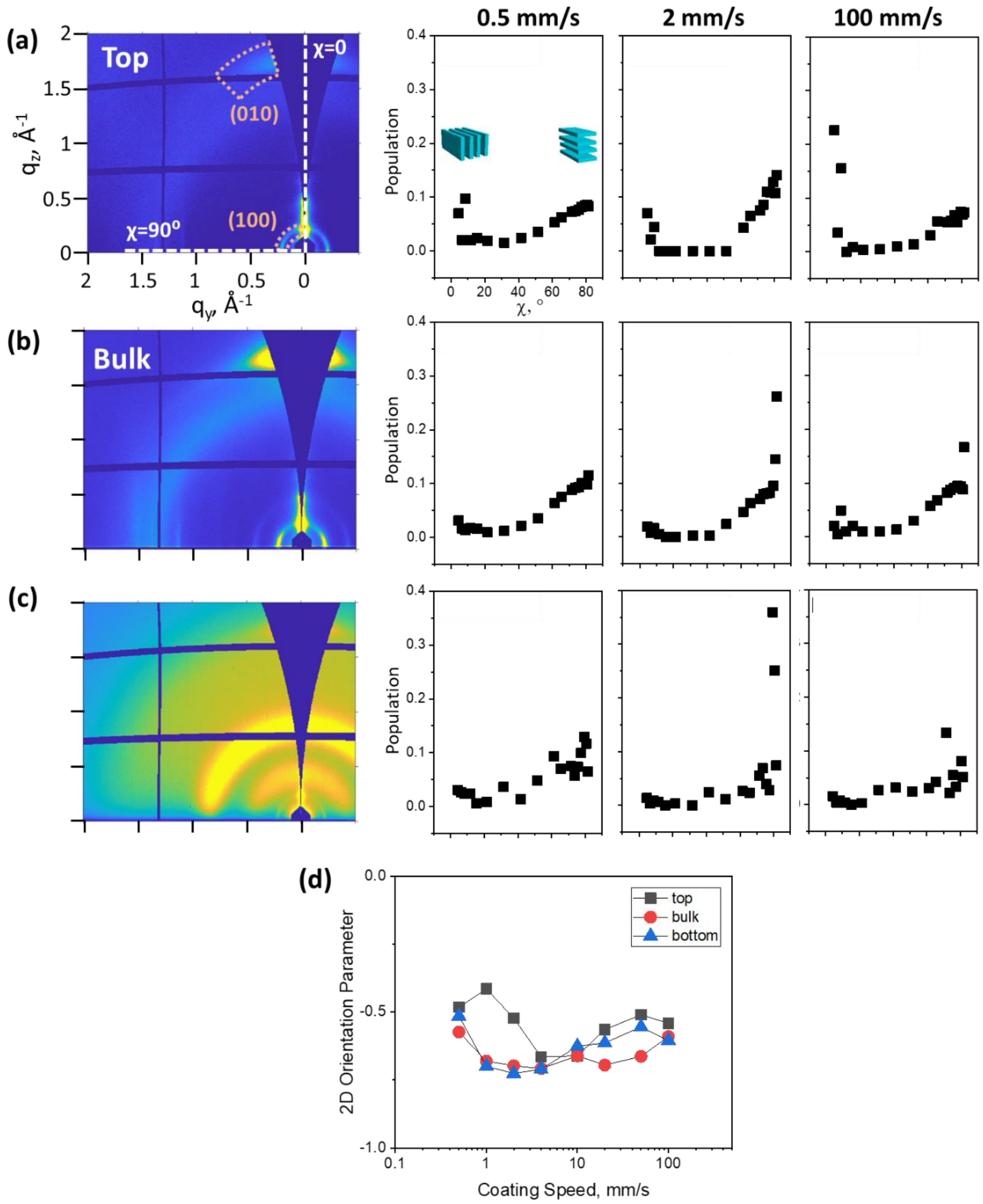

Figure 1.2. Grazing incidence X-ray 2D patterns for films coated at 0.5 mm/s and partial pole figures results for films coated at 0.5 mm/s, 2 mm/s and 100 mm/s for (a) top interface, (b) bulk film and (c) bottom interface. Measurements are taken with the incident beam perpendicular to the coating direction. (d) Out-of-plane 2D orientation parameter from GIWAXS measurements at various coating speeds.

We perform partial pole figure analysis from the GIWAXS 2D scattering patterns to quantitatively analyze the out-of-plane molecular orientation of DPP-BTz polymers in the thin film. Measurements of the interfaces and the bulk film are differentiated by varying the incident angle of the X-ray beam, 0.04^o for interfacial measurements and 0.14^o for bulk measurements. The 0.14^o incident angle is slightly above the critical angle for total reflection at the polymer/air interface, yielding a penetration depth of the complete film thickness, while the shallow 0.04^o incident angle gives a penetration depth of 8 nm, approximately 3-4 molecular layers.[37] Bulk film and top interface measurements are directly performed on the thin films coated on the SiO_2 substrates. For bottom interface measurements, inverted films are prepared on a PDMS support by peeling the films with PDMS from SiO_2 substrates after soaking the system in ACN overnight, see details in methods. The GIWAXS 2D patterns for the top interface, bulk film and the bottom interface of films coated at 0.5 mm/s are shown in **Figure 1.2a-c**. The (100) lamellar stacking peak is analyzed to construct the partial pole figures and quantify the out-of-plane polymer orientation in the crystalline domains. The (100) peak is chosen because it has high intensity and narrow peak width in the χ=0-90^o range compared to the (010) peak, and is less affected by the "forbidden zone" after geometric correction, as shown in the GIWAXS patterns in **Figure 1.2a-c**. The partial pole figures are obtained by plotting the (100) lamellar peak intensity from 1^o sector cut profiles on the geometrically corrected scattering patterns within the range of 4^o<χ<82^o. Small degree sector cut is performed to ensure more accurate representation in population of oriented crystllites at specific χ angles in the pole figures and for later calculation. For the (100) lamellar stacking peak, intensity near χ=0^o corresponds to edge-on crystallites and intensity near χ=90^o corresponds to face-on crystallites. The peak intesnites are normalized to the 0-1 scale for direct comparison of the polymer orientations across different coating speed and interfaces/bulk film. The selected pole figures in **Figure 1.2** at 0.5 mm/s, 2 mm/s and 100 mm/s represent the thin film out-of-plane orientation in the evaporation regime, transition point and Landau-Levich regime, respectively (complete set of pole figures in **Appendix**). At the top interface, sharp rise of intensity near $\chi=0^o$ reveals the presence of edge-on crystallites, with the highest population observed at the highest coating speeds of 50-100 mm/s. However in the bulk film and at the bottom interface, sharp increase in intensity is instead observed near $\chi=90^o$ corresponding to face-on crystallites. The highest intensity at $\chi=90^o$ for bulk film and bottom interface appears at 4 mm/s, near the 2 mm/s transition point. Overall, from the pole figure analysis we observe distinct edge-on crystallites residing at the top interface of the film, as compared to the predominance of face-on crystallites at bulk film and bottom interface. The degree of out-of-plane orientation from GIWAXS measurements is quantified in terms of 2D orientation parameter $S_{2D} = 2 < \cos^2 \gamma > -1$, where γ is the tilt angle of the conjugated backbone with respect to the susbtrate (**Figure 1.2d**).[32, 38, 39] With a scale of S_{2D} between -1 to 1, S = 1 indicated a completely edge-on orientation, S = 0 an isotropic orientation and S = -1 a completely face-on orientation. Detailed calculation of S_{2D} is included in the Supporting Information. S_{2D} from GIWAXS of top interfaces, bulk film and bottom interfaces all concentrate within the range of -0.5 to -0.8 corresponding to preferred face-on orientation, with a moderate coating speed dependence. The S_{2D} of the top interface is closer to zero (less face-on) compared to S_{2D} of the the bulk and the bottom interface, due to the emergence of edge-on crystallites at the top interafce. The lowest value of S_{2D} occurres at 4 mm/s near the transition speed, where the film is as thin as 12.8±0.7 nmpossessing a relatively homogeneous out-of-plane molecular orientation.

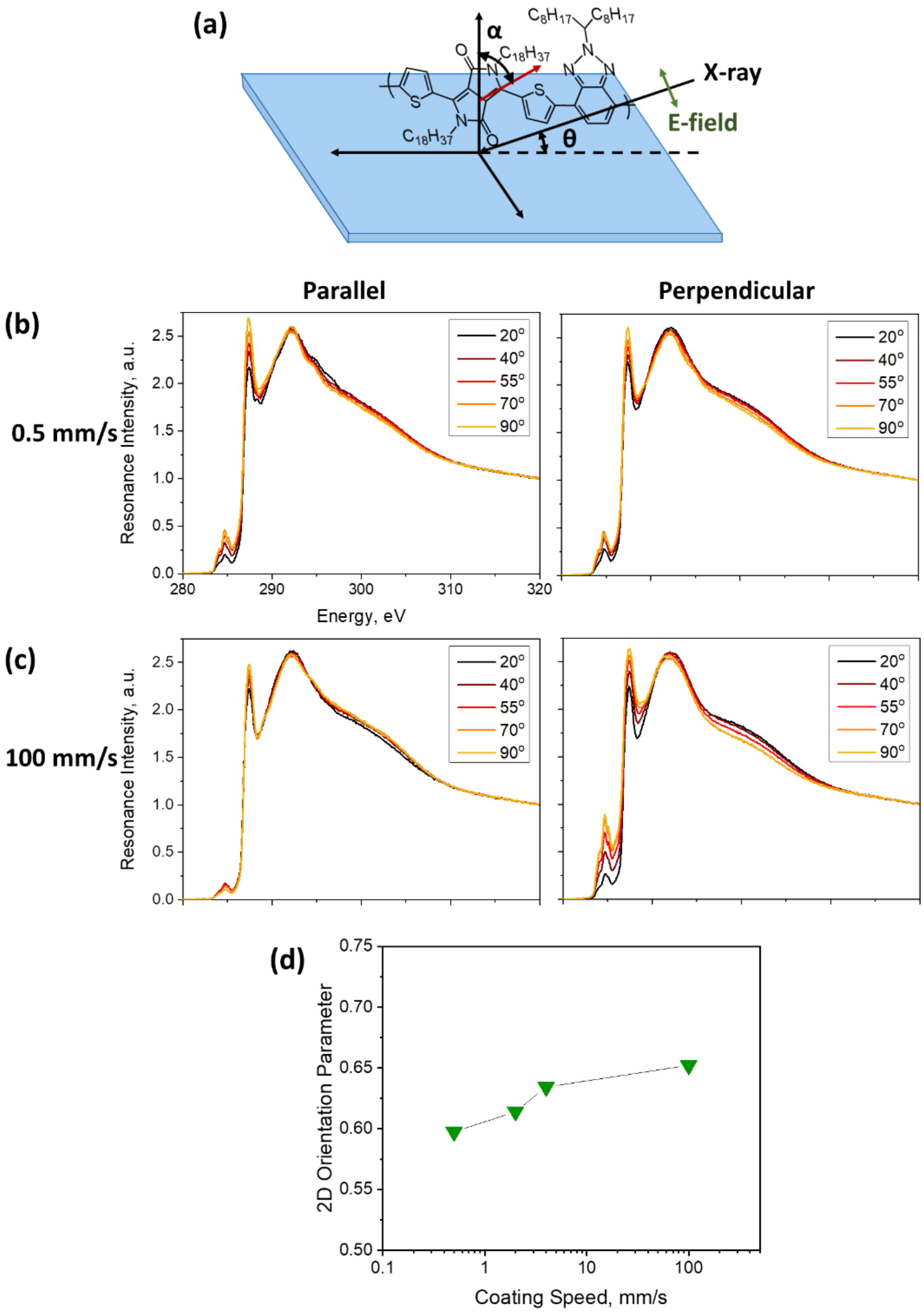

Figure 1.3. Angle resolved NEXAFS measurement illustration and results. (a) Illustration of NEXAFS measurements of DPP-BTz polymer with the incident angle θ using a polarized X-ray beam. The angle between transition dipole moment of the DPP-BTz molecule with respect of substrate normal is α. Angle resolved NEXAFS spectra with the X-ray beam parallel and perpendicular to coating direction at (b) 0.5 mm/s and (c) 100 mm/s are showed. (d) Out-of-plane 2D orientation parameter from NEXAFS measurements at various coating speeds.

We utilize NEXAFS spectroscopy as a powerful tool to reveal the out-of-plane molecular orienation with high surface sensitivity. Incident angle resolved NEXAFS measurements with a polarized X-ray beam is used to probe the K-shell electron C1s-π* resonance and collect angle-dependent absorption spectra. Because the transition dipole moment of the C1s-π* resonance is orthogonal to the the conjugated plane on the polymer backbone, the orientation of the conjugated polymer backbone is determined by analyzing the C1s-π* intensity obtained from multiple tilt angle θ scans (**Figure 1.3a**). Unlike GIWAXS, NEXAFS mesurements do not distinguesh crystalline or amorphous regions, giving averaged molecular orientation information contributed by all polymers.

Tilt angle NEXAFS scans are performed at incident angles 20^{o}, 40^{o}, 55^{o}, 70^{o} and 90^{o}, with the incident X-ray beam both parallel and perpendicular to the coating direction. NEXAFS measurements are operated under the partial electron yield mode, probing the top 3 nm of the thin film (~ 1 molecular layer). **Figure 1.3b and c** show example spectra of tilt angle measurements on film coated at 0.5 mm/s and 100 mm/s with the X-ray beam both parallel and perpendicular to coating direction. Complete set of NEXAFS spectra from 0.5 mm/s, 2 mm/s, 4 mm/s and 100 mm/s films are included in **Figure A2a-d**. For quantitative analysis, the intensity of the C1s-π* resonance peak at 285 keV is analyzedAt 0.5 mm/s, the angle resolved NEXAFS scans are similar in parallel and perpendicular measurmeents, with increasing intensity from 20^{o} to 90^{o}. On the other hand, at 2 mm/s, 4 mm/s and 100 mm/s the angle resolved spectra from parallel scans nearly overlay, but spectra from perpendicular scans show significant angle dependence. It is because the intensity variation of the C1s-π* resonance depends on the relative alignment between the polarized X-ray beam with respect of the TDM of the molecule. In a biaxially aligned film, maximun degree of TDM variation occurs in the direction orthogonal to the polymer backbone, where TDM is orthogonal to substrate normal in edge-on molecules and along substrate normal in face-on molecules. Therefore, minimun angle-dependent signal in parallel measurements and significantly angle-depnednt signal in perpendicular measurements indicate a preferred in-plane polymer backbone orientation along the coating direction. The dichroic ratio calculated by $DR_{NEXAFS} = \frac{I_{90°,perp} - I_{90°,par}}{I_{90°,perp} + I_{90°,par}}$ incrased from 0 at 0.5 mm/s to 0.78 at 100 mm/s **(Figure A2e)**, showing increasing degree of in-plane alignment at the top interface with increasing coating speed. Further discussion on in-plane alignment is included in the following content.

Information of out-of-plane molecular orientation embeds in the angle resolved NEXAFS spectra, particularly in perpendicular measurmenets. The strongest resonance signal occurred when the linearly polarized X-ray beam aligned with the TDM of the C1s-π* resonance. Therefore, a strongest C1s-π* intensity with $\theta=90^{o}$ indicated a predominate TDM orientation parallel to the substrate, in other words, a primarlly edge-on orientation of the polymer molecules. Because increasing C1s-π* intensity with incident angle θ changing from 20^{o} to 90^{o} occurs in all experimental conditions (**Figure A2**), DPP-BTz at film surface adopts primarlly edge-on orientation. Similar as in GIWAXS, the out-of-plane molecular orientation in terms of 2D orientation parameter S_{2D} can be evaluated. Due to the biaxial alignment of DPP-BTz in thin film, calculation of S_{2D} requires angle resolved NEXAFS spectra from both parallel and perpendicular measurements.[40] Fitting parameters are obtained from the intensity of C1s-π* resonance and the average out-of-plane orienration $< \cos^2 \alpha >$ in terms of TDM tilt angle α with respect of substrate normal is calculated to obtain $S_{2D,\ NEXAFS}$ (details in method section). The value of S_{2D} increased from 0.60 to 0.65 when coating speed changes from 0.5 mm/s to 100 mm/s, indicating minor coating speed dependence of the degree in edge-on orientation for DPP-BTz polymer at film surface.

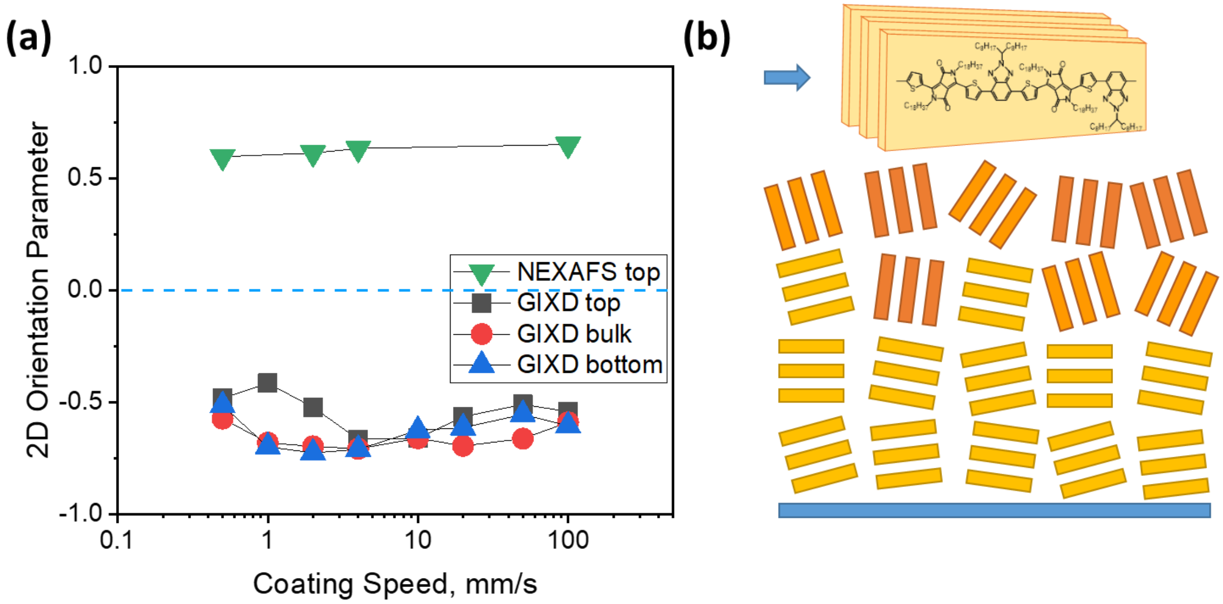

Figure 1.4. Out-of-plane 2D orientation parameter and the corresponding morphology. (a) Combined plot for 2D orientation parameter S_{2D} calculated from GIWAXS and NEXAFS measurements. (b) Illustration of out-of-plane molecular orientation of DPP-BTz thin films from various coating speeds. The rectangles are side view of DPP-BTz crystallites along the backbone direction with π-π stacking in between.

Combining the out-of-plane 2D oreintation parpameter S_{2D} from both GIWAXS and NEXAFS results in **Figure 1.4a** (tabulated in **Table A1**), it is clear that S_{2D} from GIWAXS measurements (-0.41 to -0.72) at top interface, bulk film and the bottom interface is contributed by face-on crystallites in the overall films, while S_{2D} from NEXAFS measurements (0.60 to .65) at the top interfaceis is resulted from a thin layer of edge-on crystallites. The large discrepency between the top surface S_{2D} values from GIWAXS (-0.41 to -0.76) vs. NEXAFS (0.60 to 0.65) might come from the different penetration depth of the X-ray beam (~8 nm vs. ~3 nm). With the S_{2D} analysis from both GIWAXS and NEXAFS, the illustation of the out-of-plane molecular morphology is shown in **Figure 1.4b** The polymer molecules resided with edge-on orientation at the very top interface of the thin film, while the bulk and the bottom interfaces are consisted of face-on polymers, agreeing with literature findings.[27, 41, 42]

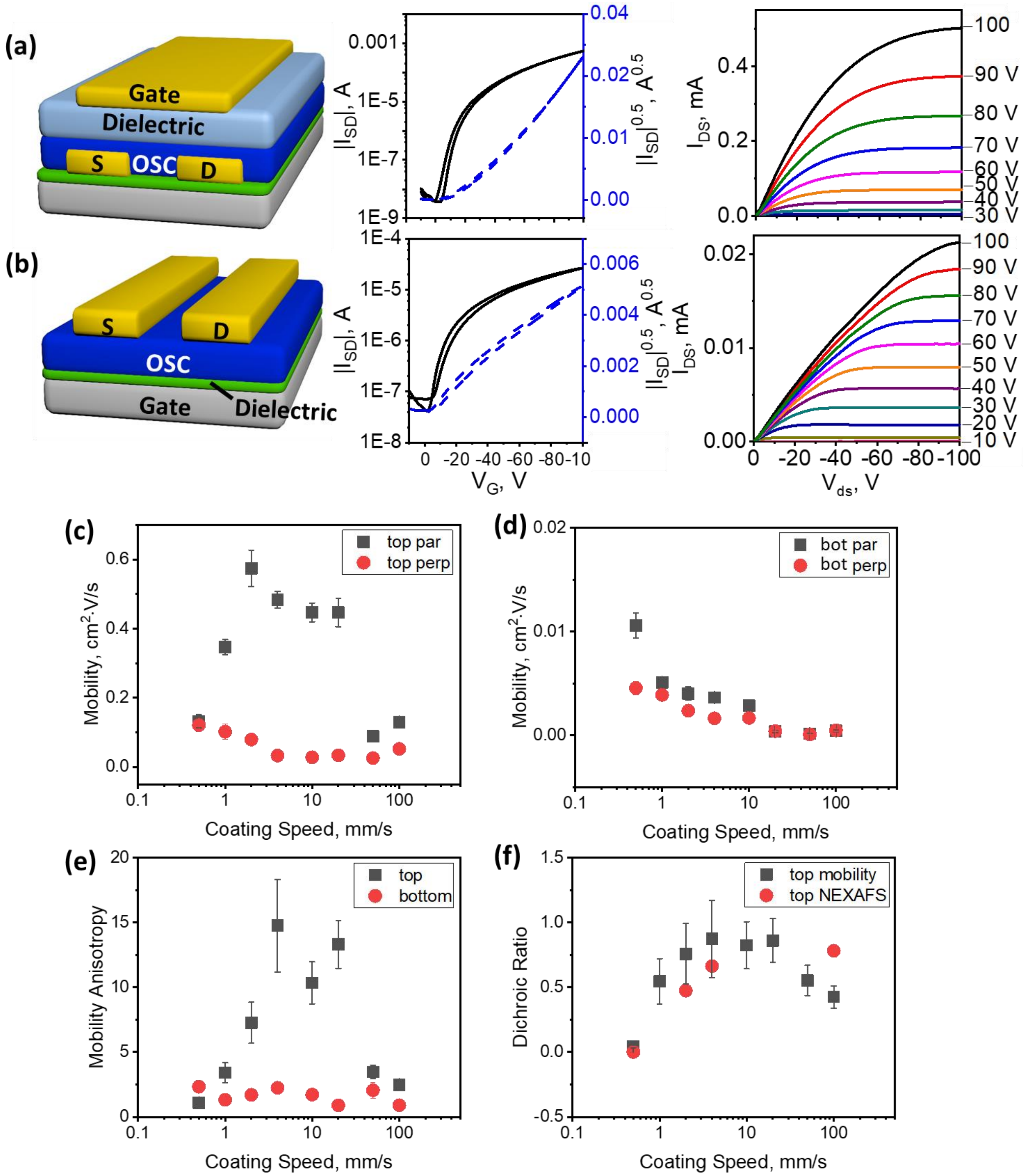

Figure 1.5. Field effect transistor device configuration, saturation regime transfer curves and output curves for (a) top interfacne and (b) bottom interface charge transport characteristic measurements. The charge transport mobilities at (c) top interface and (d) bottom interface with the transport direction parallel and perpendicular to coating direction. (e) In-plane charge transport mobiligy anisotropy calculated by the ratio of parallel versus perpendicular mobility at the top and the bottom interface. (f) Comparison of dichroic ratio between charge trasnposrt mobility and backbone alignment from NEXAFS measurements at the top interface.

Additionaly, we fabricate field-effect transister devices to measure the charge transport mobility at the top and the bottom interface, respectively. We constructed top gate bottom contact (TGBC) for top interface measuremts and bottom gate top contact (BGTC) for bottom interface measurements (**Figure 1.5a and b**). The field effect mobility μ_{sat} is calculated from the transfer curves obtained from measurements at the saturation regime. Devices with their channel length parallel and perpendicular to the coating direction are fabricated to evaluate the charge transport anisotropy, which is defined by μ_{par} over μ_{perp}. The characteristic transfer and output curves comparinting TGBC and BGTC devices and the extracted top and bottom interface mobilities are shown in **Figure 1.5a and b**. The majority of the charge transport mobility at the top interface is larger than that at the bottom interface with a highest charge transport mobility from top interface at 0.57 $cm^2 \cdot V/s$ and from bottom interface only at 0.011 $cm^2 \cdot V/s$ (**Figure 1.5c and d**). However, because different delectric is used for top interface (440 nm polymethyl methacrylate) and bottominterface (300 nm SiO_2) device fabrication, charge transport moblity from the two interfaces are not directly comparable due to different charge densities.

On the other hand, the top interface exibits significantly higher charge transport mobility in the parallel orienration, yielding a high charge transport anisotropy compared to the bottom interface. The highest charge transport mobility at the top interface 0.57 $cm^2 \cdot V/s$ occurs at the transition speed 2 mm/s, which may come from highly aligned polymer backbong at the top interface. The bottom interfae shows almost no charge transport anisotropy, suggesting less in-plane ordering at the bottom interface. The charge transport anisotropy is calculated as $A = \mu_{par}/\mu_{perp}$ and is shown in **Figure 1.5e**. The top surface, specifically near transition speed 2 mm/s with A = 14.7, exhibits highly preferred transport along the coating direction with. Bottom interface shows nearly isotropic charge transport at most of the coating speeds with a highest anisotropy A = 2.3 at 0.5

mm/s. The dichroic ratio of charge transport can be calculated from the anisotropy $DR_{transport} = \frac{A-1}{A+1}$ and to compare with the previous dichroic ratio of polymer backbone alignment from NEXAFS. For charge transport, DR = 1 indicates completely prefered charge transport along coating direction and DR = -1 for completely preferred transport orthogonal to coating. When plotting together the DR from top surface charge transport and NEXAFS in **Figure 1.5f**, the trend similarly overlapps with DR ≈ 0 at 0.5 mm/s and incrasing DR at 2 mm/s and 4 mm/s, which suggests faster charge transport along the polymer backbone at the top interface agreeing with our previous work.[31] The increasing backbone alignment with coating speed from NEXAFS is contributed by increase of extensional strain rate near the menicus at the contact line.[30] Meanwhile the charge transport mobility and anisotropy are affected by multiple factors such as molecular aligment, crystallinity, tie chains, etc, causing the descripancy in DR between mobility anisotropy and alignment from NEXAFS at 100 mm/s. Further discussion on in-plane alignment is beyond the scope of this manuscript and thus not included.

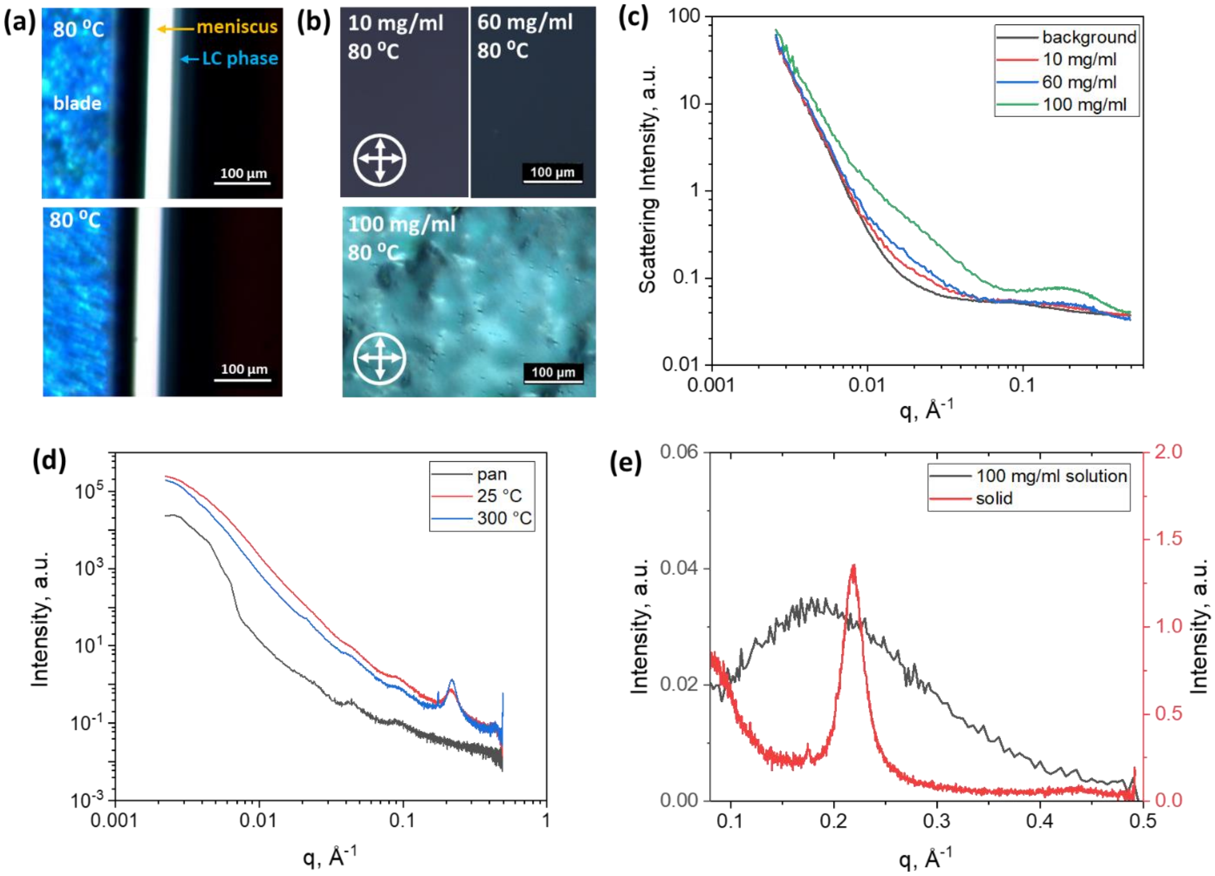

Figure 1.6. Lyotropic liquid crystalline mesophase revealed by microscopy and solution SAXS measurements. (a) Cross-polarized microscopy images of the bulk liquid crystalline mesophase of DPP-BTz in chlorobenzene with 10 mg/ml, 60 mg/ml and 100 mg/ml concentrations at 80 ºC. (b) In situ cross-polarized microscopy of the meniscus during solution coating of 10 mg/ml DPP-BTz in chlorobenzene solution on SiO_2 substrates at 80 ºC with 1 mm/s coating speed. (c) Solution state SAXS 1D scattering profile of chlorobenzene background, 10 mg/ml, 60 mg/ml and 100 mg/ml DPP-BTz in chlorobenzene solution at 85 ºC. (d) Solid state SAXS 1D scattering profile of aluminum pan background and DPP-BTz polymer solid at 25 ºC and 300 ºC. (e) Background subtracted SAXS 1D profile of 100 mg/ml DPP-BTz solution and DPP-BTz solid within the q range of 0.09 to 0.5 Å^{-1}, highlighting the LC smectic peak of solution and the (100) lamellar stacking peak of solid.

After determining the solid state out-of-plane molecular orientation of DPP-BTz thin films, we performed solution state measurements at high concentration and in situ measurements during coating to understand the evolution of DPP-BTz assembly process when the film is drying. We first record the top view meniscus movement under cross polarized microscopy. Interestingly, we observe the appearance of a birefringent blue colored band at the front of the meniscus (**Figure**

1.6a), similar as the liquid crystalline (LC) mesophase observed in other conjugated polymer systems.[27, 30] The birefringent blue band traces the movement of the meniscus, which belongs to the highest concentration region of the meniscus from solvent evaporation. It is because the solution concentration increases rapidly from the bulk to the triple phase contact line due to solvent evaporation,[30] reaching the critical concentration for the appearance of liquid crystalline mesophase. To determine the presence of LC mesophase and its concentration range, DPP-BTz solution in chlorobenzene at high concentration is made and inspected under cross-polarized microscope (**Figure 1.6b**). We find that bulk LC mesophase is visible at 100 mg/ml, as compared to no LC texture from 10 mg/ml and 60 mg/ml. One signature of the LC mesophase is its birefringence when rotating the sample. Therefore, we deduce that DPP-BTz undergoes LC mesophase during solution coating when chlorobenzene evaporation occurs and concentration approaches near 100 mg/ml. The structure and the orientation of the LC mesophase may influence the final out-of-plane orientation of the conjugated polymer in thin film state.

We perform solution SAXS measurements to understand the molecular ordering and structures of the LC mesophase of DPP-BTz in chlorobenzene. The polymer solution is placed in a quartz capillary on a heating stage to run transmission SAXS experiments at various temperatures. In **Figure 1.6c**, a broad peak arises in the range of $q = 0.1 – 0.5$ Å^{-1} in the SAXS 1D profile for 100 mg/ml DPP-BTz solution, distinct from the scattering intensity of the background and low concentration samples. The broad peak centers at 0.191 Å^{-1}, corresponding to a d-spacing of 32.9 Å assuming the predominant contribution from the structure factor. Given that this peak lies in the range of the solid state lamellar stacking peak, we perform transmission SAXS measurements to directly compare the two. Specifically, we pack DPP-BTz solid in a press-sealed thermogravimetric analysis (TGA) aluminum pan and perform SAXS scans at 25 ºC and 300 ºC

(**Figure 1.6d**). The (100) lamellar stacking peak is much sharper, centering at q = 0.219 Å^{-1} which is insensitive to temperature. The lamellar stacking peak distance is calculated to be 28.7 Å, agreeing with literature values.[32, 43] Given the close proximity with the (100) lamellar stacking peak (**Figure 1.6e**), we attribute the origin of the 0.191 Å^{-1} peak at 100 mg/ml DPP-BTz solution to smectic-like ordering in the LC mesophase. The smectic-like layers in the LC mesophase have a spacing of 32.9 Å at the meniscus front during deposition, and evolves into lamellar stacking with 28.7 Å distance in dried film and at the same time sharpens as the paracrystalline disorder drastically reduces from the LC phase to the solid state. To further explore the ordering in LC mesophase from solution SAXS results, we utilize Kratky analysis by plotting $q^2I(q)$ against q, where the trend of the Kratky plot correlates to the shape of polymers in the solution (**Figure A3**). Two distinct peaks arise from the Kratky plot, one in the q = 0 – 0.1 Å^{-1} range and the other in the q = 0.1 – 0.5 Å^{-1} range. We have discussed in the above content that intensity above q = 0.1 Å^{-1} come from the smectic ordering in the LC mesophase. Therefore, the peak at q = 0 – 0.1 Å^{-1} reflects structure or ordering in the larger lengthscale than the smectic ordering, with a peak position at q = 0.03 Å^{-1}. The peak position corresponds to a length in d = 210 Å^{-1}, which may be a characteristic length along the polymer backbone in the LC mesophase.

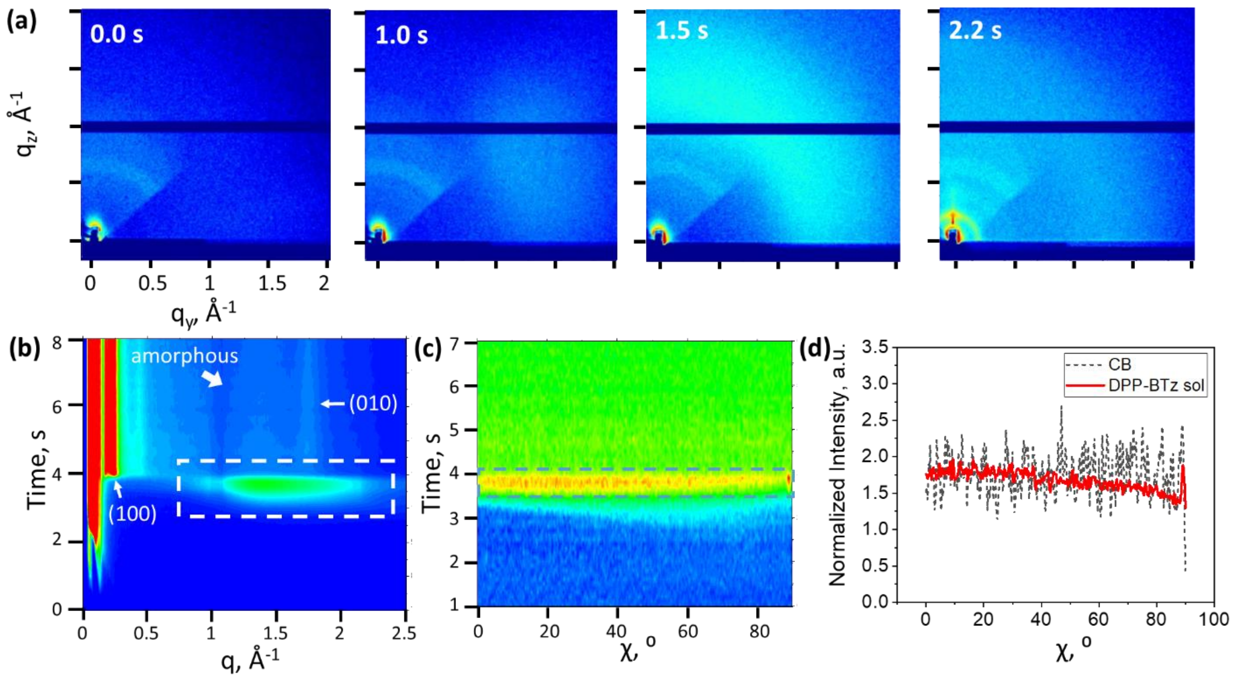

Figure 1.7. (a) Evolution of scattering peaks from in situ μGIWAXS measurements during solution coating of 5 mg/ml DPP-BTz at 0.5 mm/s at 70 °C on SiO_2 substrates. The same conditions apply to (b-d) (b) The intensity-time-q plot with $\chi = 0 - 90^{o}$. This plot shows the evolution of peaks with respect to time across the range of q values. Peak locations are determined from this plot. (c) The normalized intensity-time-χ plot for $q = 0.8 – 0.95$ Å^{-1}. This plot shows the χ angle-dependent intensity distribution of the transient halo centered at 1.45 Å^{-1} evolving with respect of time. The q range is selected to be $q = 0.8 – 0.95$ Å^{-1} instead of near 1.45 Å^{-1} to avoid the effect of gap in detector on scattering intensity. The y-axis time scales in (b) and (c) are the same for direct comparison. (d) Dependence of the transient halo scattering intensity on the χ angle comparing the cases of the neat chlorobenzene solvent and the 5 mg/ml DPP-BTz solution.

In situ micro grazing incidence wide angle X-ray scattering (μGIWAXS) measurements are performed during solution coating of DPP-BTz on SiO_2 substrates with the incident X-ray beam perpendicular to the coating direction. In previous content, we determined partial of the structure of LC mesophase from solution SAXS. To obtain the orientation distribution of LC mesophase and correlate that to solid state X-ray results, we utilize in situ GIXD measurements. The validity of studies from X-ray measurement perpendicular to coating is illustrated in **Figure A5** that similar out-of-plane molecular orientation distribution comes from both parallel and perpendicular measurements in thin film state. Specifically in μGIWAXS, the X-ray beam is focused with a microcapillary into 40 μm beamwidth for high spatial resolution during in situ X-ray measurements without compromising the signal-to-noise ratio.[44] In the scattering video, a broad transient halo centered at q = 1.45 Å^{-1} first emerges from the horizon and forms a complete ring. Subsequently, this halo disappears as the π-π stacking peak and the lamellar stacking peaks emerge. **Figure 1.7a** comprises of time-lapsed snapshots of the scattering video showing the background, the rise of the transient halo, the complete transient halo, and the appearance of the stacking peaks when the halo disappears. In order to better visualize and analyze the in situ μGIWAXS data, an intensity-time-q plot is constructed for coating of DPP-BTz solution at 0.5 mm/s, highlighting evolution of important peaks including the transient halo, the (100) lamellar stacking peak, the (010) π-π stacking peak and the amorphous peak (**Figure 1.7b**). The broad transient halo (q of 1~2 Å^{-1}) appears around 3 second and disappears at 4 second, followed by the rise of the (100) peak (q = 0.22 Å^{-1}), the (010)peak (q = 1.75 Å^{-1}) and the amorphous peak (q = 1.44 Å^{-1}) after 4 seconds. A transient halo also appears when coating pure chlorobenzene solvent on the substrate. However, the scattering intensity is 30 times weaker than the case of coating DPP2T-TT chlorobenzene solution. Because an LC mesophase is observed at the meniscus front during solution coating (**Figure 1.6a**), the scattering intensity is expected to have contributions from the LC mesophase in this q range, that the average spacing between LC directions is expected to give comparable intensity as the amorphous peak in solid state.[30] To validate this point, we make the normalized intensity-time-χ plot to determine the intensity distribution of the transient peak over the χ angle (**Figure 1.7c**). Such a plot can help differentiate the anisotropic scattering of the LC mesophase (χ angle dependent) from the isotropic scattering of the solution (χ angle independent). The polar angle χ on the scattering pattern is defined as χ = 0 for the vertical and χ = 90° for the horizontal direction. In the intensity-time-χ plot for coating of DPP-BTz solution, the intensity of the transient peak at its maximum has uneven distribution across χ = 0-90^{o}. The intensity is high in the χ = 0-50^{o} range and decreases between χ = 50^{o}-85^{o}, and then a sharp peak appears near χ = 90^{o}. This indicates that the species contributed to the transient halo scattering has preferred out-of-plane orientation distribution because pure solution should result in isotropic scattering intensity (**Figure A4a**). A more direct comparison by plotting the linecut at the maximum intensity from the intensity-time-χ plot is shown in **Figure 1.7d** for pure solvent vs, DPP-BTz solution. The chlorobenzene data is noisy because of the low intensity of pure solvent scattering, but still shows homogeneous distribution over χ. Meanwhile the DPP-BTz solution coating intensity distinctly decreases between χ = 50^{o}-85^{o}, leaving a overall high intensity between χ = 0-50^{o} and a sharply peaked intensity at χ = 90^{o}. We believe that solvent and solvated polymer resulted in isotropic intensity distribution in the transient peak, but at the same time LC mesophase with specific out-of-plane orientation gives rise to the anisotropic intensity distribution. The structure origin of the χ angle-dependent intensity with higher intensity at low χ range and the sharp intensity peak near χ = 90^{o} will be discussed in following content.

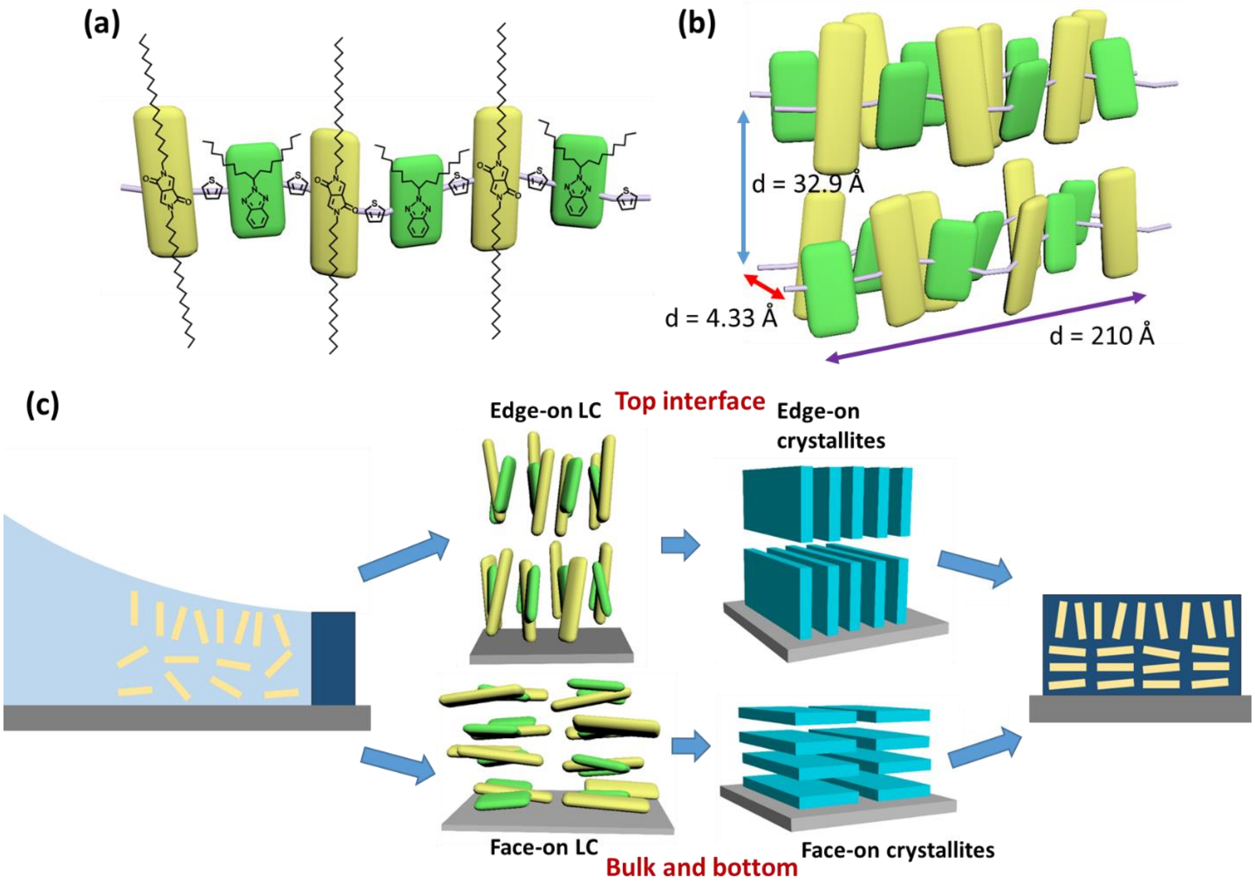

Figure 1.8. (a) Liquid crystalline structure with LC directors orthogonal to the polymer backbone. The yellow and green bars represent the LC directors from DPP units and BTz units. (b)Smectic-like liquid crystalline stacking with average director distance of 4.33 Å, layer distance of 32.9 Å and characteristic length along the backbone of 210 Å. (c) DPP-BTz assembly through liquid crystalline mesophase with distinct out-of-plane orientation at the top vs. the bulk and the bottom interface. The yellow rectangles represent the side view of polymer backbone.

Based on solution state SAXS data and in situ μGIWAXS data, we propose the DPP-BTz liquid crystalline structure and the mechanism by which the LC mesophase determines the interfacial orientation in the solid thin film. We assign the LC directors to be along the short axis of the polymer backbone that each DPP or BTz unit represent one director (**Figure 1.8a**). This assignment of LC director is inline with the conventional small molecule LC mesogens consisting of rigid rod-like segment attached with flexible alkyl chains. The average spacing between the directors are obtained from the q value of the transient halo with q = 1.45 Å^{-1} (**Figure 1.7b**) which gives a d-spacing of 4.33 Å. The average LC director spacing 4.33 Å is comparable to the average spacing between amorphous backbones, and is substantially larger than the π-π stacking distance 3.63 Å ($q = 1.73$ Å^{-1}). The average LC director spacing eventually evolves into π-π stacking when the film solidifies. Therefore, the anisotropic intensity distribution over χ of the solution coated transient halo (**Figure 1.8d**) come from the LC mesophase with preferred orientation. The scattering intensity near $\chi = 0$ is contributed by face-on LC directors, and intensity near $\chi = 90^o$ by edge-on LC directors. The majority of the LC in the bulk and bottom moderately prefers face-on orientation,[38] resulting in higher intensity at $\chi = 0\text{-}50^o$. Meanwhile the LC at the very top interface shows a distinct edge-on orientation, giving rise to the sharp peak near $\chi = 90^o$ in **Figure 1.7d**. Because we conclude from solution SAXS measurements that the LC mesophase has smectic-like layers, we propose the stacking structure of the LC mesophase in **Figure 1.8b** with average director distance of 4.33 Å and smectic layer spacing of 32.9 Å. After elucidating the LC structure and orientation in the meniscus, we correlate the out-of-plane orientation of the LC mesophase with the orientation in thin films (**Figure 1.8c**) during the process of solution coating and drying. Smectic-like LC mesophase forms at the front of the meniscus when the critical concentration is reached (between 60 - 100 mg/ml) by solvent evaporation during solution coating of DPP-BTz from chlorobenzene. Because surface energy minimization, alkyl chains prefer to stick out of the air-liquid interface, leading to edge-on orientation of the mesophase at the top interface. This gives rise to the sharp peak near $\chi = 90^o$ in **Figure 1.7d**. The LC mesophase in the bulk liquid layer and the bottom interface experience symmetry breaking and adopts the orientation with the LC director aligning moderately along the substrate,[45] resulting in the broad intensity at $\chi = 0\text{-}50^o$ in **Figure 1.7d**. When the solvent further evaporated, the edge-on LC evolves into edge-on crystallites at the top surface of the dried polymer film, while the face-on LC into face-on crystallites in the bulk and at the bottom of the film. Similar LC-induced out-of-plane orientation distribution in films is previously reported for discotic small molecule LC.[46] Overall, the crystallization process of DPP-BTz undergoes an isotropic-LC mesophase-solid thin film transition where the out-of-plane orientation is predetermined by the LC mesophase before evolving into crystallites.

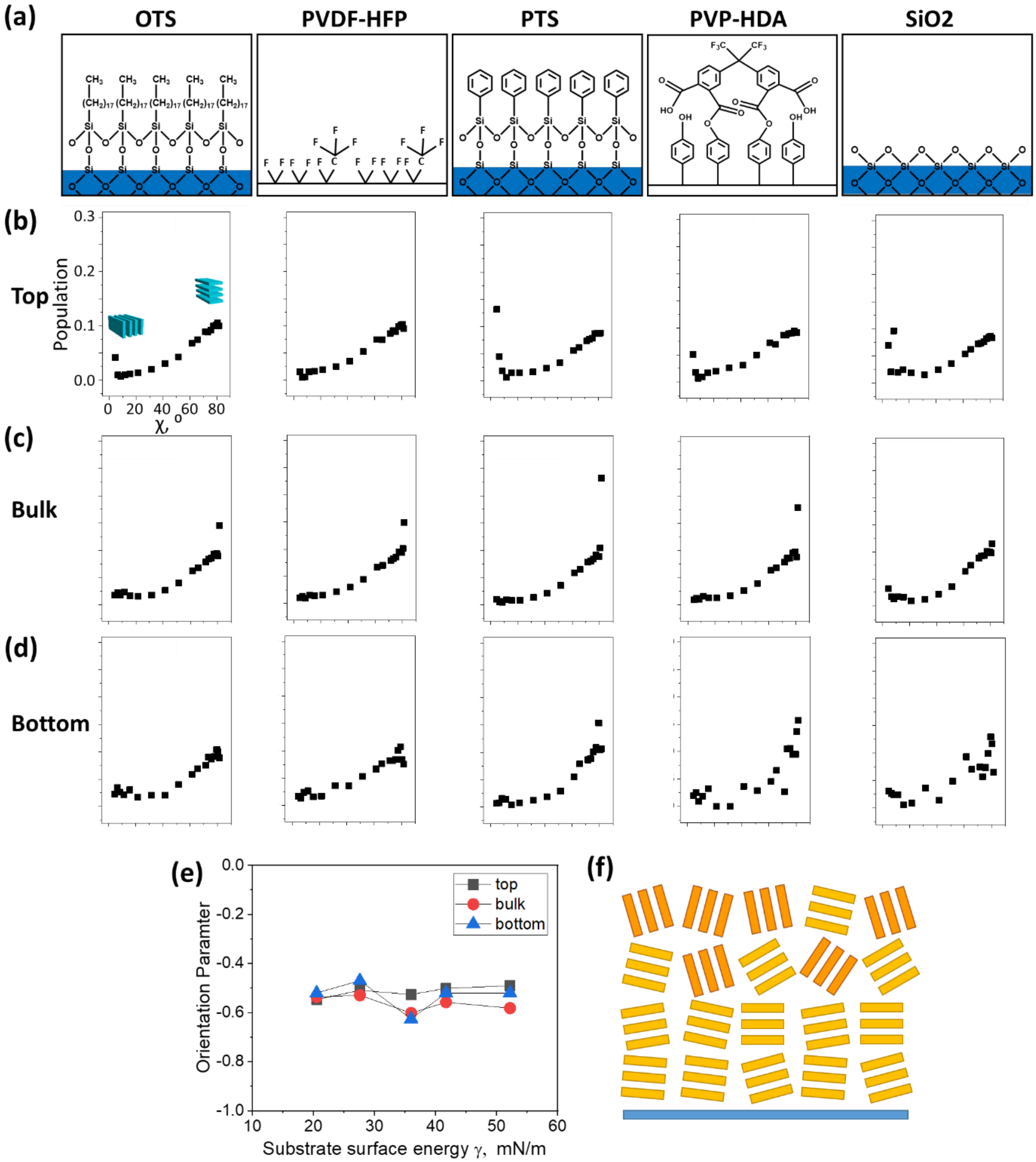

Figure 1.9. (a) Molecular structure of substrate and partial pole figures of the (b) top interface, (c) bulk film and (d) bottom interface of solution coated DPP-BTz on OTS, PVDF-HFP, PTS, PVP-HDA and SiO^2 substrates at 0.5 mm/s and 80 ºC. (e) Out-of-plane 2D orientation parameter from GIWAXS pole figures measurements for various substrates. (f) Illustration of out-of-plane molecular orientation of DPP-BTz thin films on various substrates.

Having understood the appearance of face-on LC mesophase near the substrate interface and in the bulk liquid layer, we look into the influence of substrate interaction with the conjugated polymer on the templating effect of the LC mesophase and the final orientation of crystallites in the film. We prepare a series of substrates with various substrate surface energy: OTS ($\gamma = 20.5$ mN/m), PVDF-HFP (27.6 mN/m), PTS (36.0 mN/m), PVP-HDA (41.7 mN/m) and SiO_2 (52.2 mN/m), with molecular structure in **Figure 1.9a**. The surface energy of OTS, PTS, PVP-HDA and SiO_2 is determined in previous work, and the surface energy of PVDF-HFP is determined by the by contact angle measurements of known probing liquids with least-square method analysis using the equation of state.[47] DPP-BTz thin films are deposited onto the substrates at 10 mg/ml concentration in chlorobenzene with 0.5 mm/s coating speed at 80 ºC (**Figure A6**). Similar as the coating speed series, we carry out GIWAXS measurements for the top interface, bulk film and bottom interface of the DPP-BTz substrate series thin films and construct the corresponding partial pole figures (**Figure 1.9 b-d**). The top interface from most substrates again shows the existence of edge-on crystallites, compared to the primarily face-on bulk film and bottom interface. However, the out-of-plane orientation does not show significant change with respect of substrate surface energy, reflected in the calculated out-of-plane 2D orientation parameter (**Figure 1.9e,** tabulated in **Table A2**). The calculated 2D orientation parameter values concentrate near -0.5, without significant interface/bulk film differentiation. Hence, varying molecular interactions between polymer and substrate by using different modification layers does not change the out-of-plane orientation of DPP-BTz, validating that the solid state orientation is determined by LC symmetry breaking at interfaces in the solution state. The out-of-plane molecular morphology of the DPP-BTz substrate series is very similar as the previous speed series, with edge-on crystallites at the top surface and face-on crystallites in the bulk and at the bottom interface (**Figure 1.9f**).

In this work, we show that varying molecular interaction between polymer and solid substrate does not alter the out-of-plane molecular orienration of DPP-BTz. On the other hand, our collegues have demonstrate that by varying the amount of ionic liquid in the ion gel substrate, the orienration of DPP-BTz thin film shifts from face-on to edge-on with increasing amount of ionic liquid up to an optimum percentage.[33] It is because ionic liquid with high degree of dynamics enhances polymer self-interactions at the ionic liquid substrate/polymer solution interface and significantly expedite the crystallization rate of the polymer, leading to edge-on molecular orienration in the final film. The strength of Van de Waals interaction between solid substrates and polymer in this work cannot outcompete the effect of ion-π interactions for the ionic liquid/polymer pair and the dyanmic nature of the liquid substrate, resulting in no effect on out-of-plane molecualr orienration when changing solid substrates.

1.3 Conclusion

In summary, we deposit DPP-BTz thin films using meniscus guided solution coating and observe liquid crystalline mesophase governed out-of-plane molecular orientation distribution in the conjugated polymer thin film. Revealed by GIWAXS and NEXAFS measurements, conjugated polymer molecule exhibit edge-on orientation at the top interface of the film, while adopting face-on orientation at the bulk film and the bottom interface. We discover the existence of liquid crystalline mesophase at the meniscus front during solution coating by microscopy and utilize X-ray measurements to understand the packing structure of the LC mesophase. Solution SAXS and in situ μGIWAXS during coating suggest a spacing of 32.9 Å and a smaller spacing of 4.33 Å, respectively. With assigning the LC directors orthogonal to the conjugated polymer backbone and along the DPP and BTz units, we attribute the 32.9 Å spacing to the smectic-like layer spacing and the 4.33 Å spacing to the average director distance. We also find anisotropic intensity distribution of the 4.33 Å peak ($q = 1.45$ Å^{-1}) over the χ angle from μGIWAXS, where high intensity is observed at $\chi = 0\text{-}50^{o}$ (weakly face-on LC) and intensity peaked near $\chi = 90^{o}$ (highly edge-on LC).

The smectic-like LC mesophase evolves into lamellar and π-π stacking in the polymer crystallites, and the out-of-plane orientation of the LC mesophase directly relates to the dried film molecular orientation. With discussion and quantitative analysis on the lyotropic liquid crystalline phase appeared during solution coating of conjugated polymer DPP-BTz, we enrich our knowledge of the polymer phase transformation under the evaporative assembly process. Furthermore, modification methods on orientation control of liquid crystals can be further utilized on lyotropic conjugated polymers for directed assembly, and therefore benefiting for their electronic applications and performances.

1.4 Experimental Section

Substrate treatment. Multiple surface treatments are performed to vary the substrate surface energy. Octadecyltrichlorosilane (OTS) treatment is performed by immersing a plasma treated silicon wafer with 300 nm SiO2 layer in 50 mL of trichloroethylene mixed with 100 μL OTS at room temperature for 20 minutes. The wafer is then washed with solvents and baked at 120 ºC for 20 minutes to crystallize OTS. Poly(vinylidene fluoride-co-hexafluoropropylene) (PVDF-HFP) substrate is prepared by spin-coating 1:8 weigh ratio PVDF-HFP in acetone solution onto plasma treated 300 nm SiO_2 substrate at 3000 rpm for 1 minute. The PVDF-HFP substrates are heated at 80 ºC in glovebox overnight. Phenyltrichlorosilane (PTS) treatment is performed by heating the immersed wafer in 50 mL of toluene mixed with 1.5 mL PTS at 90 ºC for 12-15 hours. The wafer is rinsed with solvents and sonicated in toluene for 3 minutes before drying. Poly(4-vinylphenol) and 4,4′-(hexafluoroisopropylidene)diphthalic anhydride (PVP-HDA) substrate is prepared by spin coating PVP and HDA in propylene glycol methyl ether acetate (PEGMA) solution (20 mg/ml for PVP and 2 mg/ml for HDA) at 7000 rpm for 1 minute. The PVP-HDA substrates are heated at 100 ºC in glovebox for 1 hour and at 60 ºC in vacuum oven for 1 hour.

Conjugated polymer thin film preparation. Poly[[2,5-bis(2-octadecyl)-2,3,5,6-tetrahydro-3,6-diketopyrrolo[3,4-c]pyrrole-1,4-diyl]-alt-(2-octylnonyl)-2,1,3-benzotriazole] (DPP-BTz) (M_w = 463 kg/mol, PDI = 2.6) is synthesized as previously reported and used as received.[48] DPP-BTz solution for thin film printing is prepared by dissolving the conjugated polymer at 10 mg/ml in chlorobenzene and stirred at 40 ºC until a homogeneous solution is obtained. DPP-BTz thin films are deposited onto the substrates by a meniscus guided coating method using an ODTS treated SiO_2 blade.[31] The set up includes a stationary substrate and a motor-driven blade with solution sandwiched in between. The blade is set with a tilt angle of 8º and a gap of 100 µm above the substrate for coating of polymer thin films. The substrate temperature is fixed at 80 ºC and the coating speed between 0.5 mm/s to 100 mm/s.

X-ray characterizations for thin film and liquid crystalline phase. Static state grazing incidence wide angle X-ray scattering (GIWAXS) is performed at beamline 8-ID-E at Advance Photon Source at Argonne National Laboratory. Data are collected on a two-dimensional Pilatus 1M detector with an X-ray beam energy at 10.9 keV. Data collection, extraction and processing is performed with the GIXSGUI package written for Matlab.[49] Experiments are carried in a vacuum chamber at room temperature with incident X-ray angle at 0.14º for bulk film measurements and 0.04º for surface measurements. Top surface measurements are performed on as casted films on the substrates. Bottom surface measurements are performed on inverted films on polydimethylsiloxane (PDMS) stamps. The PDMS stamps are prepared by mixing Dow Corning Sylgard 184 silicone potting compound and cross-linking agent and curing the mixture in a house vacuum oven at 50°C for 2 hours. For SiO_2 and PVDF-HFP substrates, the mixing ratio of elastomer and cross-linker is 10:1, while for PVP-HDA and PTS substrates, the mixing ratio was increased to 15:1 for better adhesion. The sandwiched films between the substrate and PDMS are immersed in acetonitrile overnight and then peeled from the substrates. Samples are scanned with the incident beam orthogonal to the coating direction. Partial pole figures are constructed by obtaining the intensity of the (100) lamellar stacking peak with respect of the χ angle to study the out-of-plane distribution of the crystallites. The (100) lamellar stacking peak is fitted with a Gaussian function to obtain the peak area and is multiplied with $\sin(\chi)$ at the corresponding χ angle for geometric correction. The pole figures are normalized for cross sample comparison.

Grazing incidence small angle X-ray scattering (SAXS) is performed at beamline 12-ID-B at the Advanced Photon Source at Argonne National Laboratory. Liquid samples are measured in 2.0 mm quartz capillary tubes and solid samples are measured in aluminum sample pans for dynamic scanning calorimetry. Data are collected on a two-dimensional Pilatus 2M detector with an X-ray beam energy at 13.3 keV. In situ thermal SAXS experiments are carried on a Linkam THMS600 stage from 25 ^{o}C to 125 ^{o}C for liquid samples and to 300 ^{o}C for solid samples. The collected data are azimuthally integrated into one-dimensional scattering profiles. Background correction is applied with respect of solution filled capillary or empty aluminum pan when necessary.

In situ μGIWAXS is performed at former beamline D1 at Cornell High Energy Synchrotron Source. Data are collected on a two-dimensional Pilatus 200k detector with an X-ray beam energy at 12.7 keV. The X-ray microbeam is focused by a single-bounce X-ray capillary and is 40 μm in width to ensure high special resolution during measurement. A meniscus guided coating set up is installed at the beamline. The blade is tilted at 15^{o} and the stage temperature is set at 70 ^{o}C. DPP-BTz solution is made in chlorobenzene at the concentration of 5 mg/ml. The solution coating speed is controlled between 0.1 to 0.5 mm/s. The recording rate of the diffraction pattern is up to 50 frames per second, with an exposure time of 0.02 s.

2D Orientation Parameter Calculation. We calculate the 2D out-of-plane orientation parameter from both GIWAXS and NEXAFS measurements with equation[32, 38, 39]:

$$S_{2D} = < cos2\gamma > = 2 < \cos^2 \gamma > -1 \qquad \text{(Eqn 1.1)}$$

where γ is the angle between the polymer conjugation plane and the substrate normal. In this case, S = 1 indicates a completely edge-on orientation of the molecules, S = 0 an isotropic orientation and S = -1 a completely face-on orientation. We use the 2D orientation parameter because of the easiness of evaluation the out-of-plane orientation on the -1 to 1 scale.

For GIWAXS measurements, the averaged out-of-plane orientation of the biaxially aligned crystalline materials is given by[50, 51]:

$$< \cos^2 \gamma >_{GIWAXS} = \frac{\int_0^{\pi} I(\gamma)\cos^2(\gamma)\sin(\gamma)d\gamma}{\int_0^{\pi} I(\gamma)\sin(\gamma)d\gamma} \qquad \text{(Eqn 1.2)}$$

Because partial pole figures are constructed by recording (100) peak intensity at different χ angles, in this case, the value of χ equals to the value of θ. Therefore $<\cos^2 \gamma>$ can be calculated from the results of the pole figures:

$$< \cos^2 \gamma >_{GIWAXS} = \frac{\sum I(\chi)_i \cos^2(\chi)_i \sin(\chi)_i \Delta\chi_i}{\sum I(\chi)_i \sin(\chi)_i \Delta\chi_i} \qquad \text{(Eqn 1.3)}$$

where i was the specific data point in the partial pole figures for each condition.

For NEXAFS measurements, the intensity of the C1S→π* resonance is dependent on the incident angle θ, with assuming zero degree molecular pre-tilt angle[40]:

$$I(\theta) = A + Bsin^2(\theta) \qquad \text{(Eqn 1.4)}$$

where A and B are the fitting parameters obtained from measurements with a set of incident angles. Because the DPP-BTz thin films are biaxially aligned, tilt angle NEXAFS measurements are performed with the incident beam parallel and perpendicular to the coating direction, giving A_{para}, B_{para}, A_{perp}, B_{perp} from fitting.

After obtaining the fitted parameters, the theoretical total intensity from NEXAFS can be calculated:

$$I_{tot} = \frac{3}{2}\left(A_{para} + A_{perp}\right) + \frac{3P-1}{2P}\left(B_{para} + B_{perp}\right) \qquad \text{(Eqn 1.5)}$$

where P is the polarization factor of the incident X-ray beam and P =0.85. The averaged out-of-plane orientation from the NEXAFS can be calculated:

$$< \cos^2 \alpha >_{NEXAFS} = \frac{A_{perp}+B_{para}(1-1/P)}{I_{tot}} \qquad \text{(Eqn 1.6)}$$

where α is the angle between the π* TDM and the substrate normal. Because the π* TDM is orthogonal to the conjugated plane orientation, and γ in Equation A1 is defined as the angle between the conjugated plane with the substrate normal, the calculated S2D from $<\cos^2\alpha>_{\text{NEXAFS}}$ need to be multiplied with -1

$$S_{2D,NEXAFS} = -(2 < \cos^2 \alpha >_{NEXAFS} - 1) \qquad \text{(Eqn 1.7)}$$

The calculated 2D orientation parameter are listed in Table A1.

Field effect transistor device fabrication. Top gate bottom contact (TGBC) and bottom gate top contact (BGTC) field effect transistors are fabricated with DPP-BTz thin films to measure charge transpor mobility at the top and bottom interface, respectively. For TGBC devices, 35 nm Ag sorce/drain electrodes are thermally evaporated onto 300 nm SiO_2 substrates, followed by coating of DPP-BTz thin films. PMMA 80 mg/ml in n-butylacetate solution is perpared and filtered, and then spin coated at 2000 rpm with 500 rpm for 60s on the DPP-BTz thin films as the dielectric layer. Another layerm of 35 nm Ag is evaporated on top of the 450 nm PMMA layer as gate electrodes. BGTC devices are prepared by evaporating 35 nm Ag source/drain electrodes on the DPP-BTz thin film coated on 300 nm SiO_2 substrates. All device measurements are performed with Keysight B1500A semiconductor parameter analyser under nitrogent enviroment. The field effect mobilities are calculated in the saturation region of the transfer curved by the equation $I_{DS} =$

$\frac{WC_i\mu}{2L}(V_G - V_T)^2$, where I_{DS} is the drain-source current, W and L the conduction channel width and length, C_i the capacitance of the dielectric layer (11 nF/cm^2 for 300 nm SiO_2 layer and 6.8 nF/cm^2 for 450 nm PMMA layer), μ the apparant mobility, V_G the gate voltage, and V_T the threshold voltage.

Chapter 2

Understanding Interfacial Alignment in Solution Coated Conjugated Polymer Thin Films[2]

2.1 Introduction

Conjugated polymers (CPs) have been intensively studied in recent decades owing to their potential applications in a wide range of technologies from flexible electronics, alternative energy conversion devices to biomedical imaging. A major advantage of conjugated polymers is their compatibility with low-cost, high-throughput manufacturing methods such as roll-to-roll printing. The solution printing process has a direct impact on the thin film morphology across multiple length scales. It is well known that thin film morphology characteristics can modulate charge transport properties in conjugated polymers by orders of magnitude.[52] At molecular scale, the extent of order in the crystalline/aggregated domains is described by paracrystallinity. In thin films with isotropic domain orientations, paracrystallinity has been shown to limit global charge transport.[53] Besides the importance of paracrystallinity to interchain charge transport, backbone planarity was shown to be critical to intrachain charge transport, which explains the excellent performance of several nearly amorphous high molecular weight polymers recently reported.[54, 55] At mesoscale, connectivity between crystalline/aggregated domains is of critical importance; inter-grain 'tie-chains' was proposed as charge-transport highways,[56, 57] while abrupt grain boundaries that interrupt backbone conjugation is detrimental to charge transport[58, 59], the extent

---

[2] The contents of this chapter appear in Qu, G.; Zhang, F.; Mohammadi, E.; Zhao, X.; Strzalka, J.W.; Mei, J.; Diao, Y. "Understanding Interfacial Alignment in Solution Coated Conjugated Polymer Thin Films". *ACS Applied Materials & Interfaces*, **2017**, 9, 25426-25433

to which may depend on the grain boundary orientation. It was also demonstrated that domain alignment in polymer thin films can enhance charge transport from a few times to over an order of magnitude.[25, 32, 60-63] Yet, there has not been systematic study reported to elucidate the origin of this phenomenon with regard to charge transport mechanisms.

Driven by the large performance gain from domain alignment, many methods have been developed to induce alignment in conjugated polymer thin films, including mechanical rubbing,[64] grooved template directed solution deposition,[65, 66] and unidirectional coating.[25, 32, 63, 67, 68] Most unidirectional coating methods reported employed a liquid crystalline conjugated polymer to attain the high degree of alignment reported.[25, 63, 67] On the other hand, depending on the specific system and the coating/printing conditions, the degree of alignment can vary from nearly isotropic (dichroic ratio ~1)[69] to highly aligned (dichroic ratio >10).[32] So far, the mechanism for attaining in-plane alignment during unidirectional coating/printing remains unclear. Here we refer the in-plane alignment to the alignment of polymer rod long axis parallel to the substrate plane and the out-of-plane alignment to the alignment of polymer rod long axis with the substrate normal. Although most studies attribute the observed in-plane alignment to shear flow during coating, the shear rate is in fact along the out-of-plane direction, and is minimal in-plane. It is unclear to what extent and by what mechanism out-of-plane shear can induce in-plane alignment. In addition, contributions of other flow types are often ignored, such as extension and compression which are prominent in evaporation driven capillary flows that occur during solution coating/printing.

Although domain alignment has been extensively investigated, fewer studies distinguished alignment at the interface from that in the bulk of the thin film. On the other hand, interfacial morphology at the semiconductor-dielectric interface is directly relevant to charge transport in field-effect transistors. Morphologies at the interface distinct from that in the bulk have been observed, including out-of-plane molecular orientation[41, 70, 71] and in-plane backbone alignment.[32, 37] Regarding in-plane alignment, Schuettfort and McNeill et al. found a high degree of backbone alignment at the surface of zone-casted poly[2,5-bis(3-tetradecylthiophene-2-yl)thieno[3,2-b]thiophene] (PBTTT) films, compared to little alignment in the bulk of as-cast films.[37] Schott and Sirringhaus et al. observed lower degree of alignment at the film surface compared to that in the bulk, in diketopyrrolopyrrole-benzotriazole co-polymer (DPP-BTz) thin films coated using a soft blade.[32] In addition, Patel and Kramer et al. observed different degrees of alignment at the top and bottom interfaces in blade coated cyclopentadithiophen-thiadiazolopyridine co-polymer (PCDTPT) thin films, a phenomenon dependent on the coating speed.[40] On the other hand, the underlying mechanism for a distinct interfacial morphology has yet to be elucidated.

In this work, we observed significantly different morphology at the free interface as compared to that in the bulk for solution coated poly(diketopyrrolopyrrole-*co*-thiophene-*co*-thieno[3,2-b]thiophene-*co*-thiophene) (DPP2T-TT) thin films. The air-film free interface exhibits fibril-like morphology; the polymer backbone extends parallel to the long axis of the fibrils, both of which aligned along the coating direction under most conditions tested. Interestingly, from the free interface to the bulk, the polymer backbone and the fibril long axis both alter in in-plane orientation to be either weakly aligned transverse to the coating direction or nearly isotropic, depending on the thickness of the film. Higher degrees of alignment at the free interface give rise to high charge transport anisotropy of up to ~6, with favored charge transport direction along the polymer backbone. This is in contrast to low charge transport anisotropy of ~1 obtained at the buried interface, whose morphology resembles that of the bulk. We further show that the preferred charge transport direction is strongly correlated with the preferred in-plane orientation of the polymer backbone. Finally, we propose a mechanism based on skin-layer formation and extensional flow induced in-plane alignment, in contrast to what has been widely hypothesized that shear flow drives alignment during meniscus-guided coating.

2.2 Results

To characterize molecular alignment in solution coated thin films, we prepared DPP2T-TT films using a meniscus guided coating method wherein the ink solution was sandwiched between a moving blade and a substrate (**Figure 2.1a**). The method is detailed in previous publications,[72, 73] originated from evaporative assembly known as the "coffee ring effect".[74] Briefly, DPP2T-TT (**Figure 2.1b**) thin films were coated from chloroform solutions at various concentrations (3 mg/ml to 25 mg/ml) on octadecyltrichlorosilane (ODTS) treated 300 nm SiO_2 on Si (100) substrates. The ODTS surface treatment was applied to minimize charge traps at the semiconductor-dielectric interface. The coating speed was 0.5 mm/s and the substrate temperature was controlled at 25 ^{0}C. By changing the solution concentration, the film thickness was varied from 20.8±0.8 nm (3 mg/ml) to 168±7 nm (25 mg/ml) to systematically vary the fraction of the interfacial layer out of the bulk (**Figure B1**). The coating speed of 0.5mm/s falls within the evaporation regime of solution coating (**Figure B2**). We further show that varying solution concentration did not alter the polymer aggregation state (**Figure B4, B5, Table B1**).

We next employed a suite of techniques probing the interfacial and bulk morphology across multiple length scales. We performed cross-polarized optical microscopy (CPOM) for visualizing global alignment and crystallinity, polarized UV-Vis spectroscopy for quantifying polymer backbone alignment in the bulk of the film, atomic force microscopy (AFM) for characterizing mesoscale morphology at the free and buried interfaces, and grazing incidence wide angle X-ray scattering (GIWAXS) for probing bulk and interfacial alignment in crystalline domains.

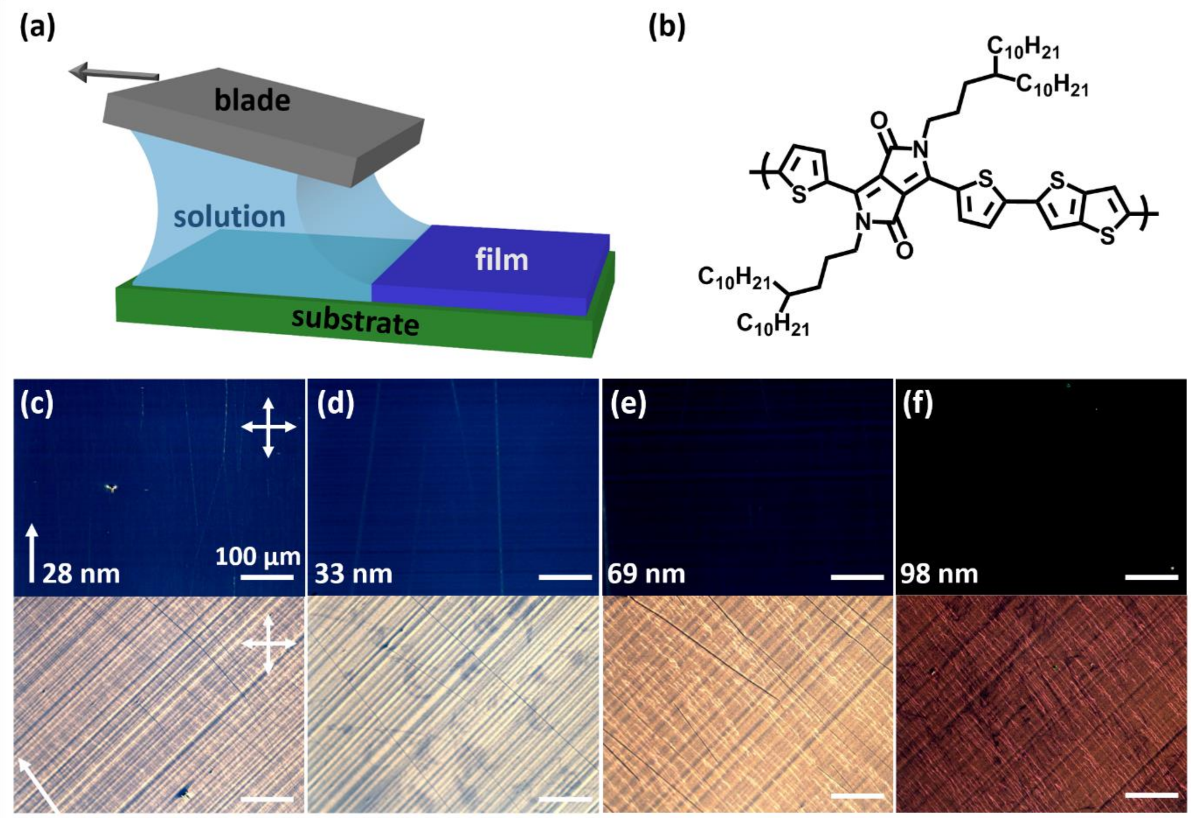

Figure 2.1. Solution coating of DPP2T-TT thin films and resulting birefringence for films of various thicknesses under cross-polarized microscopy. a) Schematic of solution coating. b) Molecular structure of DPP2T-TT. The film thicknesses are c) 28 nm, d) 33 nm, e) 69 nm and f) 98 nm coated from solutions with concentrations of 5, 7, 10, 14 mg/ml respectively. The first and the second rows of images correspond to films with coating direction oriented 0^0 and 45^0 with respect to the axis of the polarizer. The arrows at bottom left denote the coating direction and the crossed arrows indicate orientations of the crossed polarizers. Scale bars are 100 µm in all images.

Characterization of bulk alignment. First, we applied cross-polarized optical microscopy (CPOM) whereby the observed birefringence offers a qualitative characterization of the degree of in-plane alignment between the crystalline domains. For films exhibiting global alignment, an extinction of light is expected when the long axis of the polymer backbone in the crystallites is aligned with one of the polarizers. We observed light extinction in solution coated thin films when the coating direction was at 0^0 and 90^0 with respect to the axis of the polarizer (**Figure 2.1c, d, e, f**), indicating that the polymer backbone in crystalline domains is aligned along or transverse to the coating direction. This inference is consistent with the observation that the brightest reflection occurred when the coating direction was oriented 45^0 with respect to the polarizer. With increasing concentration/film thickness, an increasing and then decreasing trend in birefringence was observed (**Figure B3**). Although birefringence is correlated with the degree of alignment in the film, it is also proportional to the film thickness and the degree of crystallinity. The initial increase in birefringence (**Figure 2.1c, d**) may be attributed to enhanced polymer alignment and/or increase in film thickness. However, the decrease of birefringence at higher concentrations (**Figure 2.1e, f**) indicates a lower degree of alignment and/or crystallinity in thicker films. To quantify the degree of alignment in the bulk of the film, we further employed polarized UV-Vis spectroscopy.

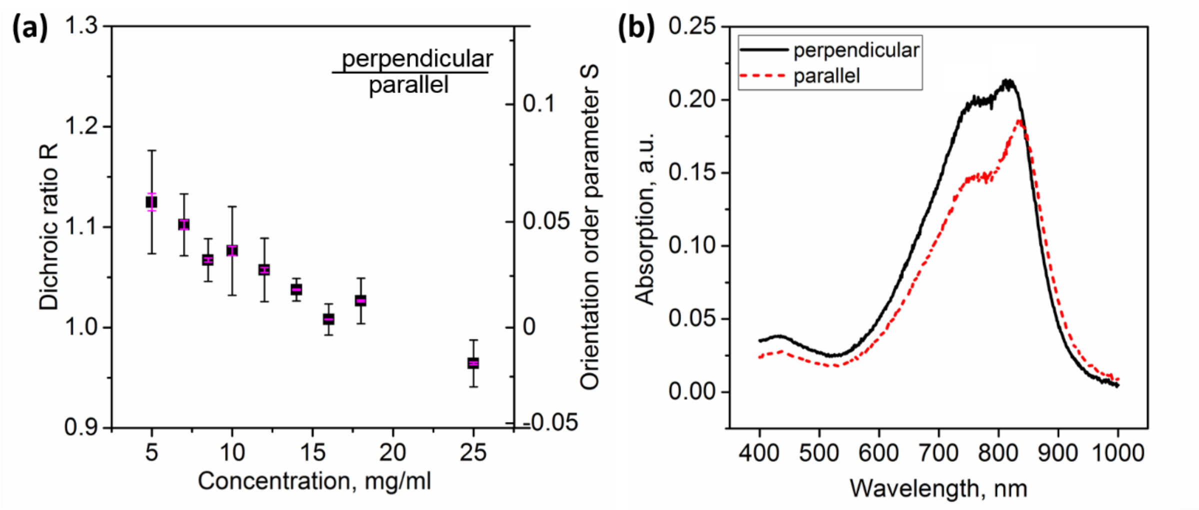

Figure 2.2. Degree of alignment in the bulk of coated thin films characterized using polarized UV-Vis spectroscopy. (a) Dichroic ratio R and in-plane orientational order parameter S from polarized UV-Vis spectroscopy as a function of film concentration/thickness. R and S were calculated from the peak absorbance at approximately 820 nm. The error bars of the same color corresponds to the standard deviation of R and those with a different color correspond to S. Error bars were obtained from 3 measurements of independent samples. (b) Polarized UV-Vis absorption spectra in parallel and perpendicular orientations for films coated from 5 mg/ml solution. For both images, parallel and perpendicular orientations are defined in terms of the coating direction with respect to the axis of the polarizer.

Polarized UV-Vis spectroscopy measurements were performed on DPP2T-TT thin films coated on ODTS treated glass slides with the light polarization direction oriented either parallel or perpendicular to the coating direction. Because the transition dipole is principally along the polymer backbone direction,[75-77] the UV-Vis absorbance is expected to be the highest when the backbone is aligned with the polarization direction of the UV light. The degree of alignment of the polymer backbone can be characterized in terms of the dichroic ratio $R = A_{perp}/A_{para}$ with A_{perp} and A_{para} denoting the absorbance when the coating direction is perpendicular and parallel to the electric field pass direction of the polarizer. We note that R only provides a lower bound to the degree of backbone alignment, as the transition dipole may have a non-zero component normal to the polymer backbone.[75, 78] We calculated R values using the peak absorbance at 820 nm (**Figure 2.2a**), as the shoulder at 760 nm may not be uniquely assigned to a single vibrational peak.[78] We further calculated the orientational order parameter $S = (R-1)/(R+1)$ to represent the degree of backbone alignment on a scale from -1 to 1, with 0 denoting completely isotropic, 1 uniaxially aligned perpendicular to the coating direction and -1 uniaxially aligned parallel to coating.[79] Calculation of S from R as shown above is based on the assumption that the UV-Vis absorbance scales with the magnitude of transition dipole moments projected along the polarization direction of light, following $A_{para} \propto \langle \cos^2\phi \rangle$ wherein ϕ is the angle between the transition dipole and the light polarization direction.[39] With $R > 1$ and $S > 0$ at most conditions, we infer that the polymer backbone was preferentially oriented perpendicular to the coating direction in the bulk of the thin film. However, the degree of alignment is at best weak and at worst isotropic. Even the thinnest film (~24nm) coated from 5mg/mol solution exhibited a dichroic ratio R (820 nm) of only 1.12, corresponding to $S = 0.06$. We further observed a decreasing trend of dichroic ratio with increasing concentration/film thickness, which is consistent with decreasing birefringence observed from CPOM (**Figure 2.1**) assuming that the initial increase in birefringence was due to increase in film thickness.

Characterization of interfacial morphology. We next performed GIWAXS and AFM to probe surface (film-air interface) morphology as compared to the bulk and the buried interface (film-substrate interface). While UV-Vis spectroscopy probes both the crystalline and the amorphous domains, GIWAXS signals come from the crystalline domains only. To evaluate the anisotropy of the in-plane molecular packing, GIWAXS measurements were taken with the incident beam parallel and perpendicular to the coating direction. This method yields an in-plane anisotropy between crystallites that satisfy the Bragg condition only, specifically, crystallites with edge-on π-stacks oriented parallel or perpendicular to the incidence beam. Crystallites with other in-plane orientations are not accounted for in this method, which is in contrast to the anisotropy obtained from UV-vis, whereby transition dipoles of all orientations contribute to the absorbance as discussed above. To differentiate the top interface from the bulk, we set the X-ray incident angle both above and below the critical angle of the organic layer, $\approx 0.1°$, to probe the molecular packing throughout the film and near the film surface, respectively.[80] Above the critical angle, X-ray penetrates the entire film, whereas below the critical angle, X-ray probes the top surface layer with approximately 5 nm penetration depth, or two molecular layers.[41] Surface measurements were also performed on the laminated DPP2T-TT films to study the molecular packing at the buried film-substrate interface, but no meaningful data was obtained due to the strong background scattering from the PDMS substrates used for film lamination.

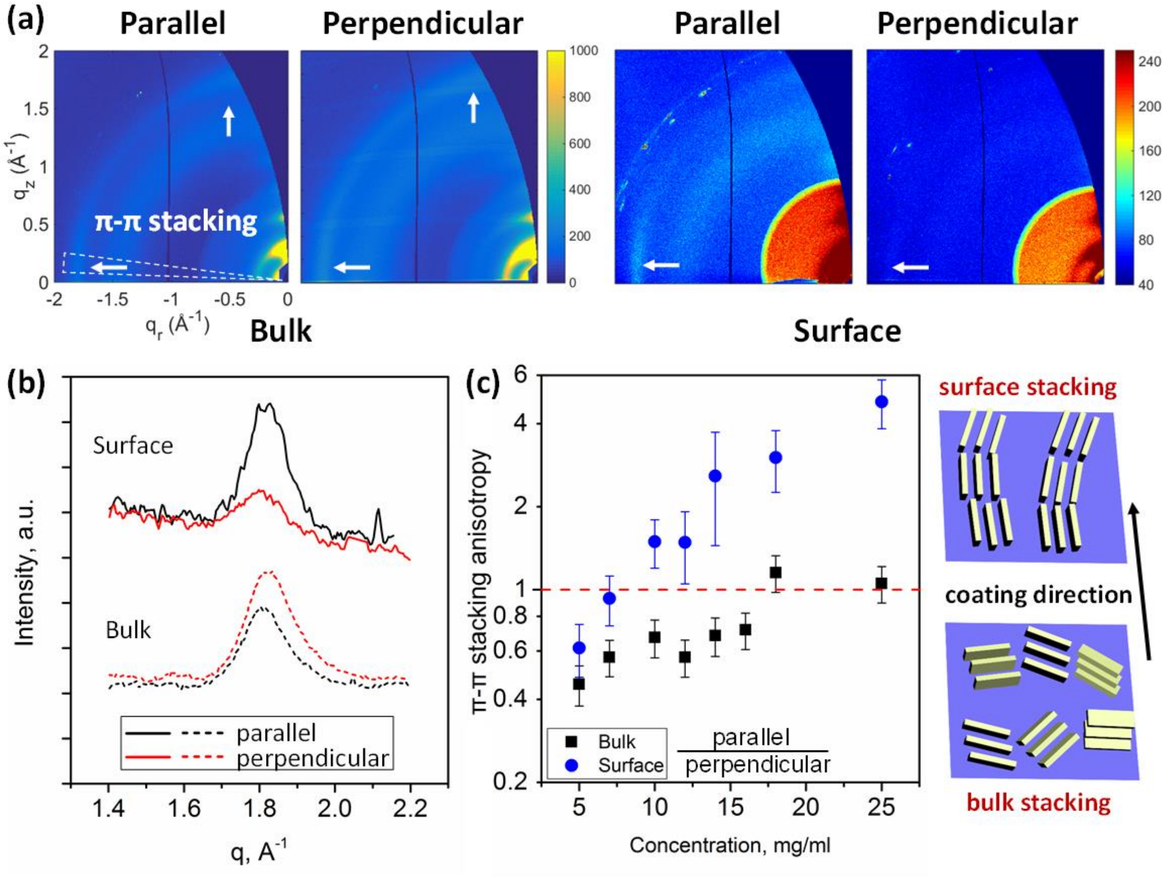

Figure 2.3. Surface vs. bulk morphology and alignment probed by GIWAXS. a) GIWAXS patterns for the 14 mg/ml (98±2 nm) DPP2T-TT thin film, measured in parallel and perpendicular orientations with 0.2º incident angle for bulk measurement and 0.08 degree incident angle for surface measurement. b) Comparison of the in-plane orientation of the film surface and the bulk film. Path length corrected intensity of the (010) π-π stacking peaks indicates the preferred in-plane orientation of the π-π stacks, obtained from a sector cut on the GIXD images with -88°<χ<-83° (cut area indicated on **Figure 2.3a**). Surface peaks were scaled by a factor of 5 for direct comparison with the bulk case. c) In-plane alignment indicated from the π-π stacking anisotropy P of the edge-on π-π stacking peak in the bulk and at the film surface. Error bars were obtained from peak intensity error resulted from incident angle alignment as well as from error of peak fitting. The schematics show the alignment of the π-stack at the film surface vs. the bulk.

Representative 2D X-ray scattering patterns from both the bulk and the surface measurements in parallel and perpendicular orientations are shown in **Figure 2.3a**. Detailed analysis on the peak area, π-π stacking distance and peak width are summarized in **Figure B6**. For the bulk film, the intensity of the edge-on portion of the (010) π-π stacking peak (on the horizon) from the perpendicular measurement is stronger than that in the parallel measurement with comparable illuminated volume for films coated from solutions of 18 mg/ml and below, indicating that the in-plane π-π stacking direction is preferentially aligned parallel to the coating direction (**Figure 2.3b**). In other words, the polymer backbone in the bulk prefers to align perpendicularly with respect to the coating direction, in agreement with the UV-Vis results. However, surface measurements reveal more intense in-plane (010) peak in the parallel direction instead, indicating that the π-π stacking is perpendicular to coating and the polymer along the coating direction at the film surface. Therefore, GIWAXS reveals an unexpected morphology outcome that the crystallites at the top surface oriented opposite to those in the bulk of the film (**Figure 2.3c**). Apart from the in-plane alignment, the out-of-plane alignment is also visible from the scattering patterns in **Figure 2.3a**. The arc-shaped scattering patterns for the (010) peak from the bulk film measurements reveal that the crystallites are misaligned in the out-of-plane orientation. However the (010) peaks from the film surface measurements only appear near the horizon on the scattering patterns, denoting primarily edge-on crystallites at the film surface. Therefore, we can conclude that DPP2T-TT crystallites show a higher degree of alignment in both the in-plane and the out-of-plane orientations at the film surface than that in the bulk film.

To quantify the degree of in-plane alignment of the π-stacks, the ratio of the integrated peak areas (IA) for the edge-on (010) peak is calculated as $P = IA_{par}/IA_{perp}$. The edge-on portion of the (010) peak was obtained by performing a sector cut between $-88° < \chi < -83°$, with $\chi = -90°$ representing the in-plane direction. In the bulk film, P is approximately 0.36 at the lowest concentration 5 mg/ml, and is approaching 1 with increasing concentration (**Figure 2.3c**). This trend reveals that the polymer backbone initially orients perpendicularly with the coating direction and becomes more isotropic at higher concentrations/film thicknesses. At the film surface, when the film is thin (20-30 nm), the surface alignment is consistent with the bulk; when the film becomes thicker (>70 nm), the backbone orientation significantly deviates from the bulk. The highest anisotropy P = 4.8 observed on the surface was obtained at the highest solution concentration 25 mg/ml, corresponding to a film thickness of 168 nm. This increasing trend in interfacial alignment with the increase of concentration/film thickness is distinct from that in the bulk. We note that similar interfacial alignment to the bulk for thin films of 20-30 nm may be a result of the difficulty in differentiating the interface from the bulk, when the interface ‘seen’ by X-ray constitutes 20-25% of the thin film.

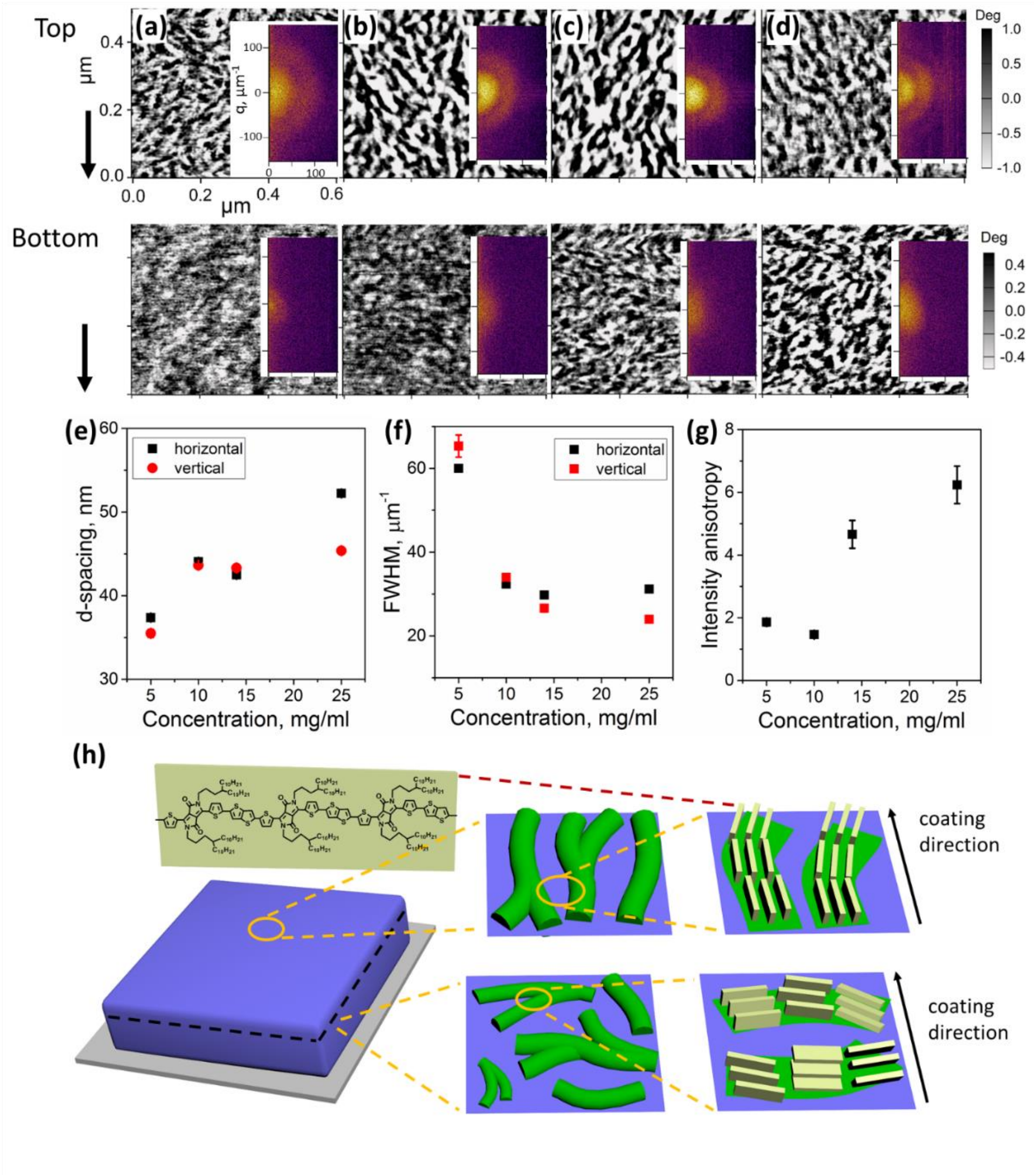

Figure 2.4. Tapping mode AFM phase images of DPP2T-TT thin films coated from chloroform solution at (a) 5 mg/ml, (b) 10 mg/ml and (c) 14 mg/ml (d) 25 mg/ml. The first row is the top interface (film-air interface) scan and the second row is the bottom interface (film-substrate interface) scan. The inset on each phase image is the corresponding FFT image. The coating direction is denoted with the arrow on the left of each row. (e) d-spacing, (f) FWHM and (g) intensity anisotropy of the horizontal and 5° offset vertical linecuts of the 2nd order ring from the top surface FFT. The intensity anisotropy was calculated as the ratio of horizontal peak area over the vertical peak area. (h) Schematic of film morphology and molecular stacking at the top surface vs. the bulk. Green structures represent the mesoscale morphology obtained from AFM and yellow structures the molecular packing obtained from GIWAXS. Note that we assume the morphology at the bottom surface is representative of the average morphology beneath the top layer.

To complement GIWAXS measurements, we further probed meso-scale interfacial morphology at the top air-film interface and the bottom film-substrate interface using AFM. The samples for bottom interface were prepared by laminating solution coated thin films using PDMS stamps (see methods section).[81-83] The AFM phase images in **Figure 2.4** reveal the evolution of the interfacial morphology at the top and the bottom surfaces with respect to concentration/film thickness. At the top air-film interface, we observed short fibril-like structures with local orientational ordering, with the fibril long axis preferentially aligned along the coating direction. Combined with GIWAXS, we infer that the polymer backbone is oriented parallel to the long axis of the fibrils, and that the favorable growth kinetics along the polymer backbone conjugation direction may have resulted in the anisotropic fibril-like morphology. Our observation is consistent with previous works on rigid donor-acceptor polymers, wherein the polymer backbone was found to align with the fiber long axis (eg. PCDTPT,[66] P(NDI2OD-T2)[63]). On the other hand, backbone alignment orthogonal to the fiber long axis has also been reported before, in particular for PBTTT,[67] P3HT[84] presumably due to their lower backbone rigidity. We further performed fast Fourier transform (FFT) to reveal the periodicity and the in-plane orientational ordering of the surface structures observed. Similar to transmission light scattering patterns, sharp and well-defined rings in the FFT image arise from the structure factor when periodic spacing emerges from the aggregated fibers with a narrow size distribution. The intensity distribution along the ring encodes information on the in-plane orientational order of the fibers. For all the top surface AFM scans we observed rings with anisotropic intensity distributions, consistent with the well-defined fibril structures observed on the top surface. The arc on the FFT patterns exhibits higher intensity perpendicular to the coating direction, arising from the periodic spacing along the short axis of the fibrils, or equivalently, preferential orientation of the fibril long axis along the coating direction (**Figure**

2.4h). To quantify the differences observed, we performed linecut (line width covers 30 pixels to improve signal-to-noise ratio) along the horizontal and the vertical direction (with 5° offset to avoid the vertical streak artifact) on the FFT images (**Figure B7, B8**). We further calculated d-spacing, full width at half maximum (FWHM) and peak intensity anisotropy by analyzing the 2nd order arc from the top surface FFT (**Figure 2.4e-g**). On the top surface, we observed larger d-spacing at higher concentration, which reflects increased distance between fibers and therefore increasing fiber width/diameter (**Figure 2.4e**), consistent with AFM phase images. The decreased FWHM indicates a narrower distribution and lower dispersion in fiber spacings **(Figure 2.4f)**. The intensity anisotropy was calculated as the ratio of the peak area from the horizontal orientation over that from the vertical orientation. As expected, the overall intensity anisotropy increases with increasing concentration, indicating better fiber alignment at higher concentrations (**Figure 2.4g**), consistent with the inference from GIWAXS surface scans (Figure **2.3**). On the contrary, the meso-scale morphology at the bottom film-substrate interface is significantly different compared to the top interface at the same concentration. The bottom interface does not have distinct fibril features, indicating lack of distinct periodicity, which likely arises from broad distribution of fibril size and shape. An ellipsoidal pattern extends along the coating direction in each FFT image obtained from the bottom interface scans. Judged from the pattern anisotropy (**Figure B8**), we infer that the long axis of the fibers weakly align perpendicularly to the coating direction at the bottom interface, which is orthogonal to the fiber orientation on the top interface. Because AFM can only probe the morphology at exposed interfaces, information on the meso-scale morphology in the bulk cannot be directly obtained by AFM. Nonetheless, we deduce that the morphology at the bottom interface shares similar features as that in the bulk in terms of in-plane orientation ordering. It is because the polymer backbones in the bulk and at the bottom interface are both weakly oriented orthogonal to that on the top interface, inferred from GIWAXS and AFM respectively.

Putting the results from all morphology characterizations together, we propose a multiscale morphology model illustrated in **Figure 2.4h**, contrasting in-plane and out-of-plane alignment at the top interface vs. that in the bulk. On the top interface, polymer fibrils and the backbone extend along the coating direction, with the polymer backbone oriented edge-on with respect to the interface. In the bulk, the degree of alignment is significantly lower compared to that on the top interface. The long axis of the polymer fibrils and the backbone are weakly aligned transverse to the coating direction, which is opposite to that on the top interface. These distinct differences between bulk and interfacial morphology have important implications on charge transport, which we next evaluate by measuring charge carrier mobility in field-effect transistor devices.

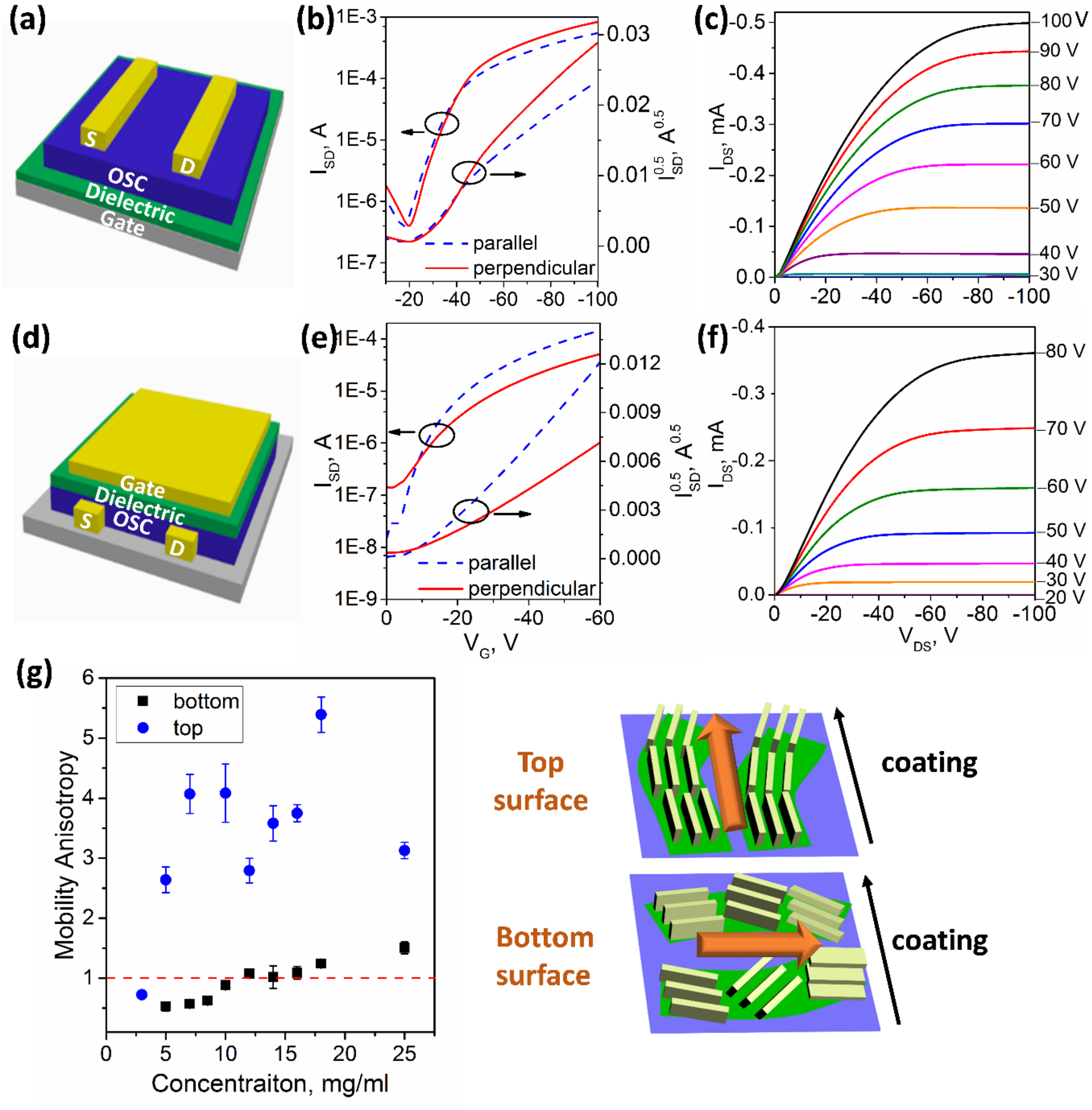

Figure 2.5. Comparison of FET device performance between the (a-c) BGTC configuration and (d-f) TGBC configuration. (b) and (e) are representative transfer curves corresponding to films coated from 7 mg/ml solution for BGTC and 14 mg/ml for TGBC. (c) and (f) are representative output curves. The measurements were performed on films coated from 7 mg/ml solution for BGTC (perpendicular) and 14 mg/ml for TGBC (parallel). The source-drain voltage V_{ds} was -100 V for the BGTC devices and -60 V for the TGBC devices. (g) Hole mobility anisotropy measured in parallel over perpendicular direction with respect to the coating direction for both BCTG and TGBC device configurations. The anisotropy is derived from the high Vg mobilities.

Evaluation of charge transport anisotropy. In thin film field-effect transistors (FETs), charge transport occurs within a few nanometers at the semiconductor-dielectric interface, recognized as the conducting channel.[85] By constructing both top and bottom gate FETs, we were able to quantify the charge transport properties at the top air-film interface and the bottom film-substrate interface of the solution coated thin films. We used the bottom gate top contact (BGTC) configuration (**Figure 2.5a**) and the top gate bottom contact (TGBC) configuration (**Figure 2.5d**) to measure charge transport at substrate-film interface and the air-film interface respectively. The field-effect mobility μ^{sat} was determined from the transfer curves measured in the saturation regime. To determine the preferred charge transport direction and the resulting charge transport anisotropy, we fabricated devices with the channel length along both parallel and perpendicular to the coating direction. The charge transport anisotropy is defined as μ_{par}^{sat} over μ_{perp}^{sat}. The characteristic transfer and output curves comparing BGTC and TGBC devices are shown in **Figure 2.5**, and the extracted apparent mobilities from all conditions are summarized in **Figure B9**. For BGTC devices, we observed a persisting "kink-down" feature in the non-ideal transfer characteristics (**Figure 2.5b**, **Figure B10**), which has been attributed to gate voltage dependent contact resistance.[86, 87] Therefore, we extracted apparent saturation mobilities from both low Vg (-20 to -50 V) and high Vg (-60 to -90 V) regions (**Figure B9**) and used the high Vg mobility to calculate charge transport anisotropy. Although the apparent mobilities are not directly comparable between the BGTC and TGBC devices given different dielectrics and different gate bias used, the charge transport anisotropy can be directly compared because it is only influenced by the interfacial morphology anisotropy as designed in our study.

The top interface exhibits significantly higher charge transport anisotropy compared to the bottom interface, which is strongly correlated with the degree of interfacial alignment observed (**Figure 2.5g**). The mobility anisotropy at the top interface is close to unity only for the thinnest film coated from 3 mg/ml solution, and is significantly higher than 1 at all other conditions when the film thickness exceeds 24 nm (above 5mg/ml). The highest mobility anisotropy observed reaches 5.39±0.05, which is among the highest observed for DPP based polymers.[32, 68] In comparison, the mobility anisotropy on the bottom interface is close to unity for the entire concentration range studied. Mobility anisotropy >1 on the top interface corresponds to preferred charge transport along the coating direction. Revisiting the GIWAXS results (**Figure 2.3b**), the interfacial morphology anisotropy and the charge transport anisotropy consistently point to preferred charge transport along the polymer backbone (**Figure 2.5g**).[20, 61] It can be seen that the trend of interfacial backbone alignment (**Figure 2.3b**) does not exactly match with that of the mobility anisotropy across the concentration range/film thickness studied (**Figure 2.5g**). Specifically, the mobility anisotropy is relatively insensitive to concentration change, while the degree of backbone alignment increases significantly with increasing concentration. Despite increasing backbone alignment, the grain boundary may eventually limit the charge transport given the small fibril sizes.

Similar to the top interface, the mobility anisotropy at the bottom interface shows a strong correlation with the backbone alignment in the bulk, which corroborates our hypothesis that the bottom interface has similar morphology as the bulk. At the bottom interface, charge transport is preferred perpendicular to the coating direction for thinner films/lower concentrations, and becomes almost isotropic for thicker films/higher concentrations (**Figure 2.5g**). Considering a similar trend of backbone alignment in the bulk (**Figure 2.3b**), we can conclude that the charge transport again is preferred along the polymer backbone. The mobility anisotropy approaches unity starting from 10 mg/ml, while backbone orientation becomes isotropic from 18 mg/ml. We attribute this mismatch to the onset of grain boundaries limiting charge transport before the backbone alignment is completely lost. In summary, we demonstrate that the charge transport anisotropy is substantially higher at the top interface than the bottom interface, and that the high degree of interfacial alignment induces anisotropic charge transport preferably along the DPP2T-TT polymer backbone.

2.3 Discussion

The characterizations presented above indicate that the top interface exhibits a higher degree of backbone alignment at the molecular scale, larger fibrils with better in-plane orientational ordering at the meso-scale, and the resulting greater charge transport anisotropy compared to the bulk. We hypothesize that there are two key factors responsible for forming aligned nanofibers during evaporative assembly: (1) crystallization of nanofibers at the fluid-air interface due to high Peclet number and (2) alignment of nanofibers driven by the extensional character of the capillary flow at the fluid-air interface.

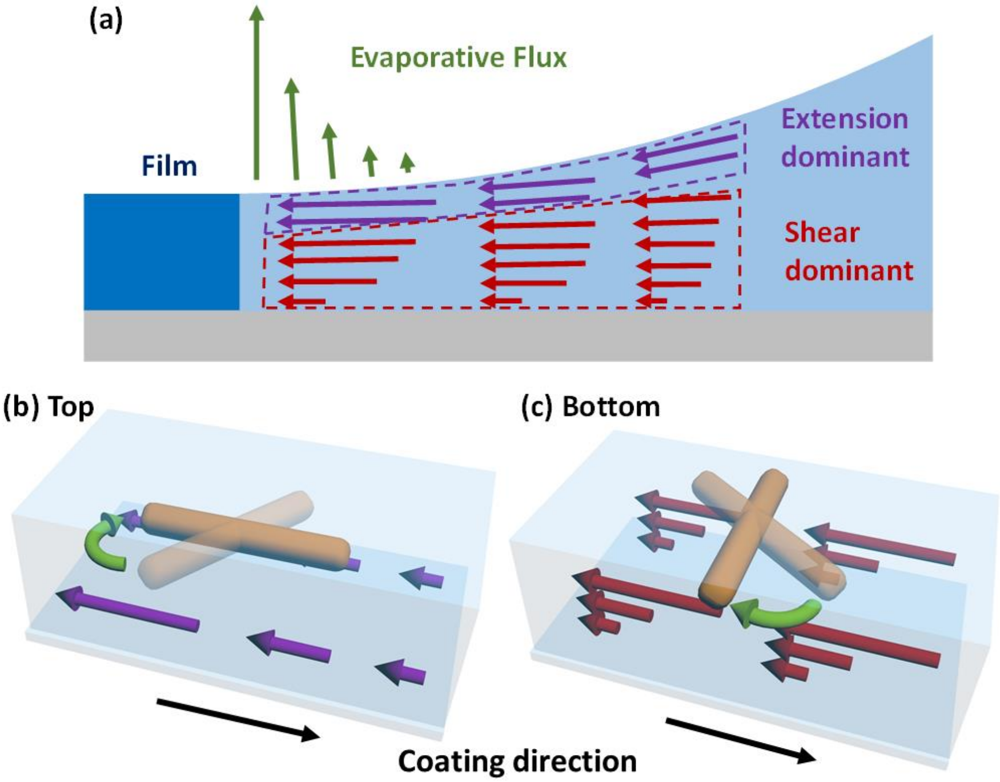

Figure 2.6. Illustration of alignment mechanism. (a) Schematic of the transport processes near the meniscus contact line. (b) Three-dimensional view of the in-plane alignment mechanism for an anisotropic particle in the extensional flow field. (c) Three-dimensional view of the in-plane alignment mechanism for an anisotropic particle in a shear flow field. Purple and red arrows denote the velocity vectors in the flow field and green arrows denote the direction of rotation.

We first infer that the distinct interfacial morphology from that of the bulk is caused by the skin layer formation. In other words, the polymer crystallization starts from the top fluid-air free interface, which inhibits the evaporation of the bulk solution and delays the formation of polymer fibrils in the bulk. Compared to the bulk, longer fibrils on the free fluid-air interface experience stronger alignment effect in an extensional flow field to out-complete rotational Brownian motion. This results in higher degree of alignment on the top interface vs. in the bulk. The inference of skin layer formation is based on estimation of the dimensionless Peclet number. Peclet number compares two competitive time scales: the rate of solvent evaporation across the liquid-air interface that establishes a vertical concentration gradient, with the rate of solute mass transport in the meniscus that diminishes the concentration gradient. We note that the estimation yielded an average Peclet number in the meniscus and did not account for its variation along the coating direction. We obtained high Peclet number Pe = 33 by estimating both time scales (details in the supporting information). A high Peclet number indicates that the rate of solvent evaporation is significantly higher than that of mass transport to result in a higher polymer concentration at the top interface. Therefore, we infer that polymer crystallization ensues on the top interface when a critical concentration is reached to induce nucleation. In addition to skin layer formation, extensional flow near the liquid-air interface may also promote polymer nucleation.

To drive in-plane alignment of as-formed polymer fibrils at the top surface, either an extensional flow or shear flow should exist. Previous works have attributed in-plane alignment to shear flow.[25, 63, 67, 88] However, shear rate at the liquid-air interface is zero mandated by the boundary condition of a free surface, and therefore does not provide the driving force for alignment at the top surface. We propose that the polymer interfacial alignment is instead directed by extensional flow on the top surface, and that the difference in orientation ordering at the top surface vs. in the rest of the film is caused by distinct flow characteristics on the top (extension dominant) vs. in the bulk (shear dominant) of the fluid layer. The rationale is detailed below. According to previous studies, strong extensional flow exists at the top surface due to increasing solvent evaporation rate moving towards the contact line.[89, 90] Going from the free surface towards the bottom substrate, the flow type transitions from extension dominant to shear-dominant, bound by the non-slip boundary condition at the bottom interface in contrast to the zero shear boundary condition at the free surface (**Figure 2.6a**).[91, 92] This flow type transition can result in distinct anisotropic particle alignment in the two different zones. For instance, Trebbin and coworkers observed, in a flow passing through an expanding channel, different orientation of fibrillary micelles in a shear dominant zone near the channel wall compared to an extension dominant zone at the channel center.[93] Simulation studies show that extensional flow is capable of aligning anisotropic particles due to differential drag along the particle.[94, 95] In the extensional flow field, the front end of a polymer fibril experiences stronger drag force than the back end. The net torque applied on the fibril is negative, rotating the fibril clockwise to align its long axis along the flow direction near the free surface (**Figure 2.6b**). In shear flows, vorticity tensor plays a dominant role instead in aligning the long axis of anisotropic particles along the vorticity tensor.[96, 97] Because the vorticity tensor is parallel to the contact line and perpendicular to the coating direction (more discussion in the supporting information), short polymer fibrils are aligned orthogonal to the coating direction in the bulk and near the bottom substrate (**Figure 2.6c**). The extent of orientiation ordering is much lower in this case, possibly due to the relatively weak effect of shear on particle rotation.[98] The alignment mechanism proposed agrees with our morphology models built based on the GIWAXS and AFM measurements (**Figure 2.4h**). Summarizing the above discussion, we can conclude that the reasons for the better in-plane alignment near the top surface than in the bulk are the crystallization of elongated fibers at the ink-air interface, and the evaporation driven extensional flow in the top layer.

In the context of the proposed alignment mechanism during meniscus-guided solution coating, the effect of polymer concentration on alignment can also be discussed. At the top interface, the degree of alignment of polymer fibrils increases with increasing solution concentration (**Figure 2.3**). It is because polymer fibrils crystallize earlier at higher starting concentrations under the same evaporation rate (**Figure B1**), leaving more time for fiber growth and reorientation under extensional flow. Thus, the in-plane alignment increases monotonically with solution concentration. On the other hand, the in-plane orientation of the polymer fibrils becomes more isotropic in the bulk of the film when the concentration increases. At higher starting concentration, the liquid film trapped underneath the skin layer is thicker given earlier onset of crystallization. Since the shear flow is imposed by the non-slip boundary condition at the substrate, thicker liquid layer weakens the effect of shear-induced alignment outcompeted by the Brownian motion to decrease the degree of alignment in the bulk of the solidified film.

2.4 Conclusion

In summary, we fabricated DPP2T-TT thin films and OFET devices using meniscus-guided coating, and observed backbone alignment and charge transport anisotropy at the air-film interface distinct from that in the bulk of the film. Revealed by GIWAXS, AFM and polarized UV-Vis, the polymer fibrils near the top interface exhibit a significantly higher degree of alignment than the bulk under most conditions studied. Specifically, well-defined polymer fibrils were observed at the top interface, with long axis and the polymer backbone aligned along the coating direction. In contrast, the bulk fibrils were significantly smaller, either weakly aligned transverse to coating or close to isotropic. Correspondingly, the charge transport at the air-film interface showed markedly higher mobility anisotropy while the charge transport at the film-substrate interface remains weakly anisotropic or almost isotropic. Interestingly, the charge transport prefers to occur along the polymer backbone direction, even in the cases when the fibrils were only weakly aligned. We hypothesize that the in-plane alignment of the DPP2T-TT fibers are driven by the extensional flow from fluid recirculation at the ink-air interface near the contact line. Nanofibers form near the interface where a concentration gradient occurs due to the high evaporation rate, and are aligned by the extensional flow. This alignment mechanism can be a reference for molecular or deposition process design to achieve high degree of alignment in conjugated polymer thin films for both kinetic studies and charge transport characterizations.

2.5 Experimental Section

Substrate treatment. Octyldecyltrichlorosilane (Acros 95%) was used to perform substrate treatment to reduce charge traps for device fabrication. The ODTS was stored in the refrigerator at 4 ºC and was removed from the refrigerator before sample preparation. In the glovebox, 100 µl of ODTS was transferred into a 1 ml syringe and 50 ml of anhydrous trichloroethylene was transferred to a 250 ml bottle. A 4 inch Si wafer with a 300 nm thick SiO_2 layer was plasma treated for 6 minutes and placed in a glass petri dish. The ODTS was injected into the trichloroethylene and the mixture was poured into the petri dish. The petri dish was covered and sealed with aluminum foil and parafilm. The reaction was left at room temperature for 20 minutes. After reaction, the wafer was removed from the solution and was rinsed with toluene. The dry wafer was placed on a hot plate at 120 ºC for 2min to induce 2D crystallization of ODTS before removal and storage.

Synthesis of DPP-TT. The conjugated polymer DPP2T-TT (Mn = 20,000 g/mol, Mw = 104,000 g/mol, PDI = 5.2) was synthesized following a previous published procedure.[99] 3,6-bis(5-bromothiophen-2-yl)-2,5-bis(4-decyltetradecyl) pyrrolo[3,4-*c*]pyrrole-1,4(2*H*,5*H*)-dione (300.0 mg, 265.2 mmol) and 2,5-bis (trimethylstannyl)thieno[3,2-*b*]thiophene (123.5 mg, 265.2 mmol) were dissolved in 20 mL of toluene in a 35 mL microwave reaction vessel. The solution was purged with nitrogen for 15 minutes, before tris(*o*-tolyl)phosphine (3 mg) and Tris (dibenzylideneacetone)dipalladium(0) (6 mg) were added. The vessel was sealed with a snap cap and quickly transferred to a CEM Discover Microwave Reactor. Reaction conditions were listed as follows: Power cycling mode; Power, 300 W; Power cycles, 100; Temperature, 120 – 150 °C; Heating, 120 s; Cooling, 30 s; Pressure, 150 psi; Stirring, high. After the reaction was complete, the polymer was collected by precipitation into methanol. The product was dissolved in 50 mL of chloroform and palladium was removed with 30 mg of *N*,*N*-diethylphenylazothioformamide at 50 °C for 30 minutes. The solution was precipitated into methanol and the solid was dried under 60 °C over high vacuum.

Film preparation. Polymer DPP2T-TT was dissolved in chloroform (Macron ACS grade) at 25 mg/ml and stirred overnight in nitrogen environment to ensure dissolution. DPP2T-TT thin films were deposited onto substrates by a meniscus-guided coating method using an ODTS-treated Si blade.[72, 73] The meniscus-guided coating setup involves a stationary substrate and a moving blade, with ink solution sandwiched in-between. The blade was tilted by 7º, with the blade edge set 100 μm above the substrate surface for the film deposition process. The speed of the blade was 0.5 mm/s for all samples and the substrate temperature was fixed at 25 ^{0}C. The solution was diluted to designated concentration during film deposition. For microscopy, AFM and GIWAXS, DPP2T-TT films were prepared on ODTS-treated SiO_2-Si substrates and for UV-Vis spectroscopy, films were prepared on ODTS-treated glass slides.

UV-Vis spectroscopy. Solid-state transmission UV-Vis spectroscopy measurements were performed on the Agilent Cary 60 UV-Vis spectrometer. DPP2T-TT thin films coated on ODTS-treated glass substrates were mounted on the solid sample holder with a vertical polarizer sheet. The scans were taken from 400 nm to 1000 nm.

Atomic force microscopy measurements. AFM measurements were performed on the Asylum Cipher AFM with Tap300Al-G tapping mode AFM tips. The top air-film interface scans were performed on the films as prepared on substrates. The film-substrate interface scans were performed on laminated films on PDMS. The PDMS stamp for lamination was prepared by mixing Momentive RIV615 silicone potting compound and cross linking agent RTV615 by the volume ratio of 10:1. The mixture was sufficiently mixed and poured into a clean plastic petri dish until the liquid layer thickness is ~5 mm. The petri dish with polymer was placed in a house vacuum oven at 50 ^{0}C for 2 hours. Low curing temperature was chosen to ensure stickiness of the PDMS surface to facilitate film transfer. After curing, the PDMS stamp was cut and placed onto a newly coated polymer film. The PDMS stamp was gently pressed on the film and quickly lifted from one corner to transfer the film from the substrate. AFM scans was performed on the exposed bottom interface of film on PDMS. Linecuts with 30 pixel line width along the horizontal direction and with 5^o offset along the vertical direction were performed on the top surface FFT images. Raw data was smoothened to reduce the noise from the pixelated FFT images. Peak deconvolution was performed to separate the 1st order peak in the center and the 2nd order arc. The 2nd order peak was fitted with a Gaussian function to obtain the peak position, peak area and the full width half maximum (FWHM).

Small angle neutron scattering. Small angle neutron scattering (SANS) experiments were performed at the National Institute of Standards and Technology Center for Neutron Research (NIST CNR) in Gaithersburg, MD. SANS measurements were performed on the NGB 30m beamline at three detector positions to obtain the scattering intensity, I(q), over a wide q-range ($0.004 < q$ (Å−1) < 0.4).[100] DPPTT was dissolved in d-chloroform (D > 99.8%, Cambridge Isotopes) by mixing for 6 hours prior to loading in a 1 mm pathlength demountable cells with quartz windows. The total scattering was normalized to the incident beam flux, corrected for background scattering (e.g., empty cell and solvent) and 2D profiles were then converted to 1D profiles using standard methods.[101] Smeared model fitting was performed using DANSE SASView software.[102]

Grazing incidence wide angle X-ray scattering. GIWAXS measurements were performed at beamline 8-ID-E of Advanced Photon Source at the Argonne National Laboratory.[103] Data were collected with an incident beam energy at 7.35 keV on a two-dimensional detector (Pilatus 1M) at two different positions and the images combined to eliminate most of the inactive pixels using the GIXSGUI package written for Matlab.[49] GIXSGUI was also also used to apply corrections for detector nonuniformity, beam polarization, and detector sensitivity, and to reshape the 2-dimensional data into the representation q_z vs q_r (= $\sqrt{q_x^2 + q_y^2}$). Experiments were carried out in a helium chamber. The incident angle was set at 0.2 degree for bulk measurements and 0.08 degree for surface measurements. For calculating the π-π stacking anisotropy, P, we extracted the intensity of the edge-on portion of the π-π stacking peak from both parallel and perpendicular scans, by performing a sector cut of $-88^0<\chi<-83^0$ from the raw data image. Peak deconvolution was performed to separate the π-π stacking peak from the amorphous peak, the background scattering and the peak from crystalline ODTS. The π-π stacking peak was fitted with a Gaussian function to obtain the peak position, peak area and the full width half maximum (FWHM).

Device fabrication and characterizations. Bottom gate top contact configuration was used to measure charge transport at the bottom interface. For BGTC device fabrication, DPP2T-TT/chloroform solution was coated on ODTS treated 300 nm SiO2-Si substrates and gold source-drain electrodes were evaporated on top of the DPP2T-TT thin film. For TGBC device fabrication, DPP2T-TT/chloroform solution was coated on substrates with evaporated gold source-drain electrodes. On the DPP2T-TT film, we next spin-coated a layer of CYTOP®, a trademarked fluorinated polymer dielectric with low trap density, and evaporated another gold layer was evaporated on top as the gate electrode. Specifically, the source and drain electrodes were 35 nm thick Au deposited by thermal evaporation. The channel length and width were 70 μm and 4500 μm respectively. Top gate bottom contact configuration was used to measure charge transport at the top interface. The source and drain electrodes had same dimensions as in the BGTC configuration deposited by the same method. A 447±3 nm CYTOP layer was spin-coated at 2000 rpm for 1min on top of the electrodes and polymer thin film serving as a dielectric. Immediately after spin coating, the CYTOP film was annealed at 100°C for 30min on a hot plate. A 35 nm gold Au layer was thermally evaporated on the CYTOP layer as a gate. Keysight B1500A analyzer was used for all FET device measurements in a glove box under nitrogen environment. The BGTC devices were measured as deposited and the TGBC devices were measured after annealing for CYTOP crosslinking. Gate bias between 0 to -100 V with drain voltage of -100 V was applied for BGTC device measurements and between 0 to -60 V with drain voltage of -60 V was applied for TGBC device measurements to avoid device burning. The apparent mobility in the saturation regime was calculated using the equation $\mu_{sat} = \frac{2L}{WC_i}\left(\frac{d\sqrt{I_{SD}}}{dV_G}\right)^2$. The capacitance for the 300 nm SiO_2 layer and the CYTOP layer is estimated with $C = \frac{\varepsilon\varepsilon_0}{d_0}$ where ε is the relative permittivity of the insulator (3.9 for SiO_2 and 2.1 for CYTOP), ε_0 is the air permittivity and d_0 is the thickness. The capacitance of CYTOP was calculated to be 4.2 nF/cm^2. With consideration of the influence of the ODTS layer,[104] the capacitance of SiO_2 used for calculation is 11 nF/cm^2.

Chapter 3

Understanding Film-to-Stripe Transition of Conjugated Polymers Driven by Meniscus Instability [3]

3.1 Introduction

Meniscus-guided solution coating has been widely adopted as a highly effective fabrication method for high-throughput, low-cost and large-area coating of functional materials. The evaporating, moving meniscus during the coating process entails highly complex and coupled transport and assembly processes often occurring at far-from-equilibrium conditions.[105] The interplay between solvent evaporation, viscous drag-out, ink dewetting, phase transition and capillary/Marangoni flows frequently gives rise to meniscus instability which critically influence the final morphology of the deposit. Meniscus instability can lead to material deposition into clusters, lines, stripes, hyperbranched patterns, etc. with various spacings and topologies.[106-109]

Meniscus-instability-driven morphology transition of the deposit has been commonly observed in solution coating or evaporative assembly of colloid and polymer materials.[108-111] The morphology transition can be introduced by combination and competition of various factors, including Marangoni flow and capillary flow near the contact line, meniscus pinning force and depinning force at the deposit front, wetting and dewetting of the ink solution on the substrate and the solid deposit, etc. Farcau and coworkers observed deposit morphology transition in blade-coated Au nanoparticles assemblies from stripes parallel with the contact line to islands of clusters,

---

[3] The contents of this chapter appear in Qu, G.; Kwok, J.; Mohammadi, E.; Zhang, F.; Diao, Y. "Understanding Film-to-Stripe Transition of Conjugated Polymers Driven by Meniscus Instability". *ACS Applied Materials & Interfaces*. **2018**, 10, 40692-40701

followed by the emergence a different type of stripes perpendicular to the contact line when decreasing the substrate temperature.[111] Yabu and coworkers observed the morphology transition in blade coated PMMA layer from horizontal stripes to ladder-shaped structures while increasing the polymer concentration.[109] Deblais et al. observed transition of uniform liquid film into stable liquid filament along the coating direction during blade coating of shear thinning polymer solution within a specific range of capillary number.[106] Although morphology transition was commonly observed during evaporative assembly and solution coating/printing, there is rarely quantitative study and models for describing to occurrence of morphology transition.

Past studies have revealed that morphology from molecular to macroscale in solution-coated organic semiconductor (OSC) thin films critically influences the charge transport characteristics.[25, 31, 34, 53, 72, 84, 112-114] During solution coating, the meniscus motion and instability can directly impact the deposit morphology and therefore influence the charge transport properties. On the other hand, the meniscus instability – thin film morphology – charge transport property relationship has not been studied before. Such understanding can enable better control over thin film morphology, offer strategies to pattern stripe/dot arrays for transistor fabrications and to modulate electronic properties in printed devices.

In this work, we observe coating speed dependent film-to-stripe transition during meniscus-guided solution coating of multiple donor-acceptor conjugated polymers and studied in detail this phenomenon in poly(diketopyrrolopyrrole-*co*-thiophene-*co*-thieno[3,2-b]thiophene-*co*-thiophene) (DPP2T-TT) thin films. At a critical transition speed, thin films and stripes were deposited interchangeably. Interestingly, different molecular stacking and a three-fold higher charge carrier mobility is measured from devices made of stripes compared to thin film devices deposited at the same condition. To understand the underpinning mechanism of morphology transition, we employ high-speed imaging and develop image analysis algorithm to discover two distinct regimes of stick-and-slip meniscus instability before and after the transition, which drastically differ in terms of stick-and-slip frequency and amplitude. We hypothesize that such regime change is driven by increasing system energy with increasing coating speed in the high-frequency, low-amplitude stick-and-slip regime, which transitions to low-frequency, high amplitude stick-and-slip regime after crossing a critical speed to lower the overall system energy. This hypothesis is successfully validated by the surface free energy model developed in this work. Our work is a significant first step towards quantitative understanding of meniscus-instability-driven morphology transition during evaporative assembly and/or solution coating of functional materials.

3.2 Results and Discussions

Morphology characterizations. We employed a simple meniscus-guided coating method[31, 34, 72, 73] (**Figure 3.1a, b**) to deposit DPP2T-TT conjugated polymer (**Figure 3.1c**) and studied the morphology of the deposit as a function of coating speed. In brief, DPP2T-TT / chloroform solution was placed between an octadecyltrichlorosilane (ODTS) functionalized SiO_2 substrate and a 7° tilted blade. Translational blade movement at various speeds drove evaporative assembly of DPP2T-TT, producing thin film or stripe deposition on the substrate. The solution concentration was fixed at 5 mg/ml and the substrate temperature at 25 °C. When the coating speed increased from 0.3 to 2 mm/s, we observed morphology transition of DPP2T-TT deposit from continuous film (**Figure 3.1d,e**) to periodic stripe array (**Figure 3.1f, g**). The two regimes were bisected by a critical coating speed of 1mm/s, while around the critical speed, film patches and stripe arrays coexisted (**Figure 3.1f**). Coating speeds beyond 2 mm/s were not shown as no deposition occurred due to ink dewetting. To compare the differences in morphology characteristics from molecular to macroscale and in charge transport properties, we characterized the films vs. stripes employing a suite of methods including cross-polarized optical microscopy (C-POM) for overall morphology and alignment, grazing incidence wide angle X-ray scattering (GIWAXS) for molecular packing and orientation, atomic force microscopy (AFM) for mesoscale morphology and field-effect transistor (FET) device measurements for charge transport properties.

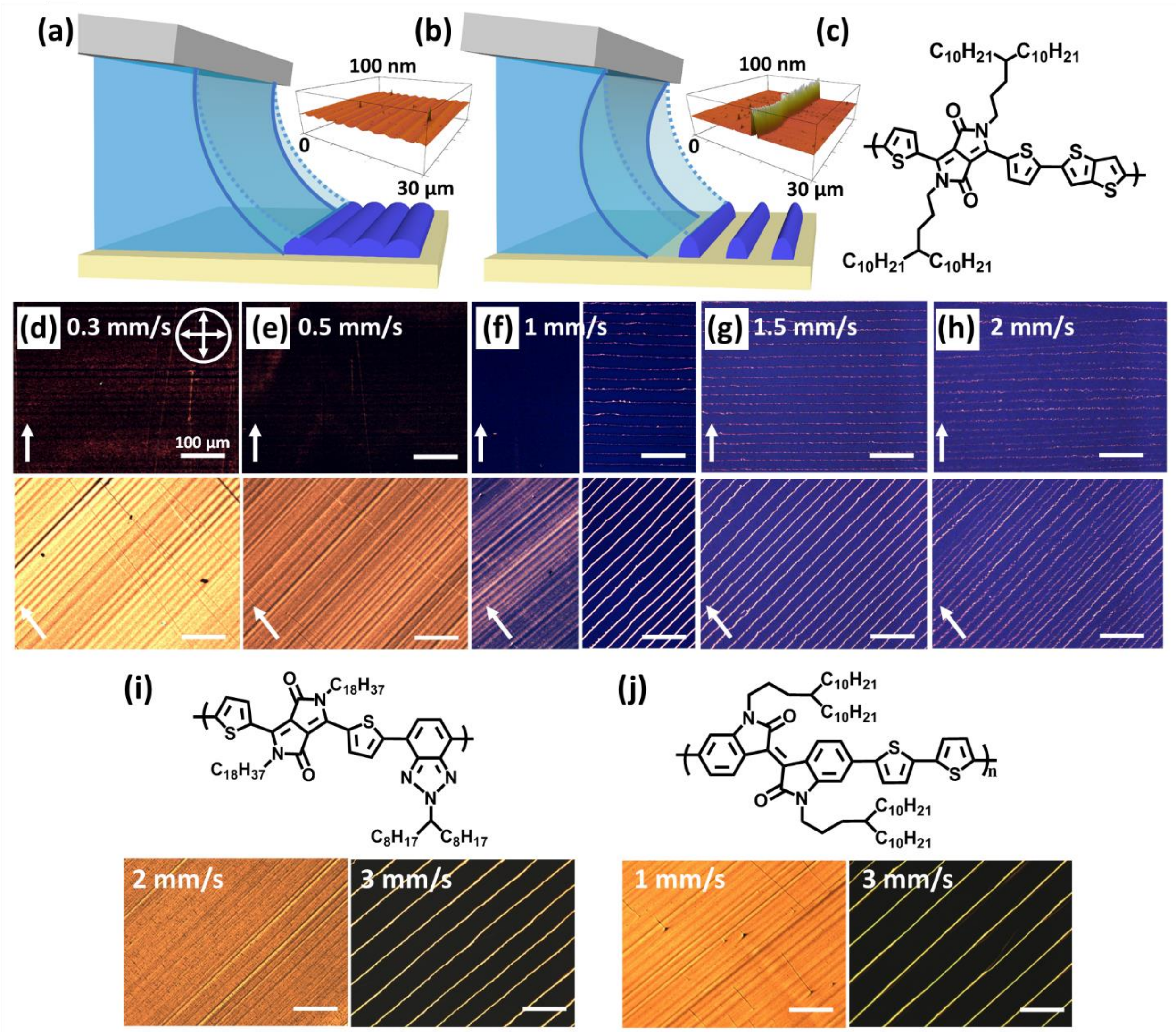

Figure 3.1. Schematics of meniscus-guided coating of DPP2T-TT for (a) film deposition and (b) stripe deposition with stick-and-slip meniscus motion. The dotted lines and the solid lines represent the meniscus position before and after slipping, respectively. The 3D AFM image insets represent morphology of film coated at 0.9 mm/s and stripe coated at 1.5 mm/s coating speed. The AFM insets are not to scale as to better compare the morphology difference between film and stripes. Real scale SEM images are included in **Figure C6**. (c) Molecular structure of DPP2T-TT. (d-h) Cross polarized optical microscopy images of DPP2T-TT coated from 5 mg/ml chloroform solution at (d) 0.3 mm/s, (e) 0.5 mm/s, (f) 1 mm/s, (g) 1.5 mm/s and (h) 2 mm/s. Deposit morphology transition occurs at 1 mm/s where film and stripe coexist. The crossed arrows indicate the cross polarizer orientation. The arrow at the lower left of each image indicates the coating direction. The top row of images were with the coating direction aligned along a polarization axis of the light and the bottom row were obtained with the coating direction at 45^0 from the polarization axis. (i) DPP-BTz molecular structure and morphology transition coated from 5 mg/ml toluene solution at 2 mm/s and 3 mm/s. (j) PII-2T molecular structure and morphology transition coated from 5 mg/ml toluene solution at 1 mm/s and 3 mm/s. All scale bars are 100 µm.

To visualize the overall deposit morphology and the global molecular alignment, we performed C-POM complemented with AFM measurements on DPP2T-TT films (thickness 20-80 nm) and stripes (height 70-120 nm). Both methods revealed periodic undulation on the top surface of the DPP2T-TT thin films (**Figure 3.1d-f**), forming stripes parallel to the meniscus front. Together with the regularly spaced stripes (**Figure 3.1f-h**), we infer that meniscus stick-and-slip instability occurs during both film and stripe deposition, however, at drastically different frequencies (150 – 300 s^{-1} for film deposition and 40 – 100 s^{-1} for stripe deposition depending on the coating speed). The spacing between stripes also systematically decreased with increasing coating speed (**Figure 3.1f-h**). Meanwhile, the amplitude of the undulation on films was also significantly different from the stripe thickness, which was <10 nm for films and ~100 nm for stripes (**Figure 3.1a, b insets**). Furthermore, when we rotated the substrates from 0° and 45° under cross-polarizers, we observed clear birefringence which indicated that the polymer backbone in the deposited film and stripes is preferentially aligned either along or transverse to the coating direction (**Figure 3.1 d-h**). Similar film-to-stripe morphology transition was observed in other conjugated polymer systems including poly[[2,5-bis(2-octadecyl)-2,3,5,6-tetrahydro-3,6-diketopyrrolo[3,4-c]pyrrole-1,4-diyl]-alt-(2-octylnonyl)-2,1,3-benzotriazole] (DPP-BTz) and poly[3,3’-bis(4-decyl-1-tetradecyl)- 6,6’-bis(thienyl-5-yl)-isoindigo] (PII-2T) (**Figure 3.1i, j**), indicating generality of this phenomenon. To quantify the polymer alignment and the molecular packing, we next performed grazing incidence wide angle X-ray scattering to compare film with stripe samples using DPP2T-TT as the model system.

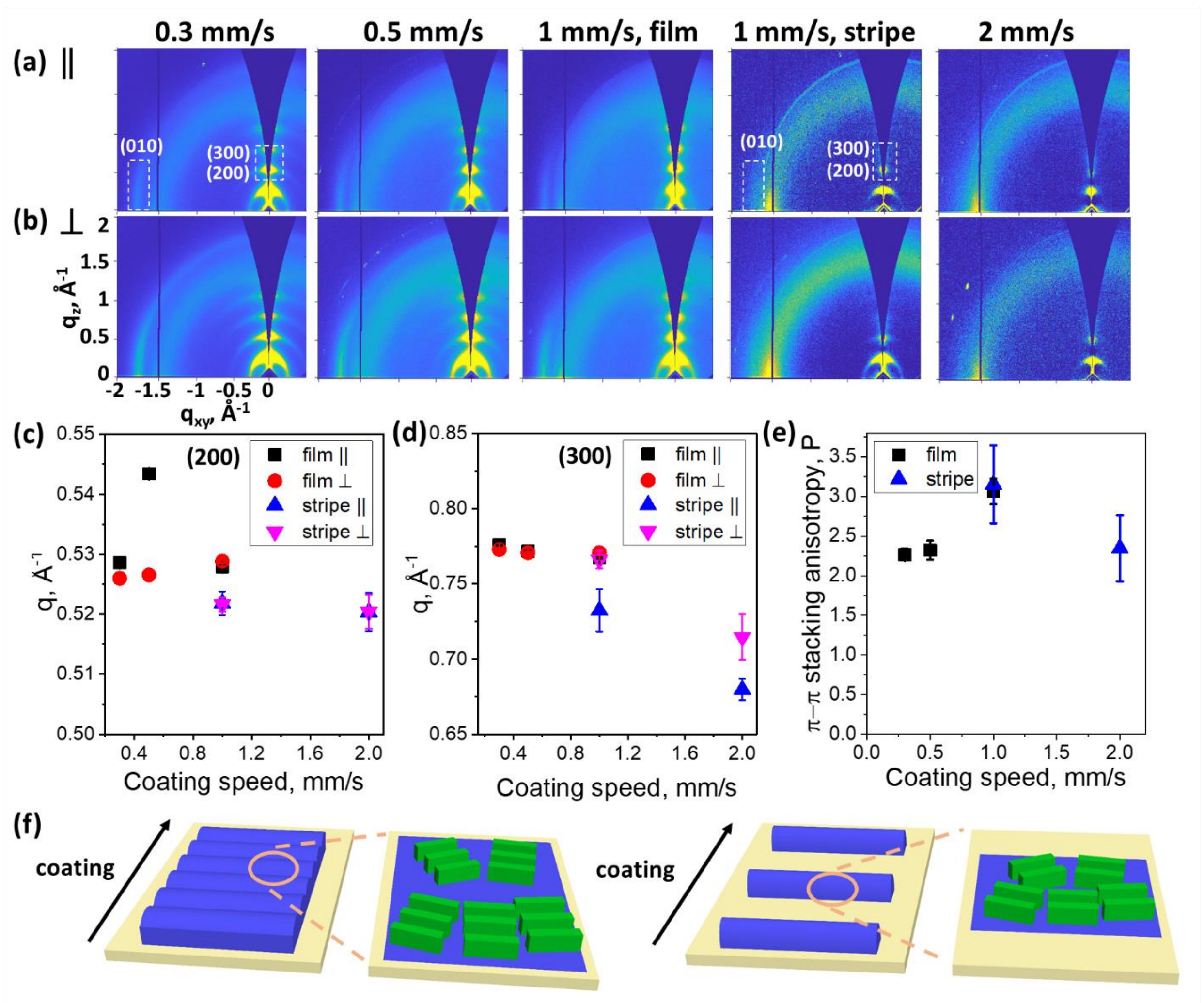

Figure 3.2. GIWAXS diffraction patterns from (a) parallel and (b) perpendicular measurements on the following samples: 0.3 mm/s film, 0.5 mm/s film, 1 mm/s film, 1 mm/s stripe and 2 mm/s stripe. Herein the parallel and perpendicular refer to the relative orientation of the X-ray incidence beam with respect to the coating direction. (c-d) Reciprocal q-spacing of the (c) (200) and (d) (300) lamellar stacking peaks comparing films vs. stripes. (e) In-plane π-π stacking anisotropy calculated as the ratio of perpendicular (010) π-π stacking peak area vs. the parallel peak area. (f) Inferred morphology model of film (upper) and stripe (lower) deposit. Green bricks represent the polymer backbone.

Through GIWAXS measurements, we compared the molecular packing details in film vs. stripes by analyzing the π-π and lamella stacking peaks (**Figure C1-4**). We also determined the polymer backbone alignment in film vs. stripes by comparing the π-π stacking peak intensities measured with the sample coating direction parallel vs. perpendicular to the incidence beam (**Figure** 错误!

未找到引用源。**.2**). The (010) π-π stacking peak from film samples predominantly appeared as 'edge-on' around q ≈ 1.74 $Å^{-1}$, corresponding to ~3.61 Å π-π stacking distance. The lamella stacking distance in film samples remained ~ 24 Å determined from (200) and (300) peaks. Upon film-to-stripe transition at 1mm/s, the π-π stacking distance was slightly reduced in stripes (**Figure C1a, C3**), whereas the lamella stacking distance moderately increased at the same time (**Figure C1b,c**). The difference in molecular packing of stripes vs. films was further manifested in the significant shift in higher order lamella stacking peaks, wherein the (200) and (300) peaks shows distinct average peak positions comparing the film and stripe regime (**Figure C4c,d**). The change in the peak position and the FWHM of the (200) and (300) lamellar stacking peak (**Figure C4c,d, C1b,c**) clearly suggest larger lamellar stacking distance and increased disorder in stripes in comparison to films.

Regarding polymer backbone alignment in-plane (parallel to the substrate plane), we observed more intense edge-on π-π stacking peak when the incidence beam was perpendicular to the sample coating direction than the parallel case at all conditions (**Figure 3.2a,b**), indicating preferred backbone alignment orthogonal to the coating direction. We quantified the degree of backbone alignment in-plane by evaluating the π-π stacking anisotropy, P, defined as the ratio of edge-on π-π stacking peak areas between perpendicular vs. parallel measurements, with P > 1 indicating a preferred perpendicular backbone alignment. **Figure 3.2e** plotted P with respect to the coating speed for both the film and stripe morphology. We observed a maximum P = 3.1 at 1 mm/s at the transition coating speed. Interestingly, the drastic change in morphology from film to stripe did not influence the backbone alignment as P values were nearly identical for film and stripe at the same coating speed of 1mm/s. Despite the morphology transition, P remained > 1 across all speeds tested, meaning the polymer backbone in both film and stripes preferably aligned orthogonal to coating and parallel to the long axis of stripes on the film and the long axis of the stripes **(Figure 3.2f)**.

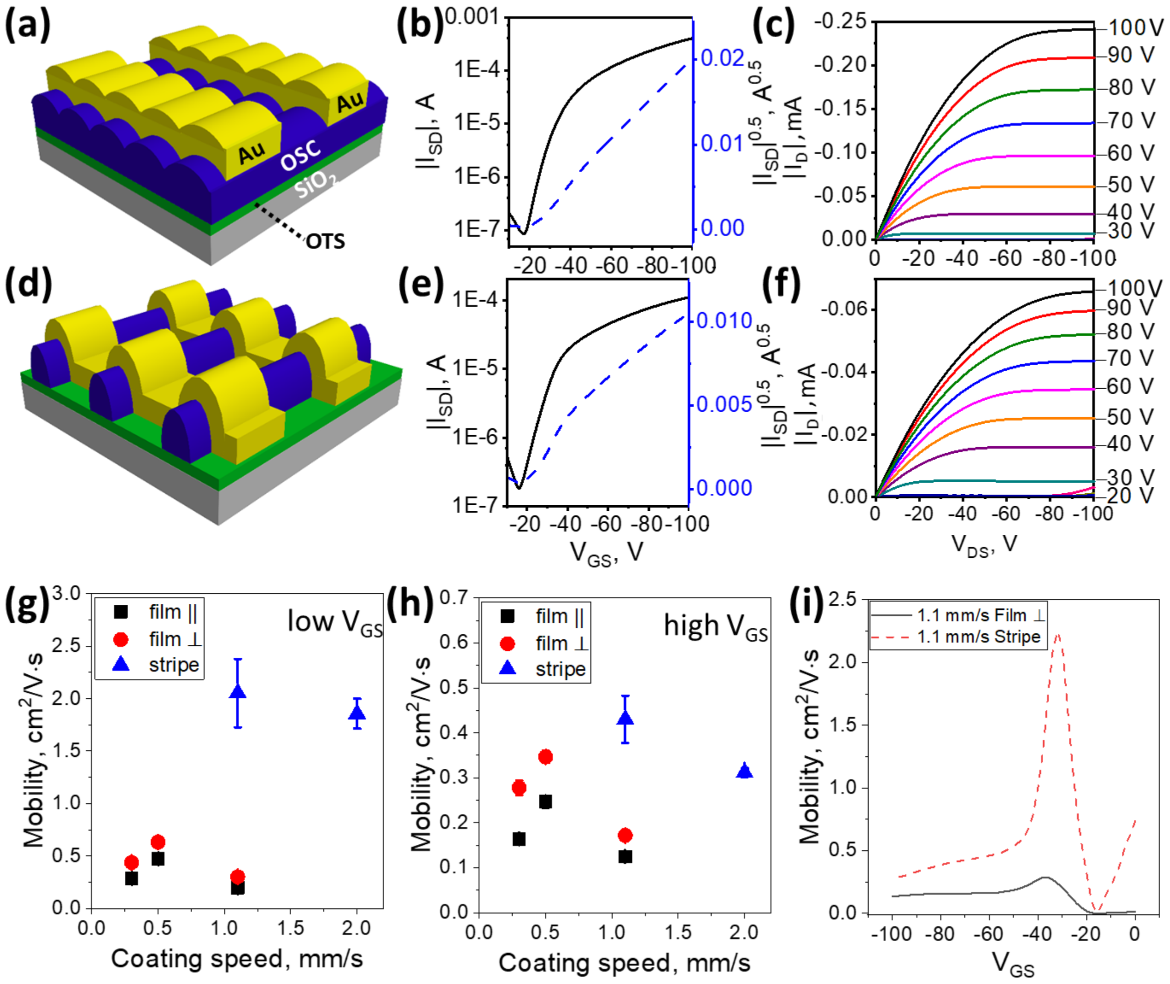

Figure 3.3. FET device configuration and performance of DPP2T-TT with (a-c) film morphology and (d-f) stripe morphology. (b) and (e) are representative transfer curves corresponding to film and stripe coated at 1 mm/s, respectively. (c) and (f) are representative output curves at the same condition. (g, h) Comparison of charge carrier mobilities measured at (g) low V_{GS} (-20V to -50V) and (h) high V_{GS} (-50V to -100V) in the saturation regime. The source-drain voltage V_{DS} was -100 V. For films, measurements were performed both parallel and perpendicular to the coating direction, whereas stripes perpendicular to coating only. For charge transport mobility of stripes, channel width was corrected by multiplying the number of stripes in the channels with the stripe width. Number of stripes was obtained by dividing the total channel width (7500 μm) by the stripe pitch (**Figure C9**). (i) Mobility vs V_{GS} plot comparing 1.1 mm/s perpendicular film and 1.1 mm/s stripe.

FET device characterizations. After determining the molecular stacking and alignment from GIWAXS, field-effect transistor (FET) devices were fabricated with DPP2T-TT films and stripes. Bottom-gate, top-contact FET device architecture was used with bottom-to-top layers of Si wafer / 300 nm SiO_2 and ODTS / DPP2T-TT / 35 nm Au (**Figure 3.3a, d**). Charge transport was measured parallel and perpendicular to the coating direction for films, but only perpendicular to coating for stripes due to their narrow line width. In all cases, we observed non-ideal transport characteristics, exhibited as “kinks” in the transfer curves (**Figure 3.3b, e**), possibly due to gate-voltage dependence of contact resistance or simultaneous injection of holes and electrons.[86, 87, 115] To avoid misinterpretation of the charge carrier mobility, the apparent saturation mobilities were extracted from both the low V_{GS} region before the kink (-20 V to -50 V) and the high V_{GS} region after the kink (-50 V to -100 V), plotted in **Figure 3.3g** and **3.3h** respectively. The mobility versus V_{GS} plot comparing film vs. stripe devices at the same speed was shown in **Figure 3.3i**. The maximum mobility was observed for stripes coated at 1.1 mm/s with channel width correction, which was 3 times higher than the average mobility in films coated at the same condition. Such a large difference in apparent mobility of films vs. stripes was surprising considering similar degrees of molecular alignment based on the GIWAXS study. X-ray measurements are capable of revealing morphologies at different length scales,[80, 116, 117] where FET performances can be critically influenced. With analysis on the π-π stacking and the lamellar stacking peaks comparing peak position and FWHM (**Figure C1**), we found different molecular stacking distances and levels of paracrystallinity between film and strips deposited at the same condition, which may give rise to the mobility difference. We also speculated that stripes may exhibit higher degree of crystallinity with slower deposition rate, leading to higher charge carrier mobility in stripes. In terms of charge transport anisotropy in films, we observed moderately higher mobility perpendicular to the coating direction (**Figure C5**), consistent with our prior observations.[31, 34, 47] The improved charge carrier mobility in stripes as compared to films prepared under the same condition demonstrates the potential advantage of leveraging meniscus instability for printing high performance as well as patterned transistor arrays.

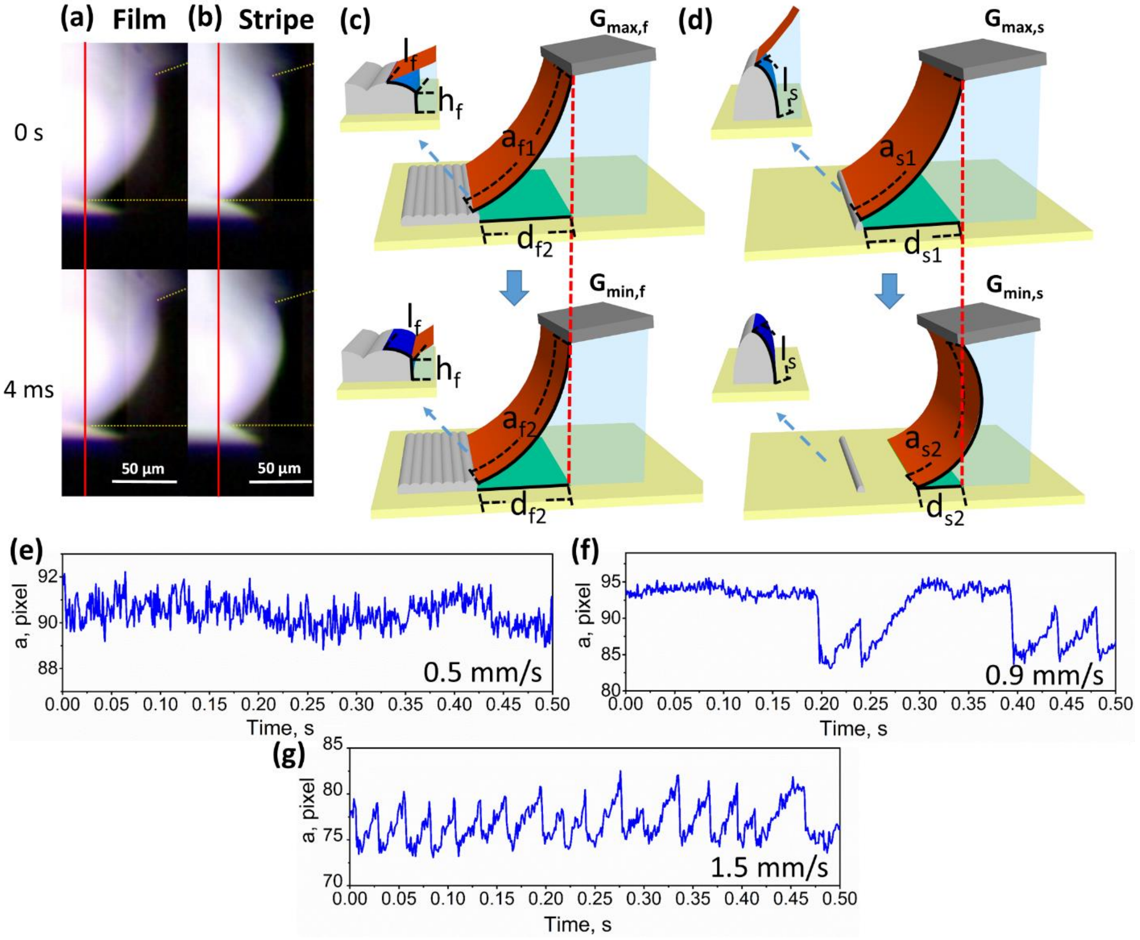

Figure 3.4. High speed imaging of the meniscus motion (side view) comparing (a) film deposition at 0.7 mm/s and (b) stripe deposition at 0.9 mm/s in 4 ms time period. (c-d) Schematics of the meniscus right before and right after slipping (with G_{max} and G_{min}, respectively) during stick-and-slip motion for (c) film and (d) stripe deposition. The interfaces contributed to the system surface free energy model were highlighted; they are the meniscus free surface (red), the contact area between the ink and the substrate (green) and the contact area between the ink and the deposit (blue). The contact areas that remain unchanged between stick and slip are not shown. (e-g) Real time tracking of arc length *a* for (e) film deposition at 0.5 mm/s, (f) film and stripe deposition at 0.9 mm/s and (g) stripe deposition at 1.5 mm/s. Arc lengths were obtained from image analysis of each frame obtained at 1000 fps, or 1ms intervals.

High-speed imaging. In order to understand the mechanism of morphology transition, we performed high-speed imaging to quantitatively characterize the meniscus stick-and-slip motion and the regime change. The high speed camera was set at 1000 frames per second (fps) in transmission configuration to capture the side view of the meniscus during coating from 0.5 mm/s to 2 mm/s. The frame rate employed was sufficient for visualizing both film and stripe deposition, with high stick-and-slip frequencies for film deposition (150 – 300 s^{-1}) and low frequencies for stripe deposition (40 – 100 s^{-1}). Examples of the meniscus movement was shown in **Figure 3.4a and b** for film and stripe deposition, respectively. In film deposition, the stick-and-slip motion was more nuanced and can hardly be discerned in **Figure 3.4a** due to high stick-and-slip frequency and small slipping distance. On the contrary, during stripe deposition, the slipping event of the meniscus was very pronounced where the meniscus jumped by 10-25 μm from the prior sticking point to a new position within 4 ms. Enabled by high speed imaging, we were able to analyze the movement and the shape of the meniscus to perform the following surface free energy analysis for further understanding of the morphology transition.

Surface free energy model. Modeling and simulation studies on meniscus instability have been performed to evaluate important factors affecting patterned material deposition.[118-120] With regard to governing-equation based modeling approach for describing stick-and-slip instability, both energy balance and force balance approaches have been reported, usually applied at the threshold of meniscus depinning.[121-124] On the other hand, models that can capture regime change of stick-and-slip instability during meniscus-guided coating are rarely reported.

Inspired by the well-studied surface free energy model for stick-and-slip in an evaporating sessile drop,[121, 122] we constructed a surface free energy model for describing the meniscus stick-and-slip instability catering to the meniscus-guided coating geometry. In particular, we were interested in quantifying the surface free energy of the meniscus and correlating morphology transition with the change of surface free energy; this is considering that the surface free energy of the meniscus can fully embody the pinning and de-pining forces that govern the stick-and-slip instability, both of which originate from capillarity.[125, 126] In our model, there are three interfaces that contribute to the surface free energy of the meniscus: the meniscus free surface, the substrate-meniscus interface and the deposit-meniscus interface (**Figure 3.4c,d**); the remaining interfaces of the ink solution were not evaluated because they were considered invariant during stick-and-slip. Because the widths of the studied interfaces equal to the width of the deposit, the surface areas to be evaluated are reduced from 3D to 2D, with arc length a for the meniscus surface, drag length d for the substrate-meniscus interface and undulation l and thickness h for the deposit surfaces (**Figure 3.4c,d**). Therefore, the total surface free energy G per width of the deposit equals to the sum of the length of the interfaces multiplied with the corresponding interfacial free energy. The maximum system surface free energy G_{max} is reached when the meniscus is stretched to its maximum length before slipping, while the minimum system surface free energy G_{min} occurs when the meniscus slips to its equilibrium position with the shortest meniscus and substrate-meniscus length. For both film and stripe deposition, G_{max} represents the surface free energy of the meniscus right before slipping and G_{min} represents that right after slipping, illustrated in **Figure 3.4c and d**. For film deposition, the meniscus pins at the apex of the undulation at $G_{max,f}$ and slips to the edge of the film at $G_{min,f}$. The surface free energy (per unit width) $G_{max,f}$ and $G_{min,f}$ during film deposition can be written as the following:

$$G_{max,f} = a_{f1}\gamma_{L-V} + d_{f2}\gamma_{L-S} + l_f\gamma_{L-DPP} + h_f\gamma_{L-DPP} \qquad \text{(Eqn. 3.1)}$$

$$G_{min,f} = a_{f2}\gamma_{L-V} + d_{f2}\gamma_{L-S} + h_f\gamma_{L-DPP} \qquad \text{(Eqn. 3.2)}$$

with γ representing interfacial free energy, L the DPP2T-TT/chloroform solution, *V* the air and *S* the ODTS-treated substrate. Unlike in film deposition, the meniscus movement in stripe deposition is pronounced and involves significant changes in the interfacial areas. For stripe deposition, the meniscus is pinned at the apex of the last stripe at $G_{max,s}$ and jumps to a new position on the substrate at $G_{min,s}$. Similar to the case of film deposition, the system surface free energy $G_{max,s}$ and $G_{min,s}$ in stripe deposition can be written as the following:

$$G_{max,s} = a_{s1}\gamma_{L-V} + d_{s1}\gamma_{L-S} + l_s\gamma_{L-DPP} \qquad \text{(Eqn. 3.3)}$$

$$G_{min,s} = a_{s2}\gamma_{L-V} + d_{s2}\gamma_{L-S} \qquad \text{(Eqn. 3.4)}$$

Based on the constructed surface free energy model, we propose a hypothesis that explains the morphology transition from film to stripe during coating. We hypothesize that morphology transition occurs to lower the maximum system surface free energy G_{max} (**Figure3.5a**). With the increase of coating speed, the meniscus lengthens due to stronger viscous force imposed by the substrate, thus increasing $G_{max,f}$ (**Table C2**). On the contrary, $G_{max,s}$ should decrease instead as both the stripe height and the maximum meniscus length (judged from stripe spacing) continuously shorten with increasing coating speed (**Table C2, Figure C9**). Therefore, at a critical coating speed, $G_{max,f} = G_{max,s}$ to lead to interchangeable deposition of both film and stripe; lower (higher) than the critical speed, film (stripe) deposition is stable (**Figure 3.5a**).

To validate the hypothesis and evaluate system surface energies, we performed image analysis on the high speed videos to obtain the length scales of the interfaces in the model, discussed below. We first extracted the lengths associated with the meniscus *a* and *d* from the high speed videos by batch processing the individual frames from the video, detailed in SI. The edge of the meniscus was identified and the meniscus was fitted to determine the arc length *a*. The drag length *d* was obtained from the projection of the meniscus on the substrate plane. Examples of the fitted *a* from film (0.5mm/s), transition (0.9mm/s) and stripe (1.5mm/s) regimes were shown in Figure 4e-g respectively. The transition speed varied around 1 mm/s from batch to batch due to the sensitive dependence of meniscus instability on processing conditions. Beside a and d, the undulation half width length l_f, film thickness h and stripe half width l_s were obtained from AFM measurements (**Figure C7, 8**). We further obtained interfacial free energies (**Table C1**) of respective interfaces using a method detailed in previous publications[47, 127] and summarized in the SI. With the needed interfacial lengths and free energy values, the final system surface free energies were calculated and plotted in **Figure 3.5b**.

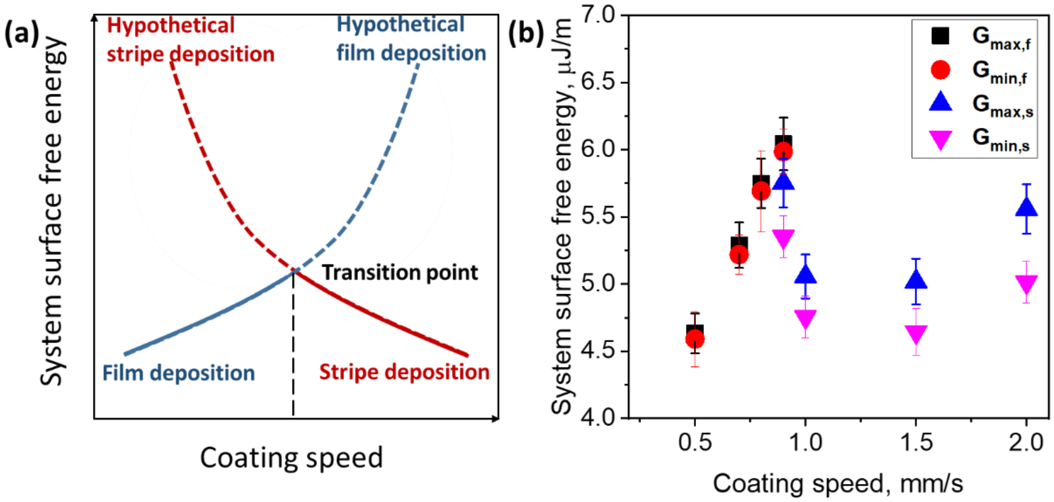

Figure 3.5. a) Hypothesized energy landscape of maximum system surface free energy $G_{max,f}$ and $G_{max,w}$ with respect to coating speed. b) Maximum and minimum system surface free energy at various speeds for film and/or stripe deposition. Error bars were from errors in length extractions from videos and interfacial free energy measurements.

We observed increasing and decreasing trend in the maximum surface free energy with increasing coating speed. As hypothesized, for film deposition, $G_{max,f}$ increased from 4.6 μJ/m to 6.0 μJ/m when the coating speed increased from 0.5 mm/s to 0.9 mm/s, due to increased arc length and drag length as a function of speed. At the transition speed 0.9 mm/s, the close match between $G_{max,f}$ of 6.0 μJ/m and $G_{max,w}$ of 5.8 μJ/m is consistent with our hypothesis that the max surface free energies for film and stripe regimes cross over at the critical coating speed. In the stripe deposition regime, $G_{max,w}$ first decreased from 5.8 μJ/m to 5.0 μJ/m from 0.9 mm/s to 1.5 mm/s, following the proposed trend of decreasing $G_{max,w}$ with increasing speed. Both arc length and drag length decreased from 0.9 mm/s to 1.5 mm/s as a result of the decreasing amount of deposition and the increasing deposition frequency. However, $G_{max,w}$ did not further decrease at 2 mm/s and instead moderately increased, possibly due to the instability of stripe deposition on non-wetting substrates as evidenced by no stripe deposition at coating speed > 3mm/s. The difference between G_{max} and G_{min} for both film and stripe deposition come from the exposed deposit/substrate to air after meniscus slipping. The wider stripe pitch with exposed substrate in stripe deposition resulted in larger difference between G_{max} and G_{min} compared to film deposition. The change of G_{max} and the occurrence of film-to-stripe transition reflects the interplay between pinning and depinning forces at the meniscus front, as a function of coating speed. As the coating speed increases, the film thickness decreases in the evaporation regime due to mass balance.[35] At the same time, viscous drag force increases, which leads to extended meniscus length with lower dynamic contact angle. The decrease in film thickness causes the decrease in the pinning force, while the lower dynamic contact angle causes the increase in the depinning force. At a critical coating speed, pinning from thin film cannot balance with depinning of the meniscus, and thus the meniscus transits from film deposition into stripe deposition. After transition, given the partial wetting of solution on the substrate no longer covered by the film, both the arc length and the drag length decrease as to lower G_{max}. Therefore we observed an apparent maximum system surface free energy at the film-to-stripe transition, which was caused by the maximum pinning/depinning existed at this transition. The film-to-stripe transition occurred to minimize the system surface free energy in order to avoid the appearance of the hypothetical film and stripe regimes with high system surface free energy as shown in **Figure 3.5a**. In general, the analysis on surface free energy validated the hypothesis on the relationship between the minimization of surface free energy and the appearance of film to stripe morphology transition.

3.3 Conclusion

In conclusion, we demonstrated the film-to-stripe morphology transition induced by meniscus stick-and-slip instability for multiple polymer systems and systematically investigated solution coated DPP2T-TT. With increasing coating speed, morphology transition from undulated film to regularly spaced stripes was observed. The coexisting film and stripes deposited at the critical coating speed showed similar π-π stacking and degree of alignment with 3.1 anisotropy from GIWAXS. However, FET device measurement showed 3 times higher charge transport mobility in stripes compared to that in films coated at the same condition. To further understand and study morphology transition from meniscus instability, a generalizable surface free energy model was proposed for the meniscus guided coating setup. In this model, three changing interfaces, namely the meniscus free interface, the solvent-substrate interface and the solvent-deposit interface were quantitatively studied to obtain the maximum surface free energy G_{max} during a stick-and-slip cycle. We hypothesize that film-to-stripe morphology transition occurs to lower G_{max}. Through high speed imaging and analysis, we observed that the maximum surface free energies for film and stripe deposition $G_{max,f}$ and $G_{max,w}$ closely match at the critical coating speed; lower than the critical speed, G_{max} continuously increased while higher than the critical speed, G_{max} initially dropped as hypothesized. The increasing and decreasing trend of $\mathrm{G_{max}}$ reflects the interplay between pinning and depinning forces that underlies the film-and-stripe morphology transition. We believe that our surface free energy model provides a quantitative approach for studying meniscus instability with morphology transition under the unidirectional coating framework. We note that processing parameters are connected to the meniscus-instability-driven morphology transition through the system surface free energy model. By varying solution coating parameters, system surface free energy G_{max} can be tuned as to alter the critical transition speed of the film-to-stripe transition and tune the morphology of the deposited patterns. This work lays the foundation for further investigations on predictive models for controlling meniscus instability during solution coating for lithography-free patterned deposition.

3.4 Experimental Section

Sample preparation. The conjugated polymer DPP2T-TT (Mn = 20,000 g/mol, Mw = 104,000 g/mol, PDI = 5.2) was synthesized following a previously published procedure and was used as received.[99] Octyldecyltrichlorosilane (ODTS) treated 300 nm SiO_2 on Si wafer was prepared as dewetting substrates with low trap densities. ODTS-treated substrates were specifically chosen to enable partial wetting and thus morphology transition. A 4' silicon wafer with 300 nm thermally grown SiO_2 layer was treated in oxygen plasma at 30 W power for 10 min (Harrick Plasma PDC-001). The substrate was immersed in 0.2 v% solution of octyldecyltrichlorosilane (Acros, 99.5%) in anhydrous trichloroethylene (Sigma, 99%) for 20 min. The substrate was removed from solution and baked at 120 °C in air for 20 min for ODTS crystallization. Polymer DPP2T-TT was dissolved in chloroform (Macron, ACS grade) at 5 mg/ml and stirred for 2 hours to ensure dissolution. DPP2T-TT was deposited onto ODTS-treated SiO2 substrates by a meniscus-guided coating method using an ODTS-treated SiO2 blade.[31, 73] Various coating speeds were used for deposition to induce film to stripe morphology transition. The substrate temperature was fixed at 25 °C.

Atomic force microscopy and scanning electron microscopy: AFM measurements were performed on the Asylum Cipher AFM with Tap300Al-G tapping mode AFM tips. Scan area was set to 30 x 30 μm^2 to obtain mesoscale morphology of the films and stripes coated from different speed. Film thickness, dimension of undulation on films and dimension of stripes were obtained from AFM measurements for calculation of surface free energy. Pitch of film undulations was obtained from AFM measurements and stripe pitch was obtained from microscopy for frequency calculation of the appearance of film undulation and stripes. Cross-sectional image of the stick-and-slip films and stripes were characterized using scanning electron microscope (SEM, Hitachi S-4800) with acceleration voltage of 15 kV. Before measurements, the samples were cut in the center along the coating direction to expose the cross-section of films and stripes. A thin layer of Au-Pt with a thickness of several nanometers was deposited at the cross-section.

Grazing incidence wide angle X-ray scattering. GIWAXS measurements were performed at beamline 8-ID-E of Advanced Photon Source at the Argonne National Laboratory.[103] Data were collected with an incident beam energy at 10.86 keV on a two-dimensional detector (Pilatus 1M) at two different positions and the images were combined to eliminate most of the inactive pixels using the GIXSGUI package written for Matlab.[49] GIXSGUI was also used to apply corrections for detector nonuniformity, beam polarization, and detector sensitivity, and to reshape the 2-dimensional data into the representation q_z vs q_r (= $\sqrt{q_x^2 + q_y^2}$). Experiments were carried in helium environment to reduce background scattering. The incident angle was set at 0.14 degree (above the critical angle of DPP2T-TT) for measurements. Information of the edge-on π-π stacking peak was obtained by performing a 5^0 sector cut near the image horizon with $-88^0<\chi<-83^0$ on the data images. Peak deconvolution was performed to separate the (010) π-π stacking peak from the amorphous peak, the background scattering and the peak from crystalline ODTS. The π-π stacking peak was fitted with a Gaussian function to obtain the peak position, peak area and the full width half maximum (FWHM). Similarly, a 5^0 sector cut with $-10^0<\chi<-5^0$ vertically on the images was performed to obtained peak information of the edge-on lamellar stacking peaks. Peak deconvolution and peak fitting with Gaussian function was performed for the (200) lamellar stacking peak and higher order peak.

Device fabrication and characterizations. Bottom gate top contact configuration was used to measure charge transport at the DPP2T-TT thin films and stripes. Gold source-drain electrodes with a thickness of 35 nm were evaporated on top of the DPP2T-TT deposit coated from chloroform solution. The channel length and width for thin films were 70 μm and 4500 μm respectively. For stripes, the channel length was 70 μm and the channel width was corrected by the stripe width. Keysight B1500A analyzer was used for all as-deposited FET devices measurements in a glove box under nitrogen environment. Gate bias between 0 to -100 V with drain voltage of -100 V was applied. The apparent mobility in the saturation regime was calculated using the equation $\mu_{sat} = \frac{2L}{WC_i}\left(\frac{d\sqrt{I_{SD}}}{dV_G}\right)^2$. The capacitance for the 300 nm SiO_2 layer was estimated with $C = \frac{\varepsilon\varepsilon_0}{d_0}$ where ε is the relative permittivity of the insulator (3.9 for SiO_2), ε_0 is the air permittivity and d_0 is the thickness. With consideration of the influence of the ODTS layer,[104] the capacitance of SiO_2 used for calculation is 11 nF/cm^2. For stripe charge transport mobility, correction of the channel width was performed by multiplying number of stripes in the channels with the stripe width. Number of stripes was obtained by dividing the total channel width (7500 μm) by the stripe pitch (Figure C9).

High speed video recording and analysis. Printing videos were recorded by Phantom v9.1 with 1000 frame per second recording rate and 1632 x 1200 pixels resolution. The videos were processed with Phantom CV 2.8 to obtain individual frames for further image analysis. The images were analyzed with MATLAB using modified code containing the circle fitting code by Izhak Bucher.[128] On each image frame, the meniscus was fitted with a circle where the arc length of the meniscus on the circle and the drag length of the meniscus as a projected length of the arc on the substrate horizon were extracted. The arc length and the drag length of the meniscus were used in the surface free energy calculation.

Interfacial free energy evaluation. Interfacial free energies of the ODTS-modified silicon wafer and DPP2T-TT thin films were estimated by contact angle measurements of known probing liquids and least square method analysis using equation of state proposed by Kwok and coworkers,[127] with the Young's equation as described in detail in our previous work.[47] Contact angle measurements were performed with Rame-Hart Standard Goniometer by recording the contact angle of liquid on substrates in the sessile drop geometry. Contact angle measurements were performed on substrates with unknown surface energies by using probing liquids of various molecular structures, intermolecular forces and surface energies. Based on the equation $cos\theta = -1 + 2\sqrt{\frac{\gamma_{SV}}{\gamma_{LV}}}[1 - \beta(\gamma_{LV} - \gamma_{SV})^2]$ with known contact angle $cos\theta$ and known probing liquid interfacial free energy γ_{LV},[127] the unknown γ_{SV} of the substrate and the fitting parameter β were obtained by least square analysis. All surfaces were determined to be chemically inert to employed probing liquids, atomically smooth and chemically homogenous based on AFM measurements. Interfacial free energies of chloroform and 5 mg/ml DPP2T-TT in chloroform was measured by pendant drop measurements. Because the shape of the pendant drops was only dependent on gravitational force and interfacial free energy of the liquid γ_{LV}, γ_{LV} can be obtained utilizing Young-Laplace equation $\Delta P = \gamma_{LV}(\frac{1}{R_1} + \frac{1}{R_2})$ as proposed by Stauffer.[129] During pendant drop measurements, DROPimage Advance software recorded the shape of the pendent drops and calculated surface tension of the liquid, which were chloroform and DPP2T-TT solution for this study. Interfacial free energies of the ODTS – DPP2T-TT interface, ODTS – solution interface and DPP2T-TT – solution interface were calculated using the equation $\gamma_{AB} = \gamma_A + \gamma_B - 2\sqrt{\gamma_A\gamma_B}[1 - \beta(\gamma_A - \gamma_B)^2]$, with known γ and β from above measurements.[127]

Equations 3.1-3.4 are based on two assumptions. The 1st assumption is instant slipping, where the slipping time of the meniscus is considered negligible. Therefore, the blade and the contact line pinned at the blade are assumed stationary, simplifying comparison of the drag length d at G_{max} and G_{min}. The 2nd assumption is that one undulation/stripe is fully formed before slipping. This assumption is based on the symmetric-shaped undulation and stripes from atomic force microscopy (AFM) and scanning electron microscopy (SEM) shown in **Figure C6**. The meniscus is assumed to be pinned at the apex of the undulation/stripe because the maximum pinning force occurs at this point with a maximum contact area between the meniscus and the deposit in the direction of contact line movement. In order to form symmetric-shaped deposit, polymer deposition is expected to start behind the meniscus near the contact line during pinning. With the two major assumptions, the system surface free energy model describing the front meniscus slipping during meniscus-guided coating is used in the energy calculation in the following sections.

Chapter 4

Generalized Morphology Transition in Solution Coated Conjugated Polymer Systems[4]

4.1 Introduction

In this work, we utilize meniscus guided solution coating to deposit conjugated polymer DPP-TT with various coating conditions. We perform speed-series solution coating of DPP-TT on a series of five substrates with substrates surface free energy from 14.1 mN/m to 54 mN/m. Film-to-stripe morphology transition is observed on low surface energy substrates and film texture variation caused by evaporation to Landau-Levich coating regime transition is observed on medium to high surface energy substrates. We construct the dimensionless group named as morphology number to describe the film-to-stripe morphology transition with various coating conditions. The morphology number is a product of evaporative Peclet number and the modified capillary number, which includes the important parameters that directly relates to film-to-stripe transition. We perform a series or characterizations to calculate the morphology number, including AFM measurements for deposit dimension to calculate evaporation rate, microfluidic capillary measurements for solution viscosity, pendant drop measurements for solution surface energy and receding contact angle measurements. We observe a sudden decrease in the value of morphology number when film to strip morphology transition occurs. The sudden decrease of morphology number can come from the change of evaporation rate when film-to-stripe transition occurs in a coating speed series, or from the change in solvent viscosity, surface energy or he receding contact

---

[4] The contents of this chapter appear in Qu, G.; Brown, M.M.; Diao, Y. "Generalized Morphology Transition For Evaporative Assembly of Conjugated Polymers Via Solution Coating" Submitted to ACS Mater. Letters

angle when varying other parameters. The generality of the morphology number is validated by solution coating of DPP-TT from a different solvent at a different substrate temperature and solution coating of two other conjugated polymers DPP-BTz and PII-2T.

4.2 Results

We deposited conjugated polymers DPP-TT, DPP-BTz and PII-2T onto various substrates to study the morphology transition behavior of conjugated polymers via meniscus guided coating (**Figure 4.1a-d**).[30, 36, 47] DPP-TT is used as our model polymer and is solution deposited on selected substrates across a range of substrate surface energy varying from 14.1 mN/m to 54.7 mN/m, including heptadecafluorodecyltrimethoxysilane (HTMS) treated substrate, octadecyltrichlorosilane (OTS) treated substrate, pentafluorophenylpropyltrichlorosilane (FPTS) treated substrate, poly(vinyl alcohol) (PVOH) coated substrate and SiO_2 substrate. We perform solution coating on these substrates with various coating speeds from 0.01 mm/s to 100 mm/s, resulting in different deposit morphology on substrates with various substrate surface energy (**Figure 4.1e, f**). On medium and high surface energy substrates, we obtain film deposition across a wide speed range with the deposition transition from evaporation regime to Landau-Levich regime defined by Le Berre.[35] In this condition, we observe undulated film with wavy film surface at low speed, smooth aligned film at intermediate speed and misoriented smooth film evaporated from a thin liquid layer at high speed (**Figure 4.1e**). On the other hand, on low surface energy substrates, continuous film with mild undulation is deposited at low speed and discrete stripes with regularly spaced gaps in between is deposited at intermediate speed, but dewetting occurs at high speed leaving no deposition on the substrate (**Figure 4.1f**). Discussion on speed dependent morphology transition and quantitative analysis is included in following contents.

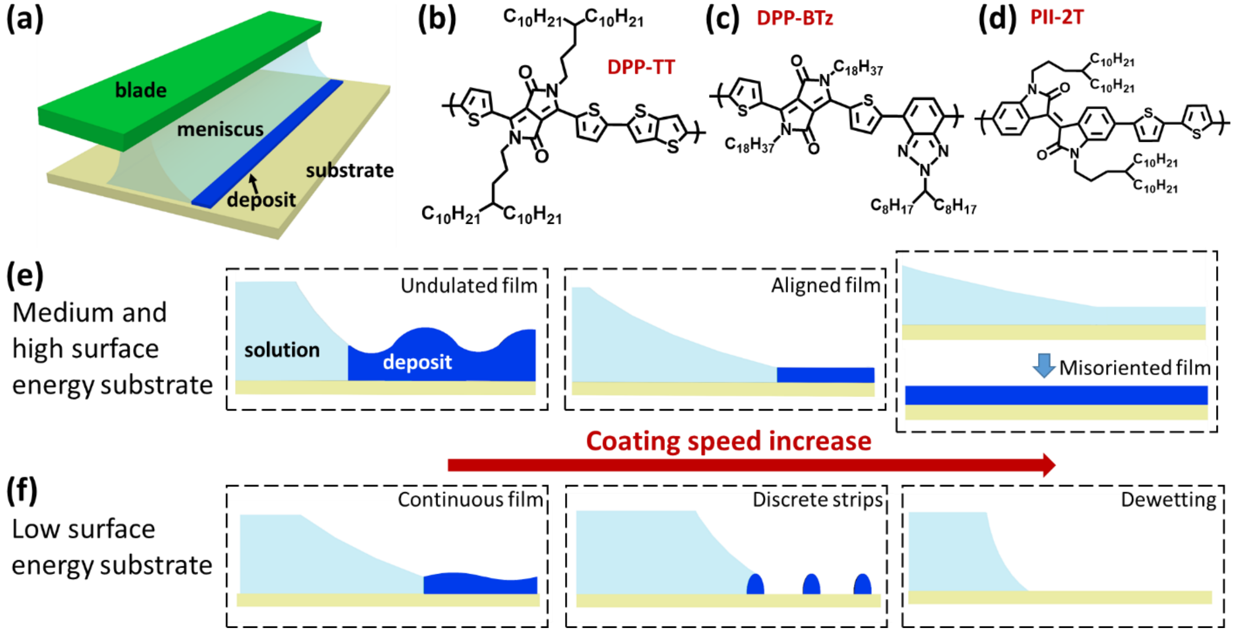

Figure 4.1. Solution coating of conjugated polymers and illustration of morphology transition. (a) Scheme of solution coating with moving blade and stationary substrates. Molecular structure of conjugated polymers (b) DPP-TT, (c) DPP-BTz and (d) PII-2T used in the experiments. Coating speed dependent deposit morphology transition for solution coating on (e) medium and high surface energy substrates and (f) low surface energy substrates.

The deposit morphologies on the five substrates HTMS, OTS, FPTS, PVOH and SiO_2 (molecular structure in **Figure D1**) differentiate based on the substrate surface energy, which is quantified by measuring contact angle of probing liquids and utilizing equation of states with Young's equation, discussed in our previous work.[47] In short, contact angles on the substrate from multiple probing liquids with known surface energy (**Table D1**) are measured and substituted into the equation of states to obtain substrate surface energy from fitting (details in methods). From this approach, we are able to modulate the substrate surface energy from 14.1 mN/m to 54.7 mN/m by performing surface treatments, with surface energy of HTMS to be 14.1 mN/m, OTS to be 20.8 mN/m, FPTS to be 31.1 mN/m, PVOH to be 40.5 mN/m and SiO2 to be 54 mN/m, comparable to literature results.[47, 130]

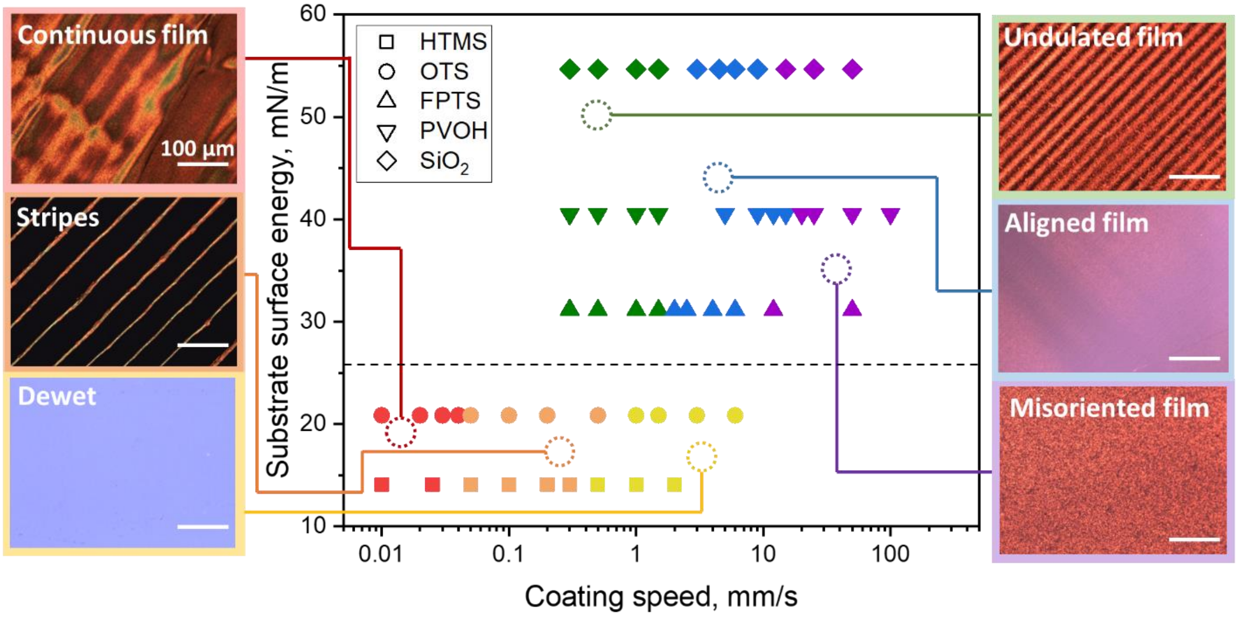

Figure 4.2. Phase diagram of solution coating DPP-TT from 5 mg/ml toluene solution at 70 °C on various substrates with various coating speed. The shape of data points indicates substrates and the color of data points indicates morphology.

As previously stated, the coating speed dependent morphology transition of DPP-TT deposit behaves differently on substrates with various surface free energy, illustrated in the phase diagram **Figure 4.2** with microscopy images. On low surface energy substrates HTMS and OTS, the morphology of DPP-TT changes from undulated continuous film to discrete stripes, and then dewets at increased speed depending on the substrate surface energy. This film to stripe and to dewetting morphology transition is discussed in detail in our previous work,[36] which is governed by the competition between pinning and depinning forces at the contact line of the meniscus. Within one morphology (film or stripe), the pinning force applied by the adhesion between meniscus and deposit is balancing with the depinning force applied by the surface free energy of the stretched meniscus. When the coating speed increases, the deposit dimension (film thickness or stripe size) related to adhesion decreases because of constant evaporation rate and material balance,[35] and thereby the depinning force outcompetes the pinning force, causing morphology transition. For HTMS (γ = 14.1 mN/m), the transition point for film to stripe is between 0.025 –

0.05 mm/s and for stripe to dewetting is 0.3 – 0.5 mm/s, while for OTS ($\gamma = 20.8$ mN/m), transition for film to strip is 0.04 – 0.05 mm/s and for stripe to dewetting is 0.5 – 1 mm/s. The decreased speed range for film to stripe and strip to dewetting morphology transition on HTMS compared to OTS is related to the wetting dependent evaporation rate on substrates with different surface energy. As described by Deegan and based on electric field analogy, the evaporation rate at a meniscus contact line is negatively related to the contact angle of the liquid on the substrate, where high contact angle leads to low evaporation rate and vice versa.[74] Therefore, the low surface energy of HTMS causes higher degree of contact angle and lower evaporation rate, leading to smaller deposit dimension with smaller pining force, and thus lower morphology transition speed range. On the other hand, thin film is coated on the medium to high surface energy substrates FPTS, PVOH and SiO_2 across a wide speed range between 0.2 mm/s and 100 mm/s with variation of the film texture. As discussed by Le Berre, solution coating on a total wetting substrate undergoes evaporation regime at low speed and Landau-Levich regime at high speed.[35] That is, at low coating speed, the solute deposition is driven by solvent evaporation and the contact line of the meniscus moves along with the moving blade or substrate, resulting in film thickness inversely proportional to coating speed in the evaporation regime. In Landau-Levich regime with high coating speed, the viscous force in the solution dominates and drags out a liquid film on the substrate followed by evaporation, causing the film thickness to increase with coating speed. The observed speed-dependent film texture changing from undulated film, aligned film to misoriented film is related to the coating regime transition on medium to high surface energy substrate. At low coating speed in evaporation regime, the stick-and-slip instability appears at the moving meniscus during evaporation driven deposition and produces undulated thin film with wavy surface. As the coating speed increase, the viscous force starts to play a role and deforms the meniscus from its equilibrium shape,[30] leading to smooth aligned film. In the Landau-Levich regime with high coating speed, the film is smooth but contains misoriented crystallites because crystallization occurs from a thin liquid layer dragged out by the fast-moving meniscus. The film texture transition speed range on FPTS, PVOH and SiO2 substrates are similar that undulated film to aligned film transition occurs above 1.5 mm/s on all substrates, and the aligned film to misoriented film transition occurs between 6 – 12 mm/s, 15 – 20 mm/s and 9 – 15 mm/s on FPTS, PVOH and SiO_2 respectively. The similar transition speed range on these substrates is observed because of the low contact angles of the solution on the substrates, resulting in similar evaporation rate. In general, we observe coating speed dependent morphology transition of solution coating of DPP-TT on a series of substrates, where the morphology transition is related to multiple parameters involved in solution coating.

We further investigate the role of the previously discussed coating parameters that influence the important film-to-stripe morphology transition and construct a combined dimensionless number to describe this transition with eliminating the coating speed effect. We first consider the evaporation rate related dimensionless number and find Peclet number as a good candidate. Peclet number describes the competition between two different means of transport, commonly used for comparing heat transfer versus convective mass transport or diffusive versus convective mass transport. In our coating condition, there is evaporative mass transport of the solvent and convective mass transport from coating speed applied by the blade. Therefore we can incorporate evaporation rate Q_{ev} into the Peclet number,[131] and together with coating speed v we are able to utilize the evaporative Peclet number to describe the behavior of coating. In this case, the evaporative Peclet number is defined as $Pe = \frac{\ddot{Q}_{ev}}{v}$, where Q_{ev} is the reduced evaporation rate or we called evaporation velocity, and v is the coating speed. Detailed discussion on the calculation and derivation of $\ddot{Q}_{ev}$ is included in the methods section. In short, we calculate the evaporation rate of the solvent Q_{ev} in volume per time from the mass balance equation by Le Berre.[35] To reduce Q_{ev} to the same dimension and direction as the coating speed v, we divide Q_{ev} by the width of the substrate and the height of the meniscus to obtain an averaged one-dimensional evaporation rate $\ddot{Q}_{ev}$ in the same direction as v. On the other hand, we determine from the previous experiments that wetting properties, viscous drag forces and meniscus surface energy significantly impact the deposit morphology. Capillary number is an important dimensionless group that compares the viscous drag forces and the surface tension forces, serving as a characteristic parameter in complex liquid coating systems.[35, 106] We modify the capillary number to incorporate wetting properties into its original form to represent our experimental conditions. The modified capillary number is calculated as $Ca^* = \frac{\eta v}{\sigma cos\theta_r}$, where η is the viscosity, v the coating speed, σ the surface energy of the liquid and θ_r the receding contact angle of liquid on the substrate. Both the evaporative Peclet number and the modified capillary number describe the properties at the liquid-air free interface during solution coating, and therefore they can be multiplied into a combined dimensionless number to summarize the morphology transition behavior while eliminating the coating speed effect. We choose to evaluate the product of Peclet number and capillary number instead of these two numbers individually because Peclet number is dependent on coating speed and capillary number does not directly reflect morphology transition. We name the final dimensionless group morphology number with the equation $Mo = \frac{\ddot{Q}_{ev}\eta}{\sigma cos\theta_r}$, which the value correlates with the morphology transition behavior and is coating speed independent.

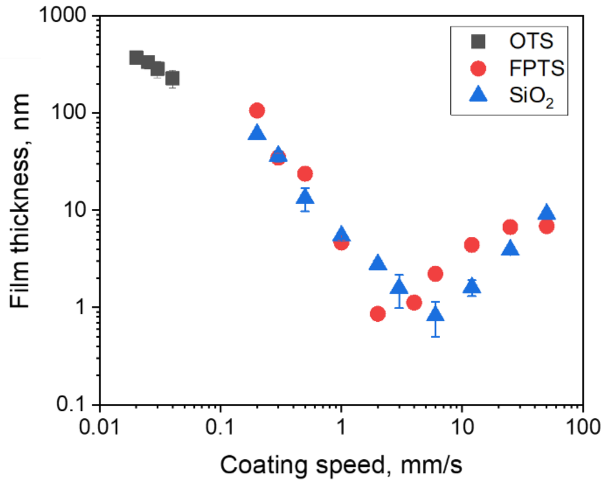

Figure 4.3. Film thickness results from AFM measurements of films on OTS, FPTS and SiO_2 substrates.

We thereby perform a series of measurements to obtain the parameters to quantitatively calculate the morphology number, all detailed in methods sections. Because deposit morphology and transition on HTMS and OTS is similar, and on FPTS, PVOH and SiO_2 is similar, we select OTS, FPTS and SiO_2 as representatives of low, medium and high surface energy substrates for quantitative calculations. To quantify morphology number, the evaporation velocity $\ddot{Q}_{ev}$, solution viscosity η, solution surface energy σ and receding contact angle θ_r are obtained from measurements and calculations. For evaporation velocity $\ddot{Q}_{ev}$, we perform AFM measurements to obtain film thickness and stripe dimensions to evaluate the deposition rate and thus the solvent evaporation rate (**Figure D2a, b**). The film thickness results in shown in **Figure 4.3**, following a similar trend as reported in other works.[30, 35, 132] One thing to note is that due to film-to-stripe morphology transition on OTS, no film is coated above 0.04 mm/s. The decreasing and increasing film thickness on more wetting substrates FPTS and SiO_2 is associated with the change from evaporation regime to Landau-Levich regime as previously discussed. The thinnest film of FPTS occurs at 2 mm/s and on SiO_2 at 5 mm/s because of the lower evaporation with higher receding contact angle on FPTS compared to SiO_2. After obtaining film thickness and stripe dimensions, we calculated $\ddot{Q}_{ev}$ based on mass balance equation for the evaporation regime. Solution viscosity is measured in a capillary viscometer setup, where a droplet of the liquid is added to one end of a capillary and the movement of the meniscus inside the capillary is recorded.[133] Governed by the Hagen-Poiseuille equation, the time-dependent liquid length inside the capillary is related to the viscosity and the power-law exponent of a non-Newtonian liquid. By fitting the results from liquid movement tracking, we are able to obtain the viscosity of 5 mg/ml DPP-TT in toluene at room temperature to be 0.76 mPa·s and is estimated to by 0.55 mPa·s at coating temperature 70 °C based on pure toluene results.[134] The surface free energy of 5 mg/ml DPP-TT is obtained by pendant drop measurements in 70 °C water bath to be 19.3 mN/m. The receding contact angle is measured by sessile drop configuration using pure toluene at room temperature on the three substrates with a microsyringe withdrawing liquid to cause contact line movement (**Figure D2c, d**). The receding contact angles vary from 34.2° on OTS to 8.5° on FPTS and 7.3° on SiO_2, relating to the substrate surface energies. Hence, all the parameters are ready to calculate the morphology number.

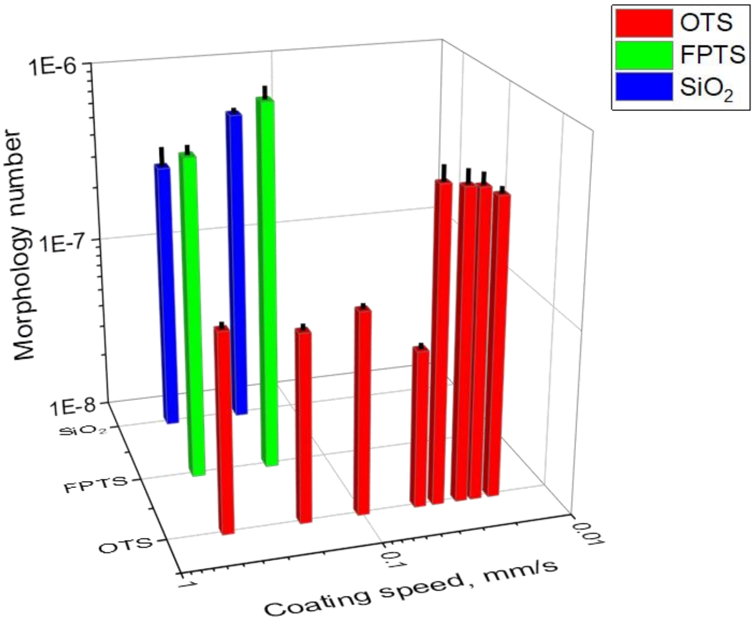

Figure 4.4. Morphology number for coating of 5 mg/ml DPP-TT from toluene at 70 °C on OTS, FPT and SiO_2 substrates.

We construct a 3-dimensional plot of morphology number with respect of coating speed and substrates to observe its correlation with film-to-stripe morphology transition influenced by different parameters (**Figure 4.4**). Because morphology number only applies to evaporation regime, we do not include data points in the Landau-Levich regime for coating on FPTS and SiO_2 substrates. When inspecting the morphology number of the OTS set, one can find that the morphology of film (0.02 – 0.04 mm/s) and for strips (0.05 – 0.5 mm/s) are nearly speed independent and distribute in a narrow range, with Mo = $4.2 – 5.1\times10^{-7}$ for films and Mo = $0.7 – 1.2 \times10^{-7}$ for strips. This agrees with our derivation of morphology number that we multiple evaporative Peclet number with capillary number to eliminate the influence of coating speed. There is a significant decrease in the value of morphology number from film morphology to stripe morphology, both along the coating speed axis and the substrate axis with various substrate surface energy. The morphology number value of films are within the range of 3×10^{-7} to 1×10^{-6}, with the value of morphology number of strips concentrates at 1×10^{-7}, which directly correlates with a large decrease in the evaporation rate during coating condition. Along the coating speed axis for OTS substrates, the drop of morphology number results from the significant increase of contact angle when film-to-stripe transition occurs,[36] and the corresponding decreasing in evaporation rate. Along the substrate axis for 0.2 mm/s and 0.5 mm/s coating speed, the drop of morphology number is contributed by contact angle increase from both substrate surface energy change and the film-to-stripe morphology transition, leading to the decrease in evaporation rate. In general, the morphology number is a parameter that describes and quantifies the phenomenon of film-to-stripe morphology transition for solution coating of conjugated polymers.

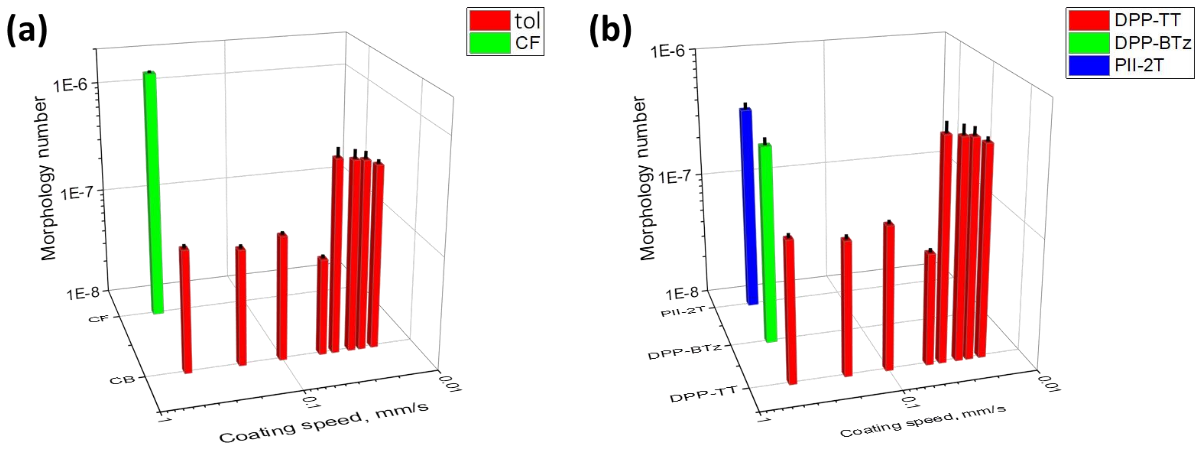

Figure 4.5. Generalization of morphology number. (a) Morphology number of solvent and coating environment series with solution coating of 5 mg/ml DPP-TT in toluene at 70 °C and in chloroform at 25 °C. (b) Morphology of polymer series with solution coating of 5 mg/ml DPP-TT, DPP-BTz and PII-2T in toluene at 70 °C.

We perform solution coating with other conditions to validate the generality of the morphology number. We first deposit 5 mg/ml DPP-TT solution from chloroform on OTS substrates at room temperature 25 °C and compare with DPP-TT deposited from toluene at 70 °C. The viscosity and surface tension of 5 mg/ml DPP-TT chloroform solution as well as the receding contact angle of chloroform is measured with the same method of toluene, and the results are η = 0.63 mPa·s, σ =

25.4 mN/m and θ_r = 31°. From **Figure 4.5a**, we observe that at 0.5 mm/s, DPP-TT deposition is film from chloroform but is stripe from toluene. There is a significant decrease in morphology number with Mo = 1.6×10^{-6} for chloroform and Mo = 1.2×10^{-7} for toluene. The larger viscosity of chloroform solution at room temperature increases the viscous drag and delays morphology transition, as well as contributes to the larger morphology number. Meanwhile the lower receding contact angle leads to higher evaporation rate and also shifts the morphology transition, resulting in a large value of morphology number. On the other hand, we deposit 5 mg/ml DPP-BTz in toluene and 5 mg/ml PII-2T in toluene solutions on OTS substrates at 70 °C and compare with DPP-TT deposition (**Figure 4.5b)**. Interestingly both DPP-BTz and PII-2T shows film morphology at 0.5 mm/s, in contrast of the DPP-TT strips at 0.5 mm/s. The morphology number is 3.3×10^{-7} for PII-2T, 3.9×10^{-7} for DPP-BTz, and 1.2×10^{-7} for DPP-TT. Because of the relative flexible configuration of DPP-BTz and PII-2T,[30] the solution state polymer morphology and the ability of forming liquid-crystalline mesophase may causes change in solution surface energy and viscosity, thereby shifting the morphology transition and changing the morphology number. From the multiple solution coating systems and conditions, we are able to demonstrate the generality of morphology number which describes film-to-stripe morphology transition involving multiple parameters involved in solution coating.

4.3 Conclusion

In summary, we deposit conjugated polymer DPP-TT on substrates using meniscus guided solution coating with various coating conditions to study the meniscus instability driven morphology transition. On a series of five substrates with substrate surface free energy ranging from 14.1 mN/m to 54 mN/m, the morphology of DPP-TT on low surface energy substrates HTMS and OTS undergoes film to stripe and to dewetting transition, while on medium to high surface energy substrates FPTS, PVOH and SiO_2 undergoes evaporation to Landau-Levich coating regime transition. We determine the important parameters involving in solution coating deposit morphology transition to be evaporation rate, wetting properties, viscous drag forces and interfacial forces. To utilize these parameters in a generalized and quantitative way that can describe the morphology transition of solution coated conjugated polymers, we construct the morphology number Mo, a product of evaporative Peclet number and modified capillary number. We performed a series of measurements to calculate the morphology number for our experimental conditions, including AFM measurements for deposit dimension, capillary viscosity measurements, pendant drop measurements for solution surface energy and receding contact angle measurements. We validate that the morphology number is coating speed independent, as multiplying evaporative Peclet number with modified capillary number cancels the velocity term in the parameter. We observe significant decrease in the value of morphology number when film to strip morphology occurs, regardless of what coating condition is varied. In a coating speed series, the film-to-stripe morphology transition is associated with a drastic decrease in evaporation rate, reflected in the decrease of morphology number. When varying other parameters at the same coating speed, the change in solvent viscosity, surface energy and the receding contact angle will contribute to the value of morphology number. With discussion and validation of the generality of the morphology number, we demonstrate the capability of using a parameter to describe the film-to-stripe morphology transition for various solution coating conditions. Studies that connects the underlying physical fundamentals in terms of dimensionless group to industry relevant solution coating instabilities can help understand and control of solution coating conditions to achieve desired morphology.

4.4 Experimental Section

Substrate treatment. Substrate modification is performed to vary the substrate surface energy. Heptadecafluorodecyltrimethoxysilane (HTMS) treatment is performed by exposing silicon wafer to 1 ml of 5 vol% HTMS in toluene solution. The HTMS solution is placed in a 50 ml beaker together with silicon wafer in a sealed glass container. The deposition is carried in an atmospheric pressure oven at 80 °C for 3 h and cooled to room temperature inside the oven. Octadecyltrichlorosilane (OTS) treatment is performed by reacting a plasma treated silicon wafer with 50 ml of 0.2 vol% OTS in trichloroethylene solution in a glass petri dish. The wafer is then rinsed with toluene-acetone-isopropanol solvent series and baked on a hotplate at 120 ºC for 20 minutes. Pentafluorophenylpropyltrichlorosilane (FPTS) treatment is performed by vapor deposition on plasma treated silicon substrates. Silicon substrate pieces are placed in a glass petri dish near the edges with a droplet (~ 1 µL) of FPTS at the center of the petri dish, heated in an atmospheric pressure oven at 75 °C for 1 h. Poly(vinyl alcohol) (PVOH) substrate is prepared by solution coating of 10 wt% PVOH in aqueous solution on silicon substrates at 10 mm/s with a substrate temperature at 60 °C to obtain smooth film.

Solution coating of conjugated polymers. The polymer used in the manuscript DPP-TT (Mn = 16,000 g/mol, Mw = 108,800 g/mol, PDI = 6.8), DPP-BTz (Mn = 176,600 g/mol, Mw = 463,000 g/mol, PDI = 2.6), and PII-2T (Mn = 156,000 g/mol, Mw = 421,700 g/mol, PDI = 2.7) are synthesized as previously reported and used as received.[48, 99, 135] The polymer solutions for coating are prepared by dissolving the conjugated polymer at 5 mg/ml in toluene or chloroform and stirred at room temperature until homogeneous solutions are formed. Meniscus guided solution coating of the conjugated polymers is performed in a setup with a stationary OTS treated SiO_2 blade and a fixed substrate.[31] The blade is attached to a horizontal translational motor with a tilt angle of 8º and a gap size of 100 μm above the substrate. Polymer solution is added between the blade and the substrate, and the movement of the blade drives evaporative assembly of the polymer. The substrate temperature is set at 70 °C for solution coating from toluene and at 25 °C for coating from chloroform.

Substrate surface energy measurements. Surface free energies of HTMS, OTS, FPTS, PVOH and SiO_2 substrates are evaluated by measuring contact angles of probing liquids with known surface free energy. Results are analyzed using equation of state combined with Young's equations, described in detail in our previous work.[47] Contact angle measurements are performed on Rame-Hart Standard Goniometer with sessile drop geometry of probing liquid droplets on the testing substrates. From the equation $cos\theta = -1 + 2\sqrt{\frac{\gamma_{SV}}{\gamma_{LV}}}[1 - \beta(\gamma_{LV} - \gamma_{SV})^2]$ with known contact angle $cos\theta$ and probing liquid surface free energy γ_{LV},[127] the unknown substrate surface free energy γ_{SV} and the fitting parameter β are obtained by least square analysis.

Evaporative Peclet number calculation. Evaporative Peclet number is defined by the competition between evaporative and convective mass transport $Pe_{evap} = \frac{\ddot{Q}_{ev}}{v}$, where $\ddot{Q}_{ev}$ is the evaporation velocity and v is the coating speed applied by blade/substrate movement. Evaporation velocity calculation is based on the mass balance of solvent and solute in the evaporation regime thin film deposition proposed by Le Berre with equation $Q_{ev,f} = \frac{\rho}{C} hLv$, where Q_{ev} is the volumetric evaporation rate, ρ is the polymer density, C is the solution concentration, h is the film thickness, L is the substrate width and v is the coating speed.[35] The mass balance equation can be interpreted as: *solvent volumetric evaporation rate* = $\frac{\rho}{C}$ × *solute volumetric deposition rate*. Same principle applies to stripe deposition with the assumption that stripe deposition belongs to the evaporation regime, where solute deposition occurs concurrently with the meniscus movement and the evaporation of solvent. Therefore, the evaporation rate for strip deposition is $Q_{ev,s} = \frac{\rho}{C}\frac{ALv}{d}$, where *A* is the cross-section area of the stripe and *d* is the gap size between stripes, with other parameters the same as film deposition. In order to reduce the dimension of volumetric evaporation rate to the same dimension as velocity, the evaporation rate is divided by the substrate width *L* and the meniscus height *m* (gap size between blade and substrate) $\ddot{Q}_{ev} = \frac{Q_{ev}}{mL}$. Hence, the reduced evaporation rate has the same direction and dimension as the coating speed and can be compared in terms of evaporative Peclet number. The equations of evaporation velocity for film and stripe deposition are $\ddot{Q}_{ev,f} = \frac{\rho}{C}\frac{hv}{m}$ and $\ddot{Q}_{ev,s} = \frac{\rho}{C}\frac{Av}{md}$, respectively. The film thickness *h*, the strip cross section *A* and the stripe gap size *d* is measured by atomic force microscopy (AFM). AFM measurements are performed on the Asylum MFP-3D AFM with Tap300Al-G tapping mode AFM tips and a scan area of 90 x 90 μm^2. After obtaining *h*, *A* and *d*, the known parameters including the approximated polymer density $\rho = 1.15$ g/cm^3, solution concentration $C = 5$ mg/ml, meniscus height $m = 100$ μm and the various coating speed *v* are substituted into the equation to calculate the evaporation velocity.

Viscosity measurement. Viscosity of polymer solution is measured in a capillary microfluidic viscometer setup following the method introduced by Srivastava and Burns with the governing equations $\eta = \frac{d^2}{S}\frac{1}{(\frac{2}{3}+\frac{1}{3n})}\frac{\Delta P}{vL}$ derived from Hagen-Poiseuille equation,[133] where η is the viscosity, *d* the depth of the channel, *S* the geometric constant for the channel cross section, *ΔP* the capillary pressure inside the channel, *v* the velocity of the liquid and *L* the length of liquid in the channel. The capillary pressure is estimated by $\Delta P = P_{cap} = 2\sigma cos\theta(\frac{1}{d} + \frac{1}{w})$, where σ is the surface tension of the liquid, θ the contact angle of liquid in the channel and *w* the width of the channel. For a non-Newtonian liquid with power law exponent *n*, the Hagen-Poiseuille question can be rearranged into $\frac{1}{L(t)} = C \cdot v(t)^n$ and then $L(t) = \left(\frac{at-b}{k}\right)^k$ with $n = \frac{k}{1-k}$, where a, b and k are fitted parameters and L and t are measured. The experiment is carried in a quartz capillary with d = 1 μm and w = 10 μm. Liquid is dropped from one end of the capillary and the movement of liquid inside the capillary is captured by camera. Therefore, instantaneous $L(t)$ and t are obtained for fitting to get a, b and k to calculate the power law exponent n and viscosity η. For capillary pressure ΔP calculation, the room temperature surface tension of solvent (σ_{tol} = 27.7 mN/m and σ_{CF} = 26 mN/m) and the contact angle of solvent inside the capillary (θ_{tol} = 23.2° and θ_{CF} = 25°) are substituted into the equation. The geometric parameter S = 13.33 is determined from the Hagen-Poiseuille equation for laminar flow through rectangular channel and verified by calibration measurements with water.

Modified capillary number calculation. Modified capillary number is calculated by $Ca^* = \frac{\eta v}{\sigma cos\theta_r}$, where η is the viscosity, v the coating speed, σ the surface energy of liquid (versus gas phase), θ_r the receding contact angle of liquid on substrate. The liquid surface energies of toluene, chloroform and their 5 mg/ml DPP2T-TT solution is measured by pendant drop measurements. For pendant drop measurements, the surface energy of liquid is obtained from Young-Laplace equation $\Delta P = \gamma_{LV}(\frac{1}{R_1} + \frac{1}{R_2})$ as discussed by Stauffer.[129] The pendant drop measurements are taken with DROPimage Advance that the shape of the pendant drop is recorded and the corresponding surface energy is calculated. The surface energy of chloroform and DPP2T-TT in chloroform solution are measured at room temperature in air, while the surface energy of toluene and DPP2T-TT in toluene are measured in 70 °C water bath to approach coating condition. Receding contact angle θ_r measurements for toluene and chloroform at room temperature are performed with Rame-Hart Standard Goniometer while withdrawing liquid from the droplet using a microsyringe.

References

1. Diao, Y.; Shaw, L.; Bao, Z.; Mannsfeld, S. C. B., Morphology Control Strategies for Solution-Processed Organic Semiconductor Thin Films. *Energy Environ. Sci.* **2014,** *7*, 2145-2159.

2. Bijal, B. P.; Ying, D., Multiscale Assembly of Solution-Processed Organic Electronics: The Critical Roles of Confinement, Fluid Flow, and Interfaces. *Nanotechnology* **2018,** *29*, 044004.

3. Duhm, S.; Heimel, G.; Salzmann, I.; Glowatzki, H.; Johnson, R. L.; Vollmer, A.; Rabe, J. P.; Koch, N., Orientation-Dependent Ionization Energies and Interface Dipoles in Ordered Molecular Assemblies. *Nat. Mater.* **2008,** *7*, 326-332.

4. Chen, W.; Huang, H.; Chen, S.; Huang, Y. L.; Gao, X. Y.; Wee, A. T. S., Molecular Orientation-Dependent Ionization Potential of Organic Thin Films. *Chem. Mater.* **2008,** *20*, 7017-7021.

5. Verlaak, S.; Beljonne, D.; Cheyns, D.; Rolin, C.; Linares, M.; Castet, F.; Cornil, J.; Heremans, P., Electronic Structure and Geminate Pair Energetics at Organic–Organic Interfaces: The Case of Pentacene/C60 Heterojunctions. *Adv. Funct. Mater.* **2009,** *19*, 3809-3814.

6. Xue, G.; Zhao, X.; Qu, G.; Xu, T.; Gumyusenge, A.; Zhang, Z.; Zhao, Y.; Diao, Y.; Li, H.; Mei, J., Symmetry Breaking in Side Chains Leading to Mixed Orientations and Improved Charge Transport in Isoindigo-Alt-Bithiophene Based Polymer Thin Films. *ACS Appl. Mater. Interfaces* **2017,** *9*, 25426-25433.

7. Liu, X.; He, B.; Garzón-Ruiz, A.; Navarro, A.; Chen, T. L.; Kolaczkowski, M. A.; Feng, S.; Zhang, L.; Anderson, C. A.; Chen, J.; Liu, Y., Unraveling the Main Chain and Side Chain Effects on Thin Film Morphology and Charge Transport in Quinoidal Conjugated Polymers. *Adv. Funct. Mater.* **2018,** *28*, 1801874.

8. Bai, X.; Zong, K.; Ly, J.; Mehta, J. S.; Hand, M.; Molnar, K.; Lee, S.; Kahr, B.; Mativetsky, J. M.; Briseno, A.; Lee, S. S., Orientation Control of Solution-Processed Organic Semiconductor Crystals to Improve out-of-Plane Charge Mobility. *Chem. Mater.* **2017,** *29*, 7571-7578.

9. Oosterbaan, W. D.; Bolsée, J.-C.; Gadisa, A.; Vrindts, V.; Bertho, S.; D'Haen, J.; Cleij, T. J.; Lutsen, L.; McNeill, C. R.; Thomsen, L.; Manca, J. V.; Vanderzande, D., Alkyl-Chain-Length-Independent Hole Mobility Via Morphological Control with Poly(3-Alkylthiophene) Nanofibers. *Adv. Funct. Mater.* **2010,** *20*, 792-802.

10. Wu, K.-Y.; Hsieh, C.-T.; Wang, L.-H.; Hsu, C.-H.; Chang, S.-T.; Lan, S.-T.; Huang, Y.-F.; Chen, Y.-M.; Wang, C.-L., Influences of out-of-Plane Lattice Alignment on the Ofet Performance of Tips-Pen Crystal Arrays. *Cryst. Growth Des.* **2016,** *16*, 6160-6166.

11. Li, M.; An, C.; Marszalek, T.; Baumgarten, M.; Yan, H.; Mullen, K.; Pisula, W., Controlling the Surface Organization of Conjugated Donor-Acceptor Polymers by Their Aggregation in Solution. *Adv. Mater.* **2016,** *28*, 9430-9438.

12. Shen, Z.; Zhu, K.; O'Carroll, D. M., Aperiodic Porous Metasurface-Mediated Organic Semiconductor Fluorescence. *ACS Photonics* **2018,** *5*, 1215-1227.

13. Chae, S.; Cho, K. H.; Won, S.; Yi, A.; Choi, J.; Lee, H. H.; Kim, J.-H.; Kim, H. J., Favorable Face-on Orientation of a Conjugated Polymer on Roll-to-Roll-Transferred Graphene Interface. *Advanced Materials Interfaces* **2017,** *4*, 1701099.

14. Hiszpanski, A. M.; Lee, S. S.; Wang, H.; Woll, A. R.; Nuckolls, C.; Loo, Y. L., Post-Deposition Processing Methods to Induce Preferential Orientation in Contorted Hexabenzocoronene Thin Films. *ACS Nano* **2013,** *7*, 294-300.

15. Smith, K. A.; Lin, Y.-H.; Mok, J. W.; Yager, K. G.; Strzalka, J.; Nie, W.; Mohite, A. D.; Verduzco, R., Molecular Origin of Photovoltaic Performance in Donor-Block-Acceptor All-Conjugated Block Copolymers. *Macromolecules* **2015,** *48*, 8346-8353.

16. Schuettfort, T.; Huettner, S.; Lilliu, S.; Macdonald, J. E.; Thomsen, L.; McNeill, C. R., Surface and Bulk Structural Characterization of a High-Mobility Electron-Transporting Polymer. *Macromolecules* **2011,** *44*, 1530-1539.

17. Chae, S.; Yi, A.; Lee, H. H.; Choi, J.; Kim, H. J., Laser-Induced Orientation Transformation of a Conjugated Polymer Thin Film with Enhanced Vertical Charge Transport. *Journal of Materials Chemistry C* **2018,** *6*, 9374-9382.

18. Pan, G. X.; Chen, F.; Hu, L.; Zhang, K. J.; Dai, J. M.; Zhang, F. P., Effective Controlling of Film Texture and Carrier Transport of a High-Performance Polymeric Semiconductor by Magnetic Alignment. *Adv. Funct. Mater.* **2015,** *25*, 5126-5133.

19. McCulloch, I.; Heeney, M.; Bailey, C.; Genevicius, K.; Macdonald, I.; Shkunov, M.; Sparrowe, D.; Tierney, S.; Wagner, R.; Zhang, W.; Chabinyc, M. L.; Kline, R. J.; McGehee, M. D.; Toney, M. F., Liquid-Crystalline Semiconducting Polymers with High Charge-Carrier Mobility. *Nat. Mater.* **2006,** *5*, 328-333.

20. Lee, M. J.; Gupta, D.; Zhao, N.; Heeney, M.; McCulloch, I.; Sirringhaus, H., Anisotropy of Charge Transport in a Uniaxially Aligned and Chain-Extended, High-Mobility, Conjugated Polymer Semiconductor. *Adv. Funct. Mater.* **2011,** *21*, 932-940.

21. Sirringhaus, H.; Wilson, R. J.; Friend, R. H.; Inbasekaran, M.; Wu, W.; Woo, E. P.; Grell, M.; Bradley, D. D. C., Mobility Enhancement in Conjugated Polymer Field-Effect Transistors through Chain Alignment in a Liquid-Crystalline Phase. *Appl. Phys. Lett.* **2000,** *77*, 406-408.

22. Baklar, M.; Barard, S.; Sparrowe, D.; Wilson, R. M.; McCulloch, I.; Heeney, M.; Kreouzis, T.; Stingelin, N., Bulk Charge Transport in Liquid-Crystalline Polymer Semiconductors Based on Poly(2,5-Bis(3-Alkylthiophen-2-Yl)Thieno[3,2-B]Thiophene). *Polymer Chemistry* **2010,** *1*, 1448.

23. Bridges, C. R.; Ford, M. J.; Popere, B. C.; Bazan, G. C.; Segalman, R. A., Formation and Structure of Lyotropic Liquid Crystalline Mesophases in Donor–Acceptor Semiconducting Polymers. *Macromolecules* **2016,** *49*, 7220-7229.

24. Bridges, C. R.; Ford, M. J.; Bazan, G. C.; Segalman, R. A., Molecular Considerations for Mesophase Interaction and Alignment of Lyotropic Liquid Crystalline Semiconducting Polymers. *ACS Macro Letters* **2017,** *6*, 619-624.

25. Kim, B. G.; Jeong, E. J.; Chung, J. W.; Seo, S.; Koo, B.; Kim, J., A Molecular Design Principle of Lyotropic Liquid-Crystalline Conjugated Polymers with Directed Alignment Capability for Plastic Electronics. *Nat. Mater.* **2013,** *12*, 659-664.

26. Yang, D. S.; Barlog, M.; Park, J.; Chung, K.; Shanker, A.; Sun, J.; Kang, J.; Lee, K.; Al-Hashimi, M.; Kim, J., Alignment of Lyotropic Liquid Crystalline Conjugated Polymers in Floating Films. *ACS omega* **2018,** *3*, 14807-14813.

27. Trefz, D.; Gross, Y. M.; Dingler, C.; Tkachov, R.; Hamidi-Sakr, A.; Kiriy, A.; McNeill, C. R.; Brinkmann, M.; Ludwigs, S., Tuning Orientational Order of Highly Aggregating P(Ndi2od-T2) by Solvent Vapor Annealing and Blade Coating. *Macromolecules* **2019,** *52*, 43-54.

28. Bilger, D. W.; Figueroa, J. A.; Redeker, N. D.; Sarkar, A.; Stefik, M.; Zhang, S., Hydrogen-Bonding-Directed Ordered Assembly of Carboxylated Poly(3-Alkylthiophene)S. *ACS omega* **2017,** *2*, 8526-8535.

29. Zhang, S.; Pfefferle, L. D.; Osuji, C. O., Lyotropic Hexagonal Ordering in Aqueous Media by Conjugated Hairy-Rod Supramolecules. *Macromolecules* **2010,** *43*, 7549-7555.

30. Park, K. S.; Kwok, J. J.; Dilmurat, R.; Qu, G.; Kafle, P.; Luo, X.; Jung, S.-H.; Olivier, Y.; Lee, J.-K.; Mei, J.; Beljonne, D.; Diao, Y., Tuning Conformation, Assembly, and Charge Transport Properties of Conjugated Polymers by Printing Flow. *Science Advances* **2019,** *5*, eaaw7757.

31. Qu, G.; Zhao, X.; Newbloom, G. M.; Zhang, F.; Mohammadi, E.; Strzalka, J. W.; Pozzo, L. D.; Mei, J.; Diao, Y., Understanding Interfacial Alignment in Solution Coated Conjugated Polymer Thin Films. *ACS Appl. Mater. Interfaces* **2017,** *9*, 27863-27874.

32. Schott, S.; Gann, E.; Thomsen, L.; Jung, S. H.; Lee, J. K.; McNeill, C. R.; Sirringhaus, H., Charge-Transport Anisotropy in a Uniaxially Aligned Diketopyrrolopyrrole-Based Copolymer. *Adv. Mater.* **2015,** *27*, 7356-7364.

33. Mohammadi, E.; Zhao, C.; Zhang, F.; Qu, G.; Jung, S.-H.; Zhao, Q.; Evans, C. M.; Lee, J.-K.; Shukla, D.; Diao, Y., Ion Gel Dynamic Templates for Large Modulation of Morphology and Charge Transport Properties of Solution-Coated Conjugated Polymer Thin Films. *ACS Appl. Mater. Interfaces* **2019,** *11*, 22561-22574.

34. Mohammadi, E.; Zhao, C.; Meng, Y.; Qu, G.; Zhang, F.; Zhao, X.; Mei, J.; Zuo, J.-M.; Shukla, D.; Diao, Y., Dynamic-Template-Directed Multiscale Assembly for Large-Area Coating of Highly-Aligned Conjugated Polymer Thin Films. *Nat. Commun.* **2017,** *8*, 16070.

35. Le Berre, M.; Chen, Y.; Baigl, D., From Convective Assembly to Landau-Levich Deposition of Multilayered Phospholipid Films of Controlled Thickness. *Langmuir* **2009,** *25*, 2554-2557.

36. Qu, G.; Kwok, J. J.; Mohammadi, E.; Zhang, F.; Diao, Y., Understanding Film-to-Stripe Morphology Instability of Solution Coated Conjugated Polymers. *Submitted to ACS Advanced Materials & Interfaces* **2018**.

37. Schuettfort, T.; Watts, B.; Thomsen, L.; Lee, M.; Sirringhaus, H.; McNeill, C. R., Microstructure of Polycrystalline Pbttt Films: Domain Mapping and Structure Formation. *ACS Nano* **2012,** *6*, 1849-1864.

38. Sauer, T.; Arndt, T.; Batchelder, D. N.; Kalachev, A. A.; Wegner, G., The Structure of Langmuir–Blodgett Films from Substituted Phthalocyaninato-Polysiloxanes. *Thin Solid Films* **1990,** *187*, 357-374.

39. O'Connor, B.; Kline, R. J.; Conrad, B. R.; Richter, L. J.; Gundlach, D.; Toney, M. F.; DeLongchamp, D. M., Anisotropic Structure and Charge Transport in Highly Strain-Aligned Regioregular Poly(3-Hexylthiophene). *Adv. Funct. Mater.* **2011,** *21*, 3697-3705.

40. Patel, S. N.; Su, G. M.; Luo, C.; Wang, M.; Perez, L. A.; Fischer, D. A.; Prendergast, D.; Bazan, G. C.; Heeger, A. J.; Chabinyc, M. L.; Kramer, E. J., Nexafs Spectroscopy Reveals the Molecular Orientation in Blade-Coated Pyridal[2,1,3]Thiadiazole-Containing Conjugated Polymer Thin Films. *Macromolecules* **2015,** *48*, 6606-6616.

41. Schuettfort, T.; Thomsen, L.; McNeill, C. R., Observation of a Distinct Surface Molecular Orientation in Films of a High Mobility Conjugated Polymer. *J. Am. Chem. Soc.* **2013,** *135*, 1092-1101.

42. Gann, E.; Caironi, M.; Noh, Y.-Y.; Kim, Y.-H.; McNeill, C. R., Diffractive X-Ray Waveguiding Reveals Orthogonal Crystalline Stratification in Conjugated Polymer Thin Films. *Macromolecules* **2018,** *51*, 2979-2987.

43. Mohammadi, E.; Qu, G.; Kafle, P.; Jung, S.-H.; Lee, J.-K.; Diao, Y., Design Rules for Dynamic-Template-Directed Crystallization of Conjugated Polymers. *Molecular Systems Design & Engineering* **2019**.

44. Smilgies, D.-M.; Li, R.; Giri, G.; Chou, K. W.; Diao, Y.; Bao, Z.; Amassian, A., Look Fast: Crystallization of Conjugated Molecules During Solution Shearing Probed in-Situ and in Real Time by X-Ray Scattering. *physica status solidi (RRL) – Rapid Research Letters* **2013,** *7*, 177-179.

45. Stöhr, J.; Samant, M. G., Liquid Crystal Alignment by Rubbed Polymer Surfaces: A Microscopic Bond Orientation Model. *J. Electron Spectrosc. Relat. Phenom.* **1999,** *98-99*, 189-207.

46. Furumi, S.; Ichimura, K., Surface-Assisted Photoalignment of Discotic Liquid Crystals by Nonpolarized Light Irradiation of Photo-Cross-Linkable Polymer Thin Films. *J. Phys. Chem. B* **2007,** *111*, 1277-1287.

47. Zhang, F.; Mohammadi, E.; Luo, X.; Strzalka, J.; Mei, J.; Diao, Y., Critical Role of Surface Energy in Guiding Crystallization of Solution-Coated Conjugated Polymer Thin Films. *Langmuir* **2018,** *34*, 1109-1122.

48. Gruber, M.; Jung, S.-H.; Schott, S.; Venkateshvaran, D.; Kronemeijer, A. J.; Andreasen, J. W.; McNeill, C. R.; Wong, W. W. H.; Shahid, M.; Heeney, M.; Lee, J.-K.; Sirringhaus, H., Enabling High-Mobility, Ambipolar Charge-Transport in a Dpp-Benzotriazole Copolymer by Side-Chain Engineering. *Chemical Science* **2015,** *6*, 6949-6960.

49. Jiang, Z., Gixsgui: A Matlab Toolbox for Grazing-Incidence X-Ray Scattering Data Visualization and Reduction, and Indexing of Buried Three-Dimensional Periodic Nanostructured Films. *J. Appl. Crystallogr.* **2015,** *48*, 917-926.

50. White, J. L.; Spruiell, J. E., The Specification of Orientation and Its Development in Polymer Processing. *Polym. Eng. Sci.* **1983,** *23*, 247-256.

51. Tao, Y.; Zohar, H.; Olsen, B. D.; Segalman, R. A., Hierarchical Nanostructure Control in Rod−Coil Block Copolymers with Magnetic Fields. *Nano Lett.* **2007,** *7*, 2742-2746.

52. Himmelberger, S.; Salleo, A., Engineering Semiconducting Polymers for Efficient Charge Transport. *MRS Commun.* **2015,** *5*, 383-395.

53. Noriega, R.; Rivnay, J.; Vandewal, K.; Koch, F. P.; Stingelin, N.; Smith, P.; Toney, M. F.; Salleo, A., A General Relationship between Disorder, Aggregation and Charge Transport in Conjugated Polymers. *Nat. Mater.* **2013,** *12*, 1038-1044.

54. Venkateshvaran, D.; Nikolka, M.; Sadhanala, A.; Lemaur, V.; Zelazny, M.; Kepa, M.; Hurhangee, M.; Kronemeijer, A. J.; Pecunia, V.; Nasrallah, I.; Romanov, I.; Broch, K.; McCulloch, I.; Emin, D.; Olivier, Y.; Cornil, J.; Beljonne, D.; Sirringhaus, H., Approaching Disorder-Free Transport in High-Mobility Conjugated Polymers. *Nature* **2014,** *515*, 384-388.

55. Zhang, X.; Bronstein, H.; Kronemeijer, A. J.; Smith, J.; Kim, Y.; Kline, R. J.; Richter, L. J.; Anthopoulos, T. D.; Sirringhaus, H.; Song, K.; Heeney, M.; Zhang, W.; McCulloch, I.; DeLongchamp, D. M., Molecular Origin of High Field-Effect Mobility in an Indacenodithiophene–Benzothiadiazole Copolymer. *Nat. Commun.* **2013,** *4*, 2238.

56. Pingel, P.; Zen, A.; Abellón, R. D.; Grozema, F. C.; Siebbeles, L. D. A.; Neher, D., Temperature-Resolved Local and Macroscopic Charge Carrier Transport in Thin P3ht Layers. *Adv. Funct. Mater.* **2010,** *20*, 2286-2295.

57. Bolsée, J.-C.; Oosterbaan, W. D.; Lutsen, L.; Vanderzande, D.; Manca, J., The Importance of Bridging Points for Charge Transport in Webs of Conjugated Polymer Nanofibers. *Adv. Funct. Mater.* **2013,** *23*, 862-869.

58. Noriega, R.; Salleo, A.; Spakowitz, A. J., Chain Conformations Dictate Multiscale Charge Transport Phenomena in Disordered Semiconducting Polymers. *Proc. Natl. Acad. Sci. U. S. A.* **2013,** *110*, 16315-16320.

59. Jimison, L. H.; Toney, M. F.; McCulloch, I.; Heeney, M.; Salleo, A., Charge-Transport Anisotropy Due to Grain Boundaries in Directionally Crystallized Thin Films of Regioregular Poly(3-Hexylthiophene). *Adv. Mater.* **2009,** *21*, 1568-1572.

60. Rivnay, J.; Jimison, L. H.; Northrup, J. E.; Toney, M. F.; Noriega, R.; Lu, S.; Marks, T. J.; Facchetti, A.; Salleo, A., Large Modulation of Carrier Transport by Grain-Boundary Molecular Packing and Microstructure in Organic Thin Films. *Nat. Mater.* **2009,** *8*, 952-958.

61. Tseng, H. R.; Phan, H.; Luo, C.; Wang, M.; Perez, L. A.; Patel, S. N.; Ying, L.; Kramer, E. J.; Nguyen, T. Q.; Bazan, G. C.; Heeger, A. J., High-Mobility Field-Effect Transistors Fabricated with Macroscopic Aligned Semiconducting Polymers. *Adv. Mater.* **2014,** *26*, 2993-2998.

62. Soeda, J.; Matsui, H.; Okamoto, T.; Osaka, I.; Takimiya, K.; Takeya, J., Highly Oriented Polymer Semiconductor Films Compressed at the Surface of Ionic Liquids for High-Performance Polymeric Organic Field-Effect Transistors. *Adv. Mater.* **2014,** *26*, 6430-6435.

63. Bucella, S. G.; Luzio, A.; Gann, E.; Thomsen, L.; McNeill, C. R.; Pace, G.; Perinot, A.; Chen, Z.; Facchetti, A.; Caironi, M., Macroscopic and High-Throughput Printing of Aligned Nanostructured Polymer Semiconductors for Mhz Large-Area Electronics. *Nat. Commun.* **2015,** *6*, 8394.

64. Biniek, L.; Leclerc, N.; Heiser, T.; Bechara, R.; Brinkmann, M., Large Scale Alignment and Charge Transport Anisotropy of Pbttt Films Oriented by High Temperature Rubbing. *Macromolecules* **2013,** *46*, 4014-4023.

65. Kyaw, A. K. K.; Lay, L. S.; Peng, G. W.; Changyun, J.; Jie, Z., A Nanogroove-Guided Slot-Die Coating Technique for Highly Ordered Polymer Films and High-Mobility Transistors. *Chem. Commun.* **2015,** *52*, 358-361.

66. Tseng, H. R.; Ying, L.; Hsu, B. B.; Perez, L. A.; Takacs, C. J.; Bazan, G. C.; Heeger, A. J., High Mobility Field Effect Transistors Based on Macroscopically Oriented Regioregular Copolymers. *Nano Lett.* **2012,** *12*, 6353-6357.

67. DeLongchamp, D. M.; Kline, R. J.; Jung, Y.; Germack, D. S.; Lin, E. K.; Moad, A. J.; Richter, L. J.; Toney, M. F.; Heeney, M.; McCulloch, I., Controlling the Orientation of Terraced Nanoscale "Ribbons" of a Poly(Thiophene) Semiconductor. *ACS Nano* **2009,** *3*, 780-787.

68. Shaw, L.; Hayoz, P.; Diao, Y.; Reinspach, J. A.; To, J. W. F.; Toney, M. F.; Weitz, R. T.; Bao, Z., Direct Uniaxial Alignment of a Donor-Acceptor Semiconducting Polymer Using Single-Step Solution Shearing. *ACS Appl. Mater. Interfaces* **2016,** *8*, 9285-9296.

69. Chang, J.; Lin, Z.; Li, J.; Lim, S. L.; Wang, F.; Li, G.; Zhang, J.; Wu, J., Enhanced Polymer Thin Film Transistor Performance by Carefully Controlling the Solution Self-Assembly and Film Alignment with Slot Die Coating. *Adv. Electron. Mater.* **2015,** *1*, 150036.

70. Joseph Kline, R.; McGehee, M. D.; Toney, M. F., Highly Oriented Crystals at the Buried Interface in Polythiophene Thin-Film Transistors. *Nat. Mater.* **2006,** *5*, 222-228.

71. Himmelberger, S.; Dacuña, J.; Rivnay, J.; Jimison, L. H.; McCarthy-Ward, T.; Heeney, M.; McCulloch, I.; Toney, M. F.; Salleo, A., Effects of Confinement on Microstructure and Charge Transport in High Performance Semicrystalline Polymer Semiconductors. *Adv. Funct. Mater.* **2013,** *23*, 2091-2098.

72. Giri, G.; Verploegen, E.; Mannsfeld, S. C.; Atahan-Evrenk, S.; Kim do, H.; Lee, S. Y.; Becerril, H. A.; Aspuru-Guzik, A.; Toney, M. F.; Bao, Z., Tuning Charge Transport in Solution-Sheared Organic Semiconductors Using Lattice Strain. *Nature* **2011,** *480*, 504-508.

73. Becerril, H. A.; Roberts, M. E.; Liu, Z.; Locklin, J.; Bao, Z., High-Performance Organic Thin-Film Transistors through Solution-Sheared Deposition of Small-Molecule Organic Semiconductors. *Adv. Mater.* **2008,** *20*, 2588-2594.

74. Deegan, R. D.; Bakajin, O.; Dupont, T. F.; Huber, G.; Nagel, S. R.; Witten, T. A., Capillary Flow as the Cause of Ring Stains from Dried Liquid Drops. *Nature* **1997,** *389*, 827-829.

75. Köhler, A.; dos Santos, D. A.; Beljonne, D.; Shuai, Z.; Brédas, J. L.; Holmes, A. B.; Kraus, A.; Müllen, K.; Friend, R. H., Charge Separation in Localized and Delocalized Electronic States in Polymeric Semiconductors. *Nature* **1998,** *392*, 903-906.

76. Comoretto, D.; Dellepiane, G.; Marabelli, F.; Cornil, J.; dos Santos, D. A.; Bredas, J. L.; Moses, D., Optical Constants of Highly Stretch-Oriented Poly(P-Phenylene-Vinylene): A Joint Experimental and Theoretical Study. *Phys. Rev. B* **2000,** *62*, 10173-10184.

77. Gather, M. C.; Bradley, D. D. C., An Improved Optical Method for Determining the Order Parameter in Thin Oriented Molecular Films and Demonstration of a Highly Axial Dipole Moment for the Lowest Energy Π–Π* Optical Transition in Poly(9,9- Dioctylfluorene-Co-Bithiophene). *Adv. Funct. Mater.* **2007,** *17*, 479-485.

78. Vezie, M. S.; Few, S.; Meager, I.; Pieridou, G.; Dorling, B.; Ashraf, R. S.; Goni, A. R.; Bronstein, H.; McCulloch, I.; Hayes, S. C.; Campoy-Quiles, M.; Nelson, J., Exploring the Origin of High Optical Absorption in Conjugated Polymers. *Nat. Mater.* **2016,** *15*, 746-753.

79. O'Connor, B. T.; Reid, O. G.; Zhang, X.; Kline, R. J.; Richter, L. J.; Gundlach, D. J.; DeLongchamp, D. M.; Toney, M. F.; Kopidakis, N.; Rumbles, G., Morphological Origin of Charge

Transport Anisotropy in Aligned Polythiophene Thin Films. *Adv. Funct. Mater.* **2014,** *24*, 3422-3431.

80. Rivnay, J.; Mannsfeld, S. C.; Miller, C. E.; Salleo, A.; Toney, M. F., Quantitative Determination of Organic Semiconductor Microstructure from the Molecular to Device Scale. *Chem. Rev.* **2012,** *112*, 5488-5519.

81. DeLongchamp, D. M.; Kline, R. J.; Fischer, D. A.; Richter, L. J.; Toney, M. F., Molecular Characterization of Organic Electronic Films. *Adv. Mater.* **2011,** *23*, 319-337.

82. Kim, J. B.; Lee, S.; Toney, M. F.; Chen, Z.; Facchetti, A.; Kim, Y. S.; Loo, Y.-L., Reversible Soft-Contact Lamination and Delamination for Non-Invasive Fabrication and Characterization of Bulk-Heterojunction and Bilayer Organic Solar Cells. *Chem. Mater.* **2010,** *22*, 4931-4938.

83. Chabinyc, M. L.; Salleo, A.; Wu, Y.; Liu, P.; Ong, B. S.; Heeney, M.; McCulloch, I., Lamination Method for the Study of Interfaces in Polymeric Thin Film Transistors. *J. Am. Chem. Soc.* **2004,** *126*, 13928-13929.

84. Wang, G.; Persson, N.; Chu, P.-H.; Kleinhenz, N.; Fu, B.; Chang, M.; Deb, N.; Mao, Y.; Wang, H.; Grover, M. A.; Reichmanis, E., Microfluidic Crystal Engineering of Π-Conjugated Polymers. *ACS Nano* **2015,** *9*, 8220-8230.

85. Coropceanu, V.; Cornil, J.; da Silva Filho, D. A.; Olivier, Y.; Silbey, R.; Bredas, J. L., Charge Transport in Organic Semiconductors. *Chem. Rev.* **2007,** *107*, 926-952.

86. Bittle, E. G.; Basham, J. I.; Jackson, T. N.; Jurchescu, O. D.; Gundlach, D. J., Mobility Overestimation Due to Gated Contacts in Organic Field-Effect Transistors. *Nat. Commun.* **2016,** *7*, 10908.

87. Uemura, T.; Rolin, C.; Ke, T.-H.; Fesenko, P.; Genoe, J.; Heremans, P.; Takeya, J., On the Extraction of Charge Carrier Mobility in High-Mobility Organic Transistors. *Adv. Mater.* **2016,** *28*, 151-155.

88. Lee, W. H.; Cho, J. H.; Cho, K., Control of Mesoscale and Nanoscale Ordering of Organic Semiconductors at the Gate Dielectric/Semiconductor Interface for Organic Transistors. *J. Mater. Chem.* **2010,** *20*, 2549-2561.

89. Doumenc, F.; Guerrier, B., Drying of a Solution in a Meniscus: A Model Coupling the Liquid and the Gas Phases. *Langmuir* **2010,** *26*, 13959-13967.

90. Hsueh, C.; Doumenc, F.; Guerrier, B., Numerical Simulation of Complex Fluid Drying in a Hele-Shaw Cell. *Eur. Phys. J.-Spec. Top.* **2013,** *219*, 51-57.

91. Doumenc, F.; Salmon, J. B.; Guerrier, B., Modeling Flow Coating of Colloidal Dispersions in the Evaporative Regime: Prediction of Deposit Thickness. *Langmuir* **2016,** *32*, 13657-13668.

92. Romero, O. J.; Suszynski, W. J.; Scriven, L. E.; Carvalho, M. S., Low-Flow Limit in Slot Coating of Dilute Solutions of High Molecular Weight Polymer. *J. Non-Newtonian Fluid Mech.* **2004,** *118*, 137-156.

93. Trebbin, M.; Steinhauser, D.; Perlich, J.; Buffet, A.; Roth, S. V.; Zimmermann, W.; Thiele, J.; Forster, S., Anisotropic Particles Align Perpendicular to the Flow Direction in Narrow Microchannels. *Proc. Natl. Acad. Sci. U. S. A.* **2013,** *110*, 6706-6711.

94. Parsa, S.; Guasto, J. S.; Kishore, M.; Ouellette, N. T.; Gollub, J. P.; Voth, G. A., Rotation and Alignment of Rods in Two-Dimensional Chaotic Flow. *Phys. Fluids* **2011,** *23*, 043302.

95. Qazi, S. J.; Rennie, A. R.; Tucker, I.; Penfold, J.; Grillo, I., Alignment of Dispersions of Plate-Like Colloidal Particles of Ni(Oh)2 Induced by Elongational Flow. *J. Phys. Chem. B* **2011,** *115*, 3271-3280.

96. Franceschini, A.; Filippidi, E.; Guazzelli, E.; Pine, D. J., Transverse Alignment of Fibers in a Periodically Sheared Suspension: An Absorbing Phase Transition with a Slowly Varying Control Parameter. *Phys. Rev. Lett.* **2011,** *107*, 250603.

97. Xie, D.; Lista, M.; Qiao, G. G.; Dunstan, D. E., Shear Induced Alignment of Low Aspect Ratio Gold Nanorods in Newtonian Fluids. *J. Phys. Chem. Lett.* **2015,** *6*, 3815-3820.

98. Lambert, G. M.; Baird, D. G., Evaluating Rigid and Semiflexible Fiber Orientation Evolution Models in Simple Flows. *J. Manuf. Sci. Eng.* **2016,** *139*, 031012.

99. Chen, Z.; Lee, M. J.; Shahid Ashraf, R.; Gu, Y.; Albert-Seifried, S.; Meedom Nielsen, M.; Schroeder, B.; Anthopoulos, T. D.; Heeney, M.; McCulloch, I.; Sirringhaus, H., High-Performance Ambipolar Diketopyrrolopyrrole-Thieno[3,2-B]Thiophene Copolymer Field-Effect Transistors with Balanced Hole and Electron Mobilities. *Adv. Mater.* **2012,** *24*, 647-652.

100. Glinka, C. J.; Barker, J. G.; Hammouda, B.; Krueger, S.; Moyer, J. J.; Orts, W. J., The 30 M Small-Angle Neutron Scattering Instruments at the National Institute of Standards and Technology. *J. Appl. Crystallogr.* **1998,** *31*, 430-445.

101. Kline, S., Reduction and Analysis of Sans and Usans Data Using Igor Pro. *J. Appl. Crystallogr.* **2006,** *39*, 895-900.

102. Alina, G.; Bakker, J.; Bouwman, W.; Butler, P.; Campbell, K.; Cho, J.-H.; Hernandez, R. C.; Doucet, M.; Gonzalez, M.; Heenan, R.; Jackson, A.; Kienzle, P.; King, S.; Kline, S.; Kryzwon, J.; Mannicke, D.; Markvardsen, A.; Nielsen, T.; Parker, P.; Richter, T.; Whitley, R.; Zhou, J. Sasview for Small Angle Scattering Analysis. http://www.sasview.org/ (accessed Apr.).

103. Jiang, Z.; Li, X.; Strzalka, J.; Sprung, M.; Sun, T.; Sandy, A. R.; Narayanan, S.; Lee, D. R.; Wang, J., The Dedicated High-Resolution Grazing-Incidence X-Ray Scattering Beamline 8-Id-E at the Advanced Photon Source. *J. Synchrotron Radiat.* **2012,** *19*, 627-636.

104. Oh, J. H.; Lee, H. W.; Mannsfeld, S.; Stoltenberg, R. M.; Jung, E.; Jin, Y. W.; Kim, J. M.; Yoo, J.-B.; Bao, Z., Solution-Processed, High-Performance N-Channel Organic Microwire Transistors. *Proc. Natl. Acad. Sci. U. S. A.* **2009,** *106*, 6065-6070.

105. Thiele, U., Patterned Deposition at Moving Contact Lines. *Adv. Colloid Interface Sci.* **2014,** *206*, 399-413.

106. Deblais, A.; Harich, R.; Colin, A.; Kellay, H., Taming Contact Line Instability for Pattern Formation. *Nat. Commun.* **2016,** *7*, 12458.

107. Lee, D. Y.; Pham, J. T.; Lawrence, J.; Lee, C. H.; Parkos, C.; Emrick, T.; Crosby, A. J., Macroscopic Nanoparticle Ribbons and Fabrics. *Adv. Mater.* **2013,** *25*, 1248-1253.

108. Liu, Y.; Lee, D. Y.; Monteux, C.; Crosby, A. J., Hyperbranched Polymer Structures Via Flexible Blade Flow Coating. *J. Polym. Sci. B* **2016,** *54*, 32-37.

109. Yabu, H.; Shimomura, M., Preparation of Self-Organized Mesoscale Polymer Patterns on a Solid Substrate: Continuous Pattern Formation from a Receding Meniscus. *Adv. Funct. Mater.* **2005,** *15*, 575-581.

110. Watanabe, S.; Mino, Y.; Ichikawa, Y.; Miyahara, M. T., Spontaneous Formation of Cluster Array of Gold Particles by Convective Self-Assembly. *Langmuir* **2012,** *28*, 12982-12988.

111. Farcau, C.; Moreira, H.; Viallet, B.; Grisolia, J.; Ressier, L., Tunable Conductive Nanoparticle Wire Arrays Fabricated by Convective Self-Assembly on Nonpatterned Substrates. *ACS Nano* **2010,** *4*, 7275-7282.

112. Diao, Y.; Tee, B. C.; Giri, G.; Xu, J.; Kim, D. H.; Becerril, H. A.; Stoltenberg, R. M.; Lee, T. H.; Xue, G.; Mannsfeld, S. C.; Bao, Z., Solution Coating of Large-Area Organic Semiconductor Thin Films with Aligned Single-Crystalline Domains. *Nat. Mater.* **2013,** *12*, 665-671.

113. Zhang, F.; Qu, G.; Mohammadi, E.; Mei, J.; Diao, Y., Solution-Processed Nanoporous Organic Semiconductor Thin Films: Toward Health and Environmental Monitoring of Volatile Markers. *Adv. Funct. Mater.* **2017,** *27*, 1701117.

114. Wang, G.; Huang, W.; Eastham, N. D.; Fabiano, S.; Manley, E. F.; Zeng, L.; Wang, B.; Zhang, X.; Chen, Z.; Li, R.; Chang, R. P. H.; Chen, L. X.; Bedzyk, M. J.; Melkonyan, F. S.; Facchetti, A.; Marks, T. J., Aggregation Control in Natural Brush-Printed Conjugated Polymer Films and Implications for Enhancing Charge Transport. *Proc. Natl. Acad. Sci.* **2017**.

115. McCulloch, I.; Salleo, A.; Chabinyc, M., Avoid the Kinks When Measuring Mobility. *Science* **2016,** *352*, 1521-1522.

116. Muller-Buschbaum, P.; Bauer, E.; Maurer, E.; Roth, S. V.; Gehrke, R.; Burghammer, M.; Riekel, C., Large-Scale and Local-Scale Structures in Polymer-Blend Films: A Grazing-Incidence Ultra-Small-Angle X-Ray Scattering and Sub-Microbeam Grazing-Incidence Small-Angle X-Ray Scattering Investigation. *J. Appl. Crystallogr.* **2007,** *40*, s341-s345.

117. Roth, S. V.; Rothkirch, A.; Autenrieth, T.; Gehrke, R.; Wroblewski, T.; Burghammer, M. C.; Riekel, C.; Schulz, L.; Hengstler, R.; Müller-Buschbaum, P., Spatially Resolved Investigation of Solution Cast Nanoparticle Films by X-Ray Scattering and Multidimensional Data Set Classification. *Langmuir* **2010,** *26*, 1496-1500.

118. Fraštia, Ľ.; Archer, A. J.; Thiele, U., Modelling the Formation of Structured Deposits at Receding Contact Lines of Evaporating Solutions and Suspensions. *Soft Matter* **2012,** *8*, 11363.

119. Doumenc, F.; Guerrier, B., Self-Patterning Induced by a Solutal Marangoni Effect in a Receding Drying Meniscus. *EPL-Europhys. Lett.* **2013,** *103*, 14001.

120. Lee, J.; Son, G., Numerical Simulation of Stick-Slip Contact Line Motion and Particle Line Formation in Dip Coating. *Int. J. Heat Mass Transf.* **2016,** *74*, 98-107.

121. Orejon, D.; Sefiane, K.; Shanahan, M. E., Stick-Slip of Evaporating Droplets: Substrate Hydrophobicity and Nanoparticle Concentration. *Langmuir* **2011,** *27*, 12834-12843.

122. Bormashenko, E.; Musin, A.; Zinigrad, M., Evaporation of Droplets on Strongly and Weakly Pinning Surfaces and Dynamics of the Triple Line. *Colloids Surf. A* **2011,** *385*, 235-240.

123. Bodiguel, H.; Doumenc, F.; Guerrier, B., Stick-Slip Patterning at Low Capillary Numbers for an Evaporating Colloidal Suspension. *Langmuir* **2010,** *26*, 10758-10763.

124. Li, B.; Han, W.; Jiang, B.; Lin, Z., Crafting Threads of Diblock Copolymer Micelles Via Flow-Enabled Self-Assembly. *ACS Nano* **2014,** *8*, 2936-2942.

125. Shanahan, M. E. R., Simple Theory of "Stick-Slip" Wetting Hysteresis. *Langmuir* **1995,** *11*, 1041-1043.

126. Denison, K. R.; Boxall, C., Photoinduced “Stick−Slip” on Superhydrophilic Semiconductor Surfaces. *Langmuir* **2007,** *23*, 4358-4366.

127. Kwok, D. Y.; Neumann, A. W., Contact Angle Measurement and Contact Angle Interpretation. *Adv. Colloid Interface Sci.* **1999,** *81*, 167-249.

128. Bucher, I. Circle Fit. https://www.mathworks.com/matlabcentral/fileexchange/5557-circle-fit?focused=5059278&tab=function (accessed May 10).

129. Stauffer, C. E., The Measurement of Surface Tension by the Pendant Drop Technique. *J. Phys. Chem.* **1965,** *69*, 1933-1938.

130. Zuo, B.; Hu, Y.; Lu, X.; Zhang, S.; Fan, H.; Wang, X., Surface Properties of Poly(Vinyl Alcohol) Films Dominated by Spontaneous Adsorption of Ethanol and Governed by Hydrogen Bonding. *The Journal of Physical Chemistry C* **2013,** *117*, 3396-3406.

131. Narita, T.; Hébraud, P.; Lequeux, F., Effects of the Rate of Evaporation and Film Thickness on Nonuniform Drying of Film-Forming Concentrated Colloidal Suspensions. *The European Physical Journal E* **2005,** *17*, 69-76.

132. Shaw, L.; Yan, H.; Gu, X.; Hayoz, P.; Weitz, R. T.; Kaelblein, D.; Toney, M. F.; Bao, Z., Microstructural Evolution of the Thin Films of a Donor–Acceptor Semiconducting Polymer Deposited by Meniscus-Guided Coating. *Macromolecules* **2018,** *51*, 4325-4340.

133. Srivastava, N.; Burns, M. A., Analysis of Non-Newtonian Liquids Using a Microfluidic Capillary Viscometer. *Anal. Chem.* **2006,** *78*, 1690-1696.

134. Krall, A. H.; Sengers, J. V.; Kestin, J., Viscosity of Liquid Toluene at Temperatures from 25 to 150.Degree.C and at Pressures up to 30 Mpa. *J. Chem. Eng. Data* **1992,** *37*, 349-355.

135. Lei, T.; Dou, J.-H.; Pei, J., Influence of Alkyl Chain Branching Positions on the Hole Mobilities of Polymer Thin-Film Transistors. *Adv. Mater.* **2012,** *24*, 6457-6461.

Appendix A. Detailed X-ray results and Microscopy Images for Study of Lyotropic Liquid Crystalline Conjugated Polymers

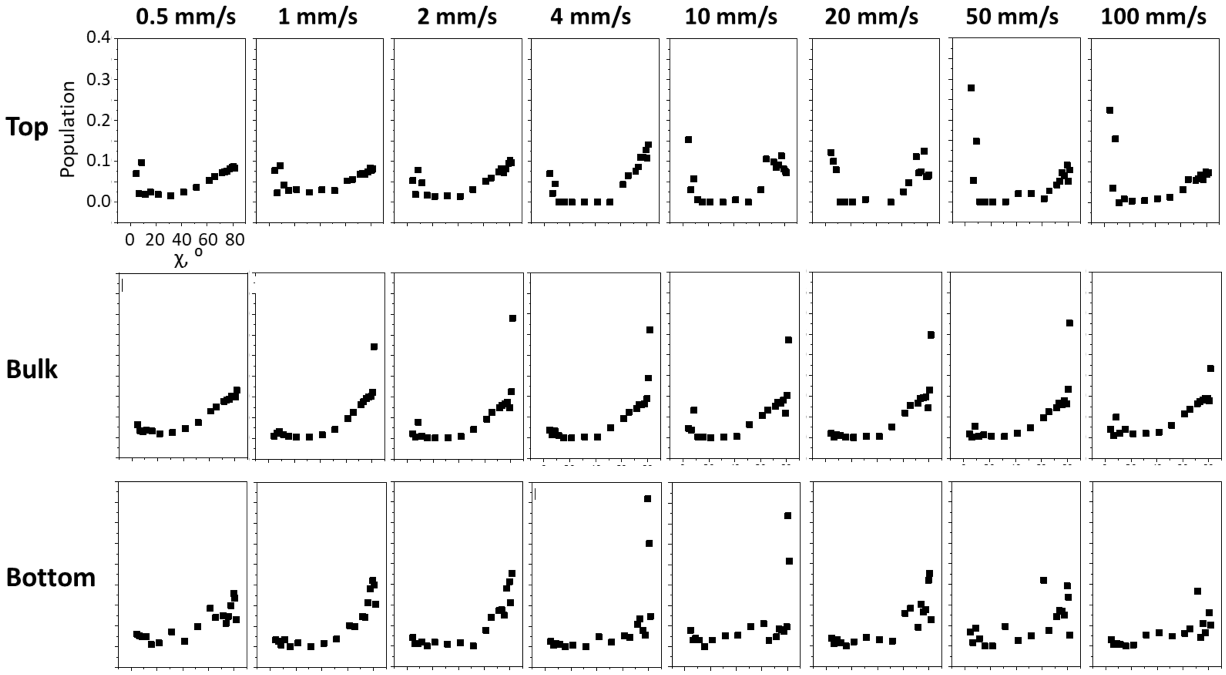

Figure A1. Partial pole figures for top, bulk and bottom measurements of DPP-BTz thin films coated on SiO_2 substrates between 0.5 mm/s and 100 mm/s

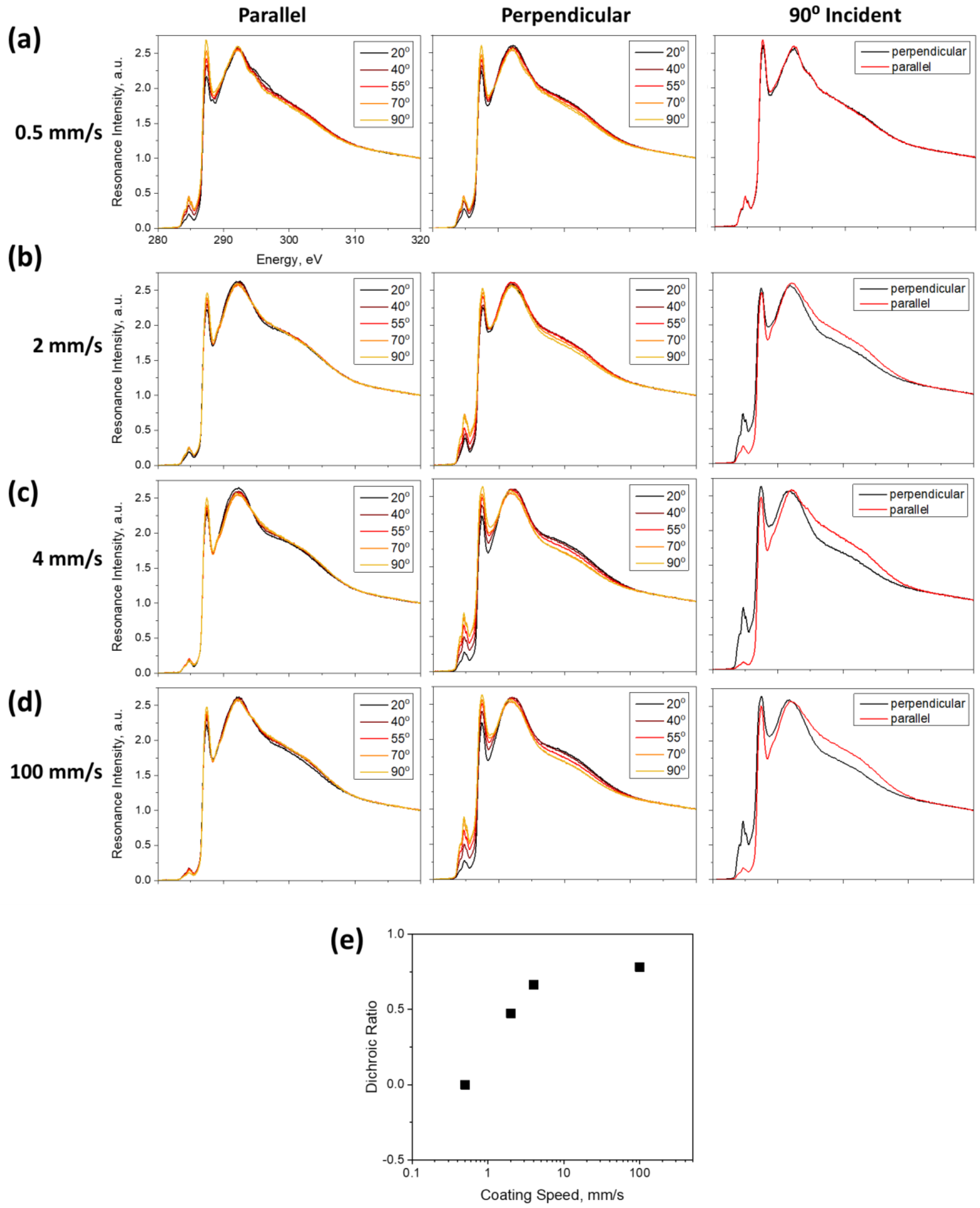

Figure A2. NEXAFS PEY tilt angle spectra of DPP-BTz thin films coated at (a) 0.5 mm/s, (b) 2 mm/s, (c) 4 mm/s and (d) 100 mm/s, measured with the incident X-ray beam parallel and perpendicular to the coating direction. The parallel and perpendicular scans with 90⁰ incident angle are plotted for in-plane alignment evaluation. (e) Calculated dichroic ratio of in-plane alignment at the top interface.

Table A1. Out-of-plane 2D orientation parameter of DPP-BTz speed series thin films from GIWAXS and NEXAFS measurements.

Coating speed, mm/s	GIWAXS top	GIWAXS bulk	GIWAXS bottom	NEXAFS top
0.5	-0.48	-0.57	-0.51	0.60
1	-0.41	-0.68	-0.70	
2	-0.52	-0.70	-0.72	0.61
4	-0.66	-0.71	-0.71	0.63
10	-0.66	-0.66	-0.62	
20	-0.56	-0.69	-0.61	
50	-0.51	-0.66	-0.55	
100	-0.54	-0.59	-0.60	0.65

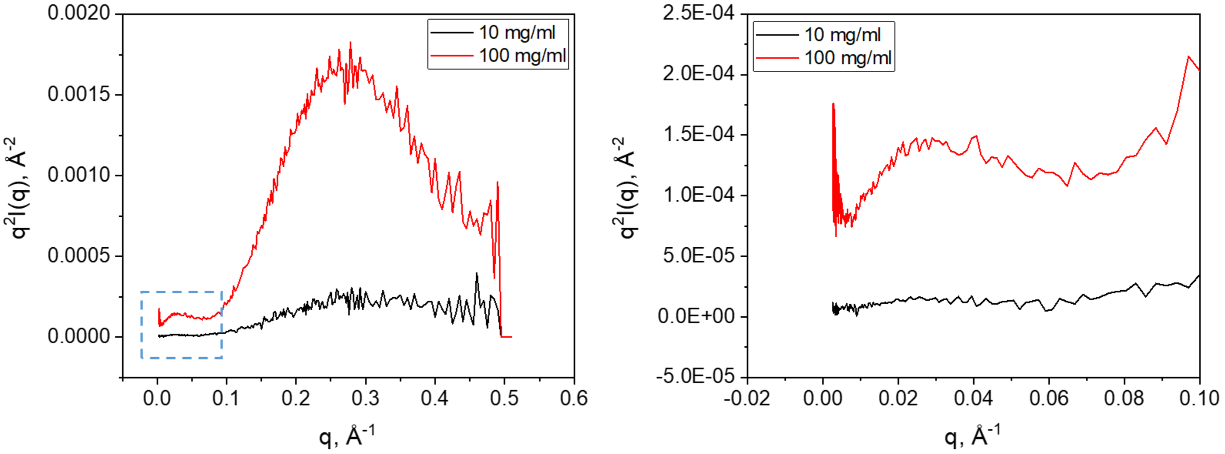

Figure A3. Kratky plot for background subtracted solution SAXS profile of 10 mg/ml and 100 mg/ml DPP-BTz in chlorobenzene solution measured at 85 ºC. The q = 0 – 0.1 Å^{-1} is zoomed in for better visualization of the peak in this range.

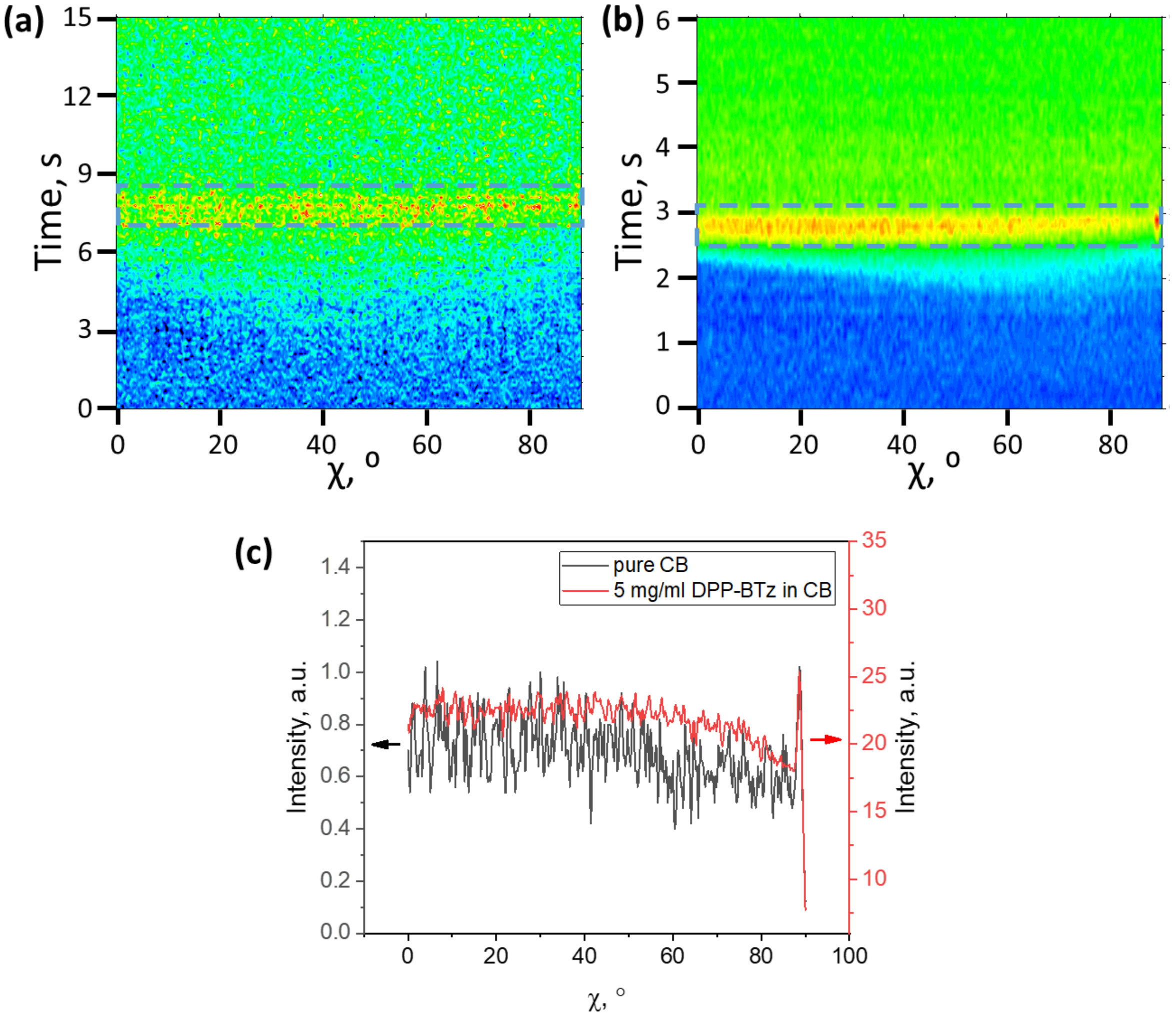

Figure A4. Normalized intensity-time-χ plot of the transient peak (q = 0.8 – 0.95 Å^{-1}) for solution coating of (a) pure chlorobenzene and (b) 5 mg/ml DPP-BTz in chlorobenzene solution. The time scale reflected real time but with arbitrary start point.

Table A2. Out-of-plane 2D orientation parameter of DPP-BTz substrate series thin films from GIWAXS measurements.

Substrate	Surface energy mN/m	GIWAXS top	GIWAXS bulk	GIWAXS bottom
OTS	20.5	-0.55	-0.54	-0.52
PVDF-HFP	27.6	-0.51	-0.53	-0.47
PTS	36.0	-0.53	-0.60	-0.62
PVP-HDA	41.7	-0.50	-0.56	-0.52
SiO_2	52.2	-0.49	-0.58	-0.52

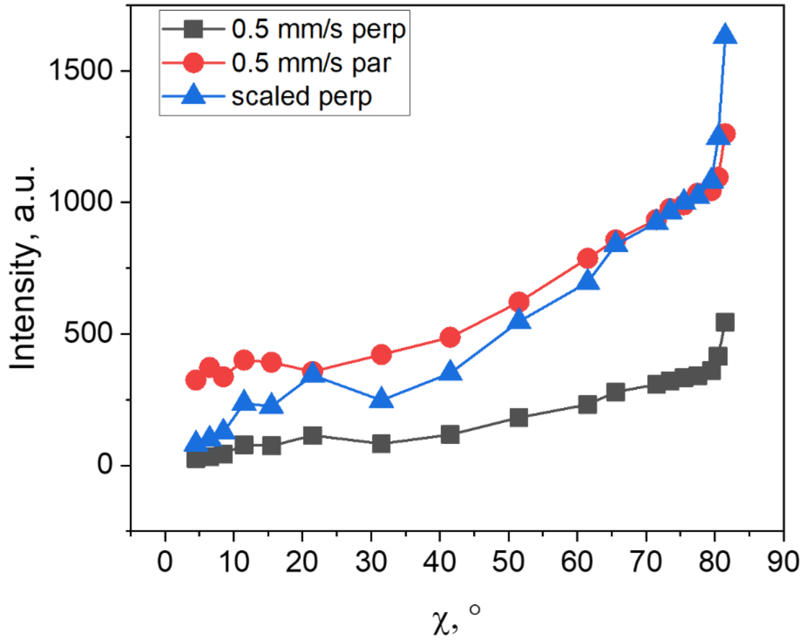

Figure A5. Pole figure comparison from DPP-BTz thin film coated from in situ μGIWAXS measurements. Measurements is performed with the incident X-ray beam paralle and perpendicular to coating direction for films coated from 5 mg/ml DPP-BTz in chlorobenzene solution on SiO_2 substrate at 70 °C. The perpendicular intensity is scalled to compare with parallel intensity.

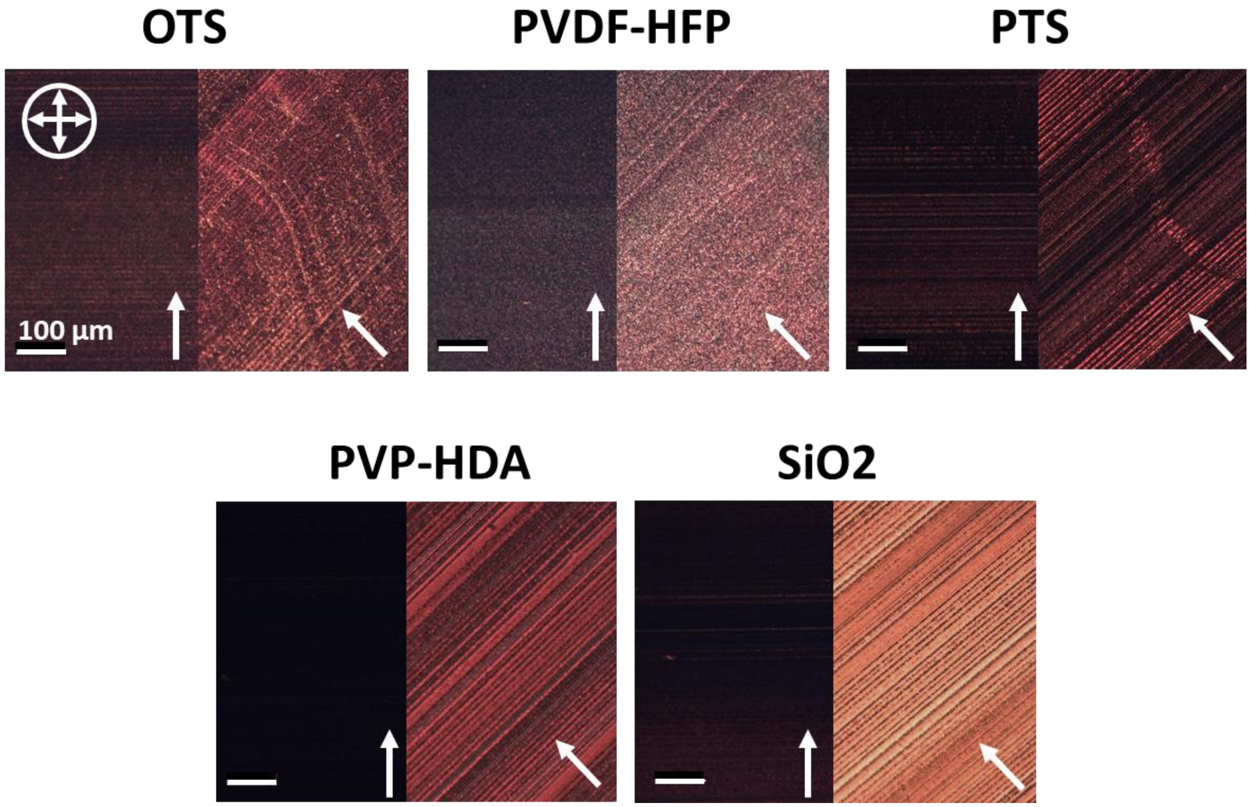

Figure A6. Cross polarized microscopy images of solution coated DPP-BTz on OTS, PVDF-HFP, PTS, PVP-HDA and SiO^2 substrates at 0.5 mm/s and 80 ºC.

Appendix B. Detailed Characterization Results and Alignment Mechanism Study for Conjugated Polymer Alignment

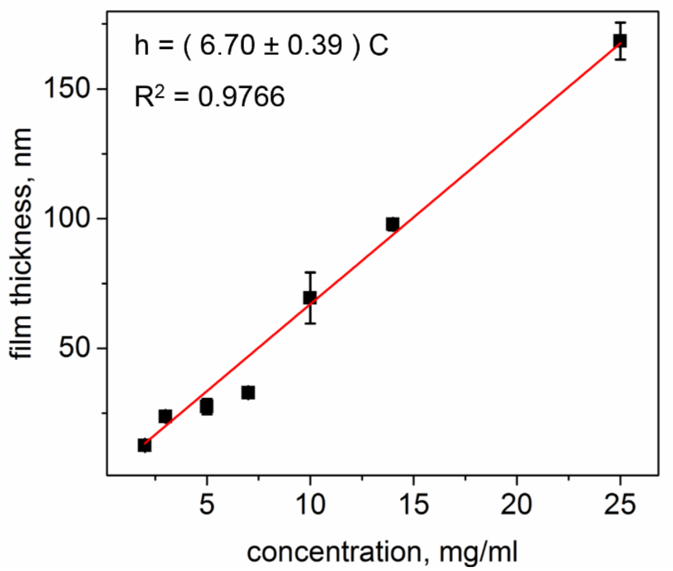

Figure B1. Film thickness as a function of solution concentration. The evaporation rate of the solvent can be calculated from the evaporation regime model by Le Berre *et. al.* in meniscus guided coating derived from mass balance.[1] The equation is $Q_{evap} = \frac{h\rho Lv}{C}$, where h is the thickness of the film, ρ is the density of the solute, L is the width of the meniscus, ν is the speed of the moving blade or substrate and C is the solution concentration. In this equation, Qevap is the evaporation rate in volume per time. The density of the solute (DPP2T-TT) is 1 g/cm^3, the blade velocity is 0.5 mm/s, and the width of the meniscus is 1 cm. The slope from Figure S1 is $\frac{h}{C} = 6.7\frac{nm}{mg/cm^3}$. Therefore, the averaged evaporation rate across all concentration is $Q_{evap} = 0.0355\frac{mm^3}{s}$.

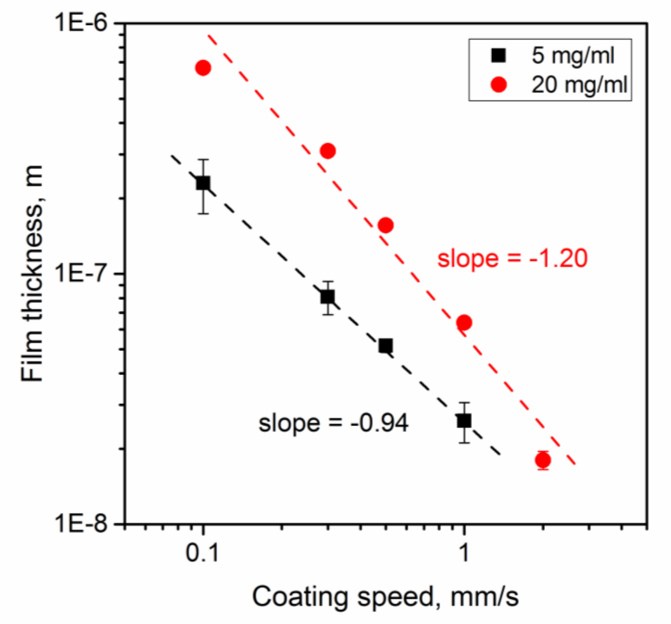

Figure B2. Film thickness and coating speed relation for DPP2T-TT coated from chloroform. Mass balance in the evaporation regime by Le Berre et al.[1] indicates the relationship between film thickness and coating speed satisfy equation $h = \frac{Q_{evap}\rho L}{c} v^{-1}$. From a double logarithm plot of film thickness versus coating speed, the exponent for coating speed equals to the slope and the value of the evaporation rate is embedded in the intercept. Because of the good agreement between the slopes (α5 = -0.94 and α20 = -1.20) in the figure with the mass balance equation (α = -1), we can confidently state that the experiments presented in the manuscript falls in the evaporation regime.

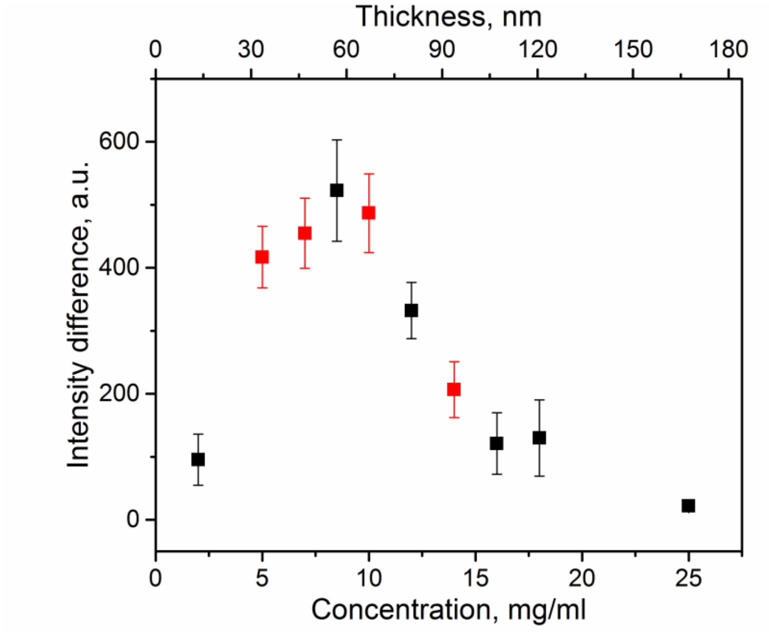

Figure B3. Birefringence of solution coated films as a function of film thickness/solution concentration. The birefringence is calculated as the average intensity difference between the optical images of films with coating direction oriented 0° and 45° with respect to the axis of the polarizer. The data points in red correspond to images presented in Figure 1 with film thickness of 28 nm, 33 nm, 69 nm and 98 nm respectively. Error bars were from intensity obtained from multiple data points on one image.

SANS measurements.

SANS profiles for DPPTT dissolved in chloroform can be seen in Figure S4 & Table S1. The polymers are fit with a cylinder model form factor as described in the following equation:[2]

$$I(q) = \frac{scale}{V} \int_0^{\pi/2} \left(2(\Delta\rho)V \frac{\sin(qL\cos\alpha/2)}{(qL\cos\alpha/2)} \frac{J_1(qr\sin\alpha)}{(qr\sin\alpha)} \right)^2 \sin\alpha \, d\alpha + bkg \qquad \text{(Eqn. B1)}$$

where V is the volume of the cylinder, r is the radius of the cylinder, L is the length of the cylinder, $\Delta\rho$ is the scattering length density contrast between the solvent and cylinder and *bkg* is the scattering background. All fits show good agreement with the model at $q > 0.02$ Å^{-1}. The radius of the cylinder (*e.g.,* polymer backbone) was found to be concentration independent at 1.7 nm. However, an inverse relationship is observed between concentration and the length of isolated cylinders obtained from fitting. This behavior is consistent with increased interchain interactions for polymer solutions above c^* (*i.e.,* critical overlap concentration).[3] Figure S7 also shows that at low-q the cylinder model deviates from the scattering. As the polymer concentration increases the point of deviation, indicated by an arrow in the figure, shifts to higher-q (*i.e.,* shorter length scales). This increase in low-q scattering is also consistent with interchain interactions and the shift to higher-q indicates interactions are happening at smaller length scales.

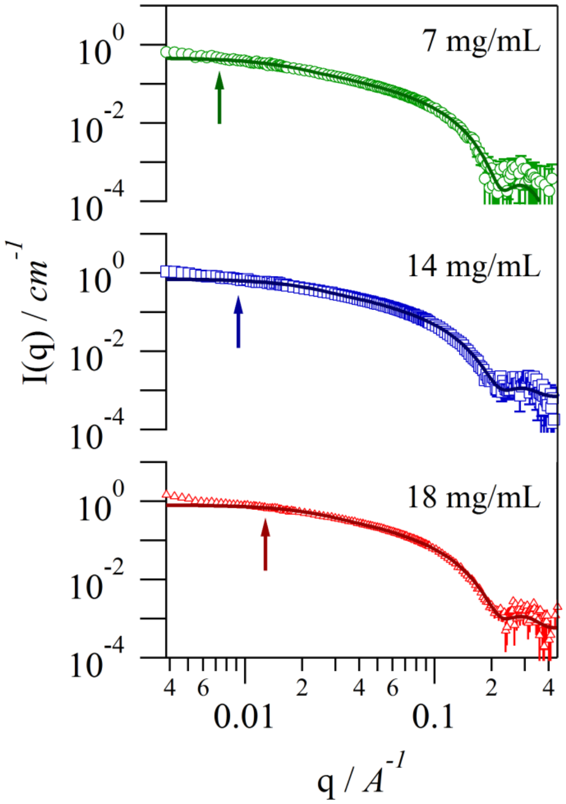

Figure B4. SANS profiles for DPPTT dissolved in chloroform at different concentrations. Solid lines correspond to cylinder model fits. Arrows highlight deviation from the model at low-*q*.

Table B1. Parameters extracted from the fitting of SANS profiles (Figure 2.1) with a cylinder model (Equation B1).

Concentration (mg/mL)	Cylinder Radius (nm)	Cylinder Length (nm)	Interchain Interaction Length Scale (nm)
7	1.7	28	84
14	1.7	22	69
18	1.7	19	49

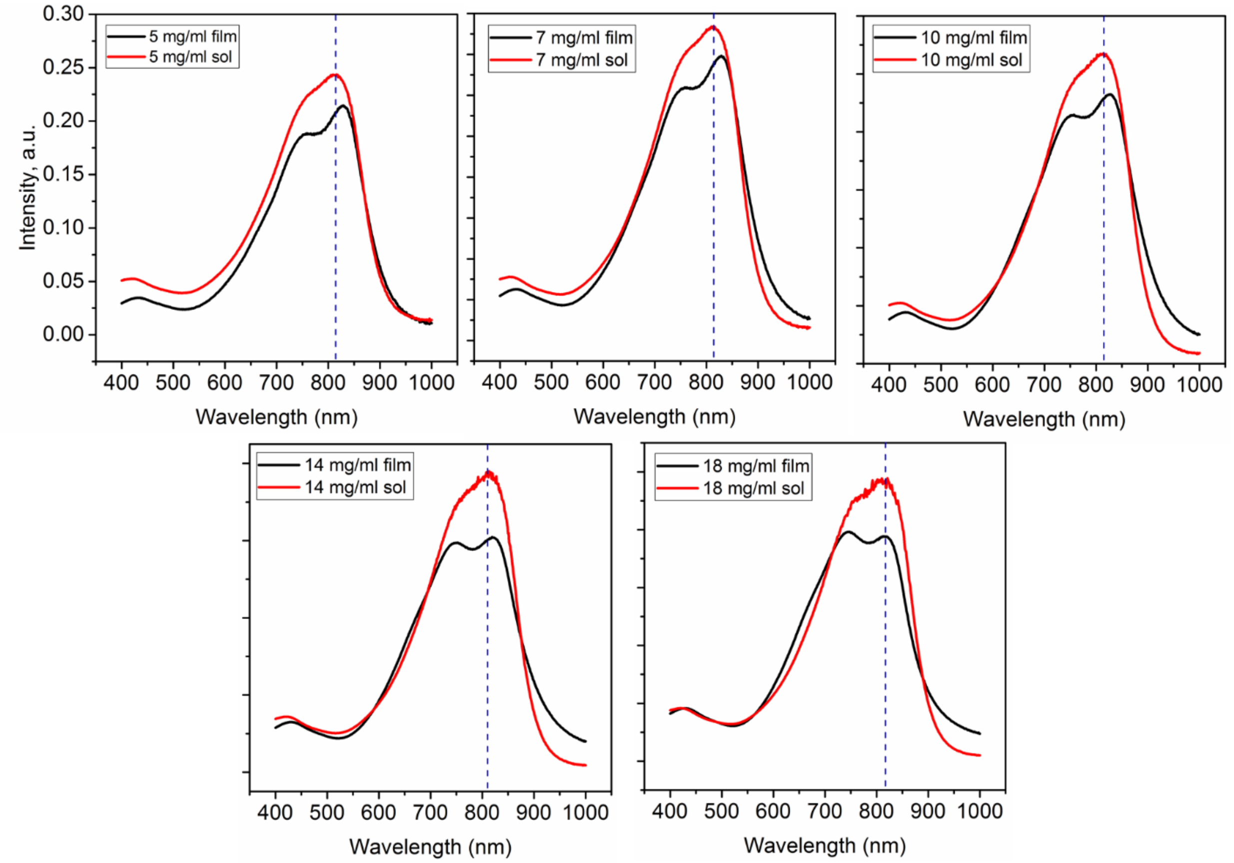

Figure B5. Solution state and corresponding solid state UV-vis spectra for DPP2T-TT at various concentrations. Consistent position and shape of the solution state spectra at all concentrations indicate similar polymer conformation and aggregation state. Blue shift of the solid state spectra indicates increasing aggregation with increasing concentration in thin films.

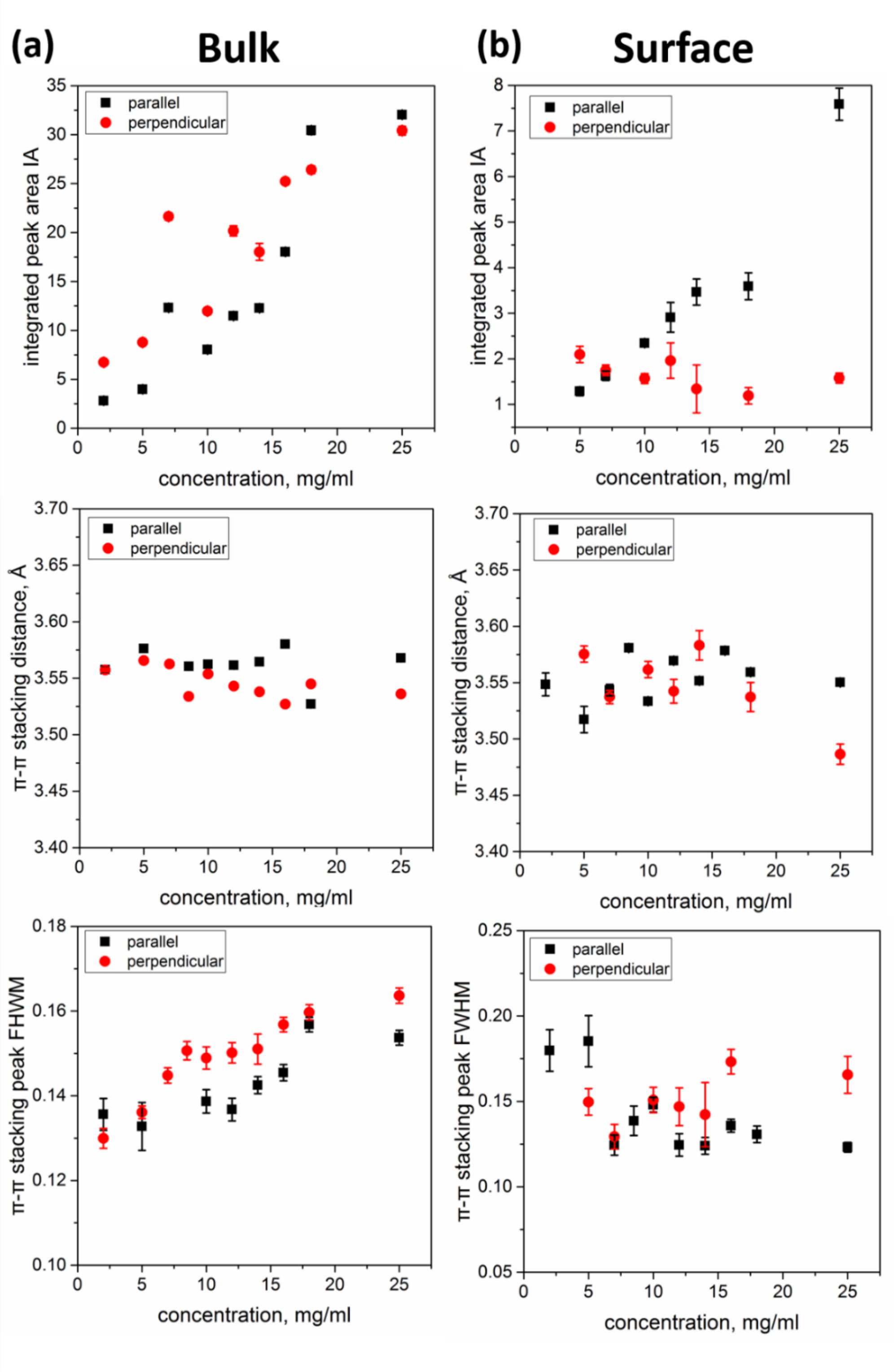

Figure B6. GIWAXS analysis performed on the edge-on π-π stacking peak from parallel and perpendicular measurements for the (a) bulk film and (b) air-film interface.

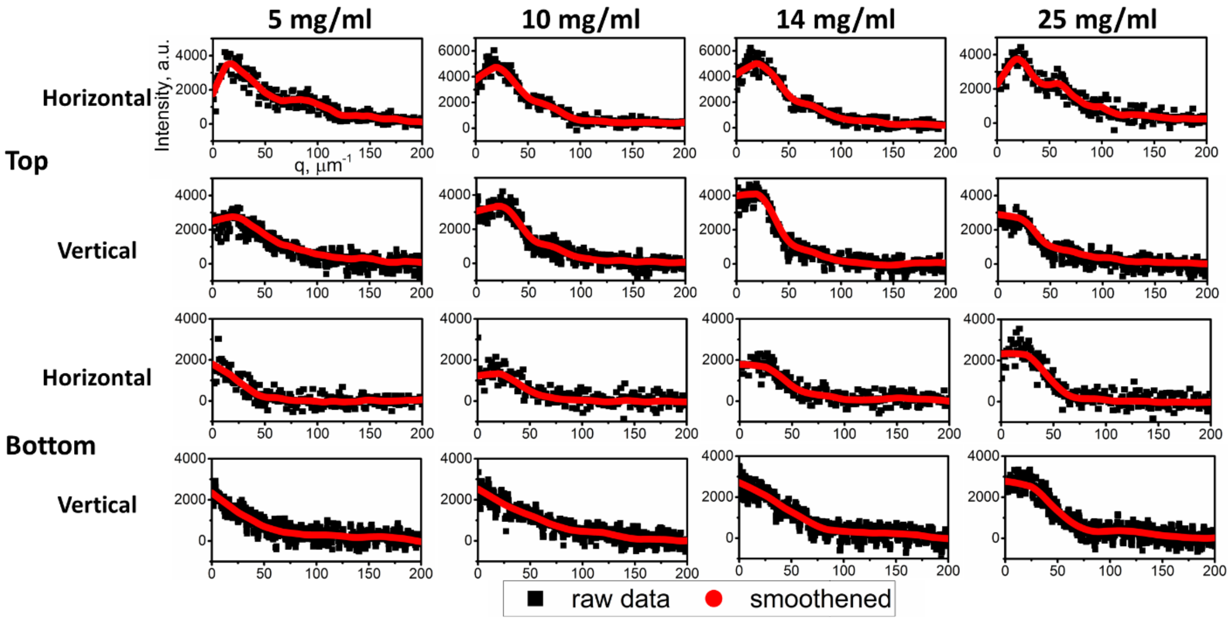

Figure B7. Raw and smoothened data from line-cuts along the horizontal (perpendicular to coating) and 5° offset with the vertical (parallel to coating) directions on the FFT images for top and bottom scans.

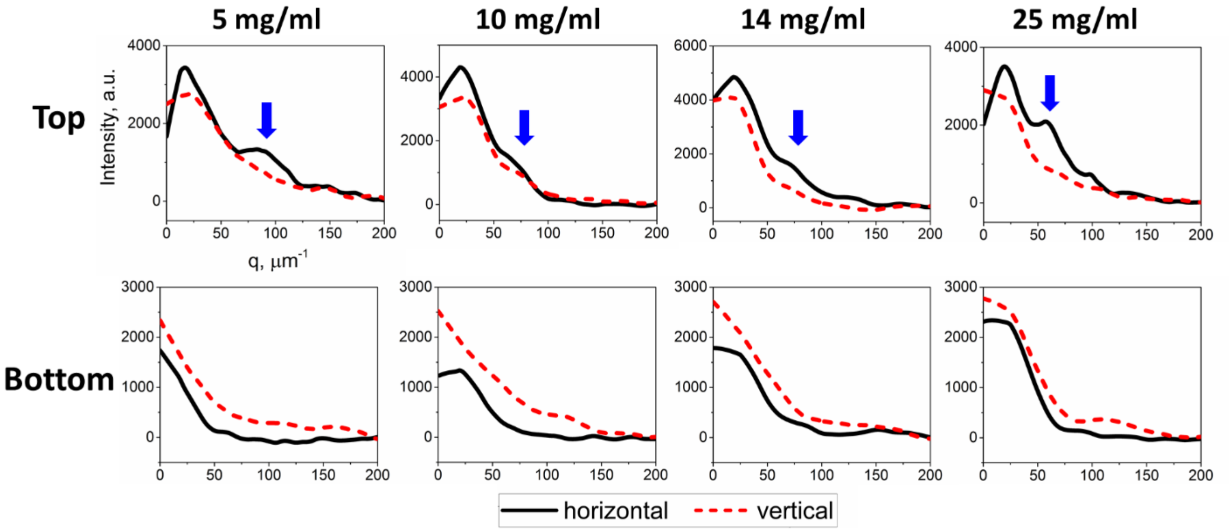

Figure B8. Overlay of the smoothened linecuts for top and bottom FFT images comparing horizontal vs. vertical intensity profiles. The 2nd order peaks in the top linecuts are indicated with the arrows.

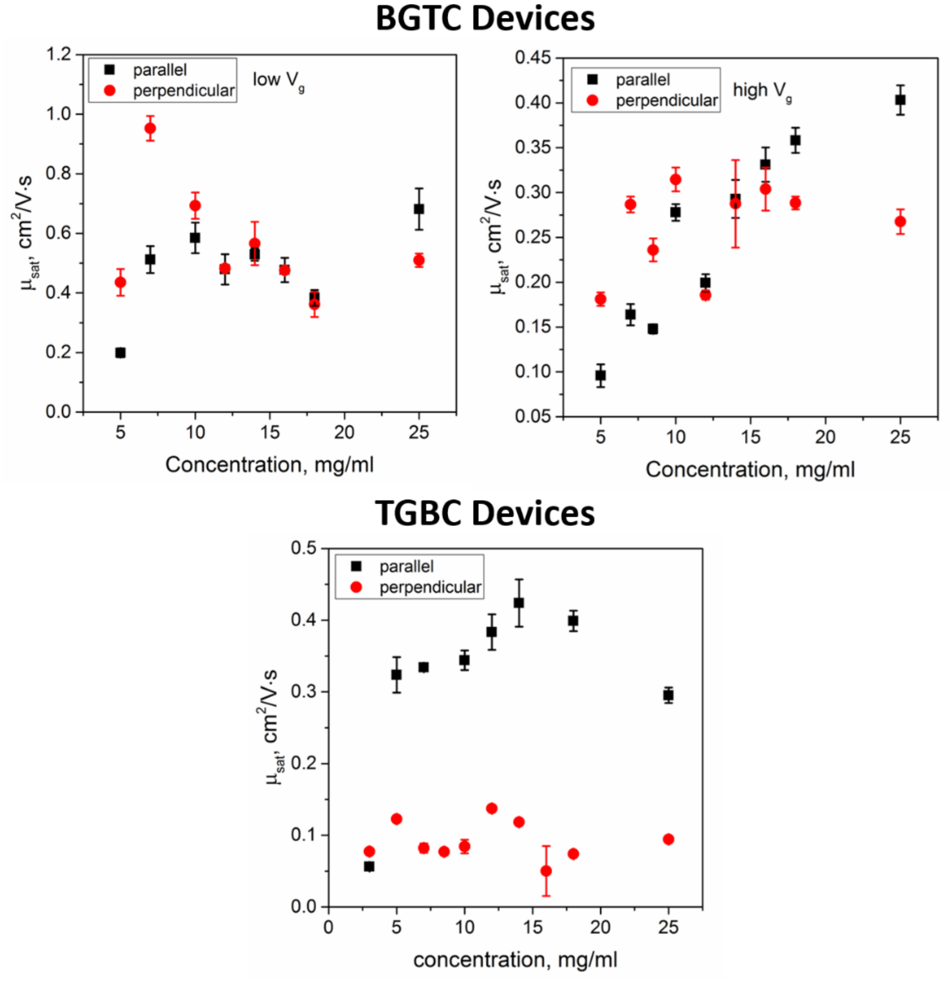

Figure B9. FET device measurements in the saturation regime in the parallel and perpendicular orientations for BGTC configuration (conductive channel at the bottom film-substrate interface) and TGBC configuration (conductive channel at the top air-film interface). For BGTC configuration, apparent mobilities were extracted at both low Vg (20 – 50 V) and high Vg (60 – 90 V).

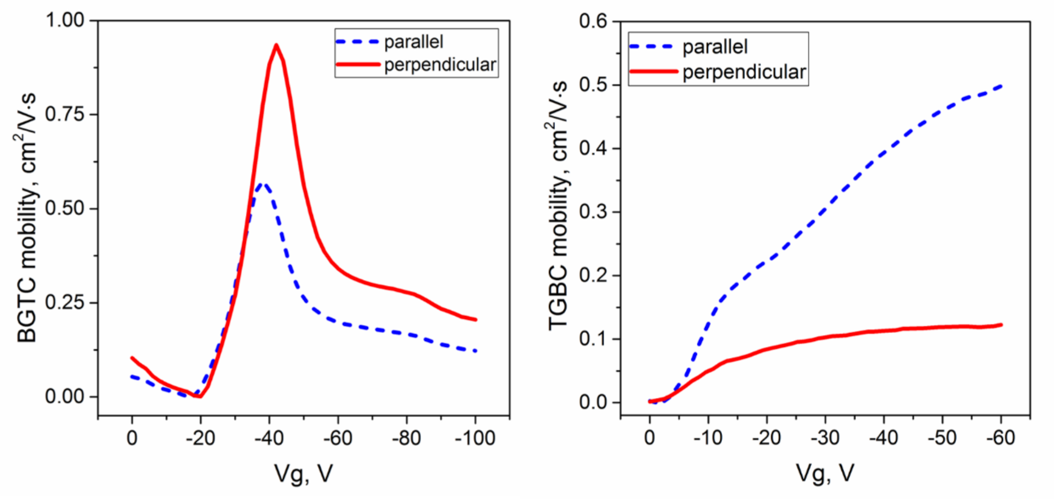

Figure B10. FET device mobility versus Vg for BGTC devices on films printed from 7 mg/ml solution and TGBC devices on films printed from 14 mg/ml solution.

Peclet number calculation.

The Peclet number is a dimensionless number comparing convective mass transport with diffusive mass transport. In our case we can compare the solvent evaporation rate with the solute diffusion rate to qualitatively understand which process is dominant. If the evaporation is dominant, the evaporation at the meniscus can induce a concentration gradient of the solute because the diffusion rate of solute is not fast enough to remove the solute from the high concentration regions. If the solute diffusion is dominant, the solute diffusion is able to remove solution from the meniscus front when the solvent is evaporating, creating an even distribution of concentration within the liquid. For this calculation, we assumed Pe to be constant across the meniscus, which may not reflect the actual distribution as both the evaporation rate and viscosity increases, while the liquid layer thickness decreases moving closer to the contact line. However, due to limited information, we cannot directly estimate Pe at the meniscus front. Accurate Peclet number calculation requires the knowledge of liquid layer thickness, evaporation rate and viscosity near the contact line, which could be simulated using coupled physics and finite element methods which will be pursued in subsequent studies.

The equation used for calculating Peclet number initially describes the geometry in a thin droplet[4]:

$$Pe = \frac{Eh_0}{D} \qquad \text{(Eqn. B2)}$$

where E is the evaporative flux of the solvent in volume per time per unit area, h_0 is the thickness of the droplet and D is the diffusion coefficient of the solute in the solvent. The evaporation rate of the solvent defined by Le Berre is shown in the caption of Figure S1 for evaporation rate calculation[1]:

$$Q_{evap} = \frac{h\rho L v}{C} \qquad \text{(Eqn. B3)}$$

where h is the thickness of the film, ρ is the density of the solute, L is the width of the meniscus, ν is the speed of the moving blade or substrate and C is the concentration of solute in the solvent. In this equation, Q_{evap} is the evaporation rate in volume per time. Therefore,

$$Q_{evap} = ES \qquad \text{(Eqn. B4)}$$

where S is the area of the meniscus. If we define that *l* is the contour length of the meniscus, we have

$$Pe = \left[\frac{\rho v h_0}{lD}\right]\frac{h}{C} \qquad \text{(Eqn. B5)}$$

that the coefficients in the brackets are all constants, and the film thickness h and the solution concentration C are varying based on the experimental condition.

The blade velocity is 0.5 mm/s. The liquid thickness is 100 μm which the gap size between the substrate and the blade. The contour length of the meniscus is 117 μm based on the meniscus geometry. The density of DPP2T-TT is assumed to be in the range of 1-1.3 g/cm^3, or around 1.15 g/cm^3. The diffusion coefficient is 1×10^{-6} cm^2/s estimated with a rigid rod modal developed by Tirado and coworkers.[5] The dimension of the rod used for calculation is from SANS measurement with 7 mg/ml DPP2T-TT in chloroform solution, resulting in 28 nm cylinder length and 1.7 nm diameter. Substituting the slope from Figure S1 $\frac{h}{C} = 6.7\,\frac{nm}{mg/cm^3}$ we can obtain the average Peclet number for all concentrations as Pe = 33 (Pe = 28.5-37.2 using 1-1.3 g/cm^3 DPP2T-TT density).

The higher value of the Peclet number indicates that, under the experimental conditions tested, evaporation of the solvent will be dominant and the DPP2T-TT solute can accumulate near the top interface of the meniscus. Therefore we hypothesize that crystalline DPP2T-TT fibers may form near the top interface first, inhibiting the crystallization in the bulk.

Diffusion coefficient calculation.

The translational diffusion coefficient for rod-shaped DPP2T-TT polymer was calculated using the model proposed by Tirado and coworkers.[5] The translational diffusion coefficient for rod was defined for diffusion with two types of rod orientations: rod parallel to flow $D_t^{\parallel}$ and rod orthogonal to flow $D_t^{\perp}$. The equations are:

$$D_t^{\parallel} = \frac{k_B T}{2\pi\eta_0 L}\left(lnp - 0.114 - \frac{0.15}{ln2p} - \frac{13.5}{(ln2p)^2} + \frac{37}{(ln2p)^3} - \frac{22}{(ln2p)^4}\right) \qquad \text{(Eqn. B6)}$$

$$D_t^{\perp} = \frac{k_B T}{4\pi\eta_0 L}\left(lnp + 0.866 - \frac{0.15}{ln2p} - \frac{8.1}{(ln2p)^2} + \frac{18}{(ln2p)^3} - \frac{9}{(ln2p)^4}\right) \qquad \text{(Eqn. B7)}$$

where T is ambient temperature 300K, η_0 is the viscosity of chloroform 0.00053 Pa·s, L is the rod length 28 nm, p is the aspect ratio L/d 16.5. The calculated values are $D_t^{\parallel} = 1 \times 10^{-6}$ cm^2/s and $D_t^{\perp} = 7.4 \times 10^{-7}$ cm^2/s. To avoid over-estimation of the Peclet number, $D_t^{\parallel}$ was used in the calculation.

Vorticity discussion.

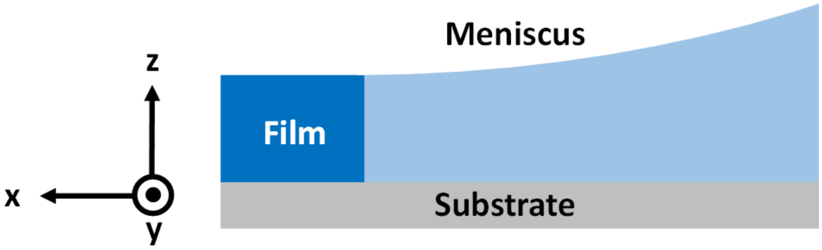

Figure B11. Geometry for meniscus guided coating near the contact line

For the meniscus guided coating geometry, relevant orientations can be defined in the Cartesian coordinate with x along the coating direction, y along the contact line (orthogonal to coating) and z orthogonal to the substrate plane. For vorticity, the vorticity tensor can be decoupled into the x,y,z directions.

$$\omega_x = \frac{\partial v_z}{\partial y} - \frac{\partial v_y}{\partial z} \qquad \text{(Eqn. B8)}$$

$$\omega_y = \frac{\partial v_x}{\partial z} - \frac{\partial v_z}{\partial x} \qquad \text{(Eqn. B9)}$$

$$\omega_z = \frac{\partial v_y}{\partial x} - \frac{\partial v_x}{\partial y} \qquad \text{(Eqn. B10)}$$

For the ω_x component, $v_y = 0$ due to 2D symmetry and v_z does not vary with y. Therefore $\omega_x = 0$. Similarly, for the ω_z component, $v_y = 0$ and v_x does not vary with y. Therefore $\omega_z = 0$. The only non-zero vorticity tensor is ω_y. The first term $\frac{\partial v_x}{\partial z}$ is the shear strain rate caused by the non-slip boundary condition. The shear strain rate is the highest at the liquid-substrate boundary and gradually decreases from substrate to meniscus because of the zero shear boundary condition at the free surface with $\frac{\partial v_x}{\partial z} = 0$. We assume that v_z is close to zero near the contact line due to lubrication approximation.[6] In this case vorticity tensor ω_y is only influenced by the shear strain rate, with highest value near the substrate and lowest value at the free surface.

References

1. Le Berre, M.; Chen, Y.; Baigl, D., From Convective Assembly to Landau-Levich Deposition of Multilayered Phospholipid Films of Controlled Thickness. *Langmuir* **2009,** *25*, 2554-2557.

2. Guinier, A.; Fournet, G., *Small-Angle Scattering of X-Rays*. Wiley: New York, 1955.

3. Newbloom, G. M.; Hoffmann, S. M.; West, A. F.; Gile, M. C.; Sista, P.; Cheung, H.-K. C.; Luscombe, C. K.; Pfaendtner, J.; Pozzo, L. D., Solvatochromism and Conformational Changes in Fully Dissolved Poly(3-Alkylthiophene)S. *Langmuir* **2015,** *31*, 458-468.

4. Pauchard, L., Droplets of Polymers. In *Droplet Wetting and Evaporation*, Academic Press: Oxford, 2015; pp 339-350.

5. Tirado, M. M.; Martínez, C. L.; Torre, J. G. d. l., Comparison of Theories for the Translational and Rotational Diffusion Coefficients of Rod‐Like Macromolecules. Application to Short DNA Fragments. *J. Chem. Phys.* **1984,** *81*, 2047-2052.

6. Doumenc, F.; Guerrier, B., Drying of a Solution in a Meniscus: A Model Coupling the Liquid and the Gas Phases. *Langmuir* **2010,** *26*, 13959-13967.

Appendix C. Detailed X-ray Results, Deposit Morphology Characterization and High Speed Video Analysis for Morphology Transition Study

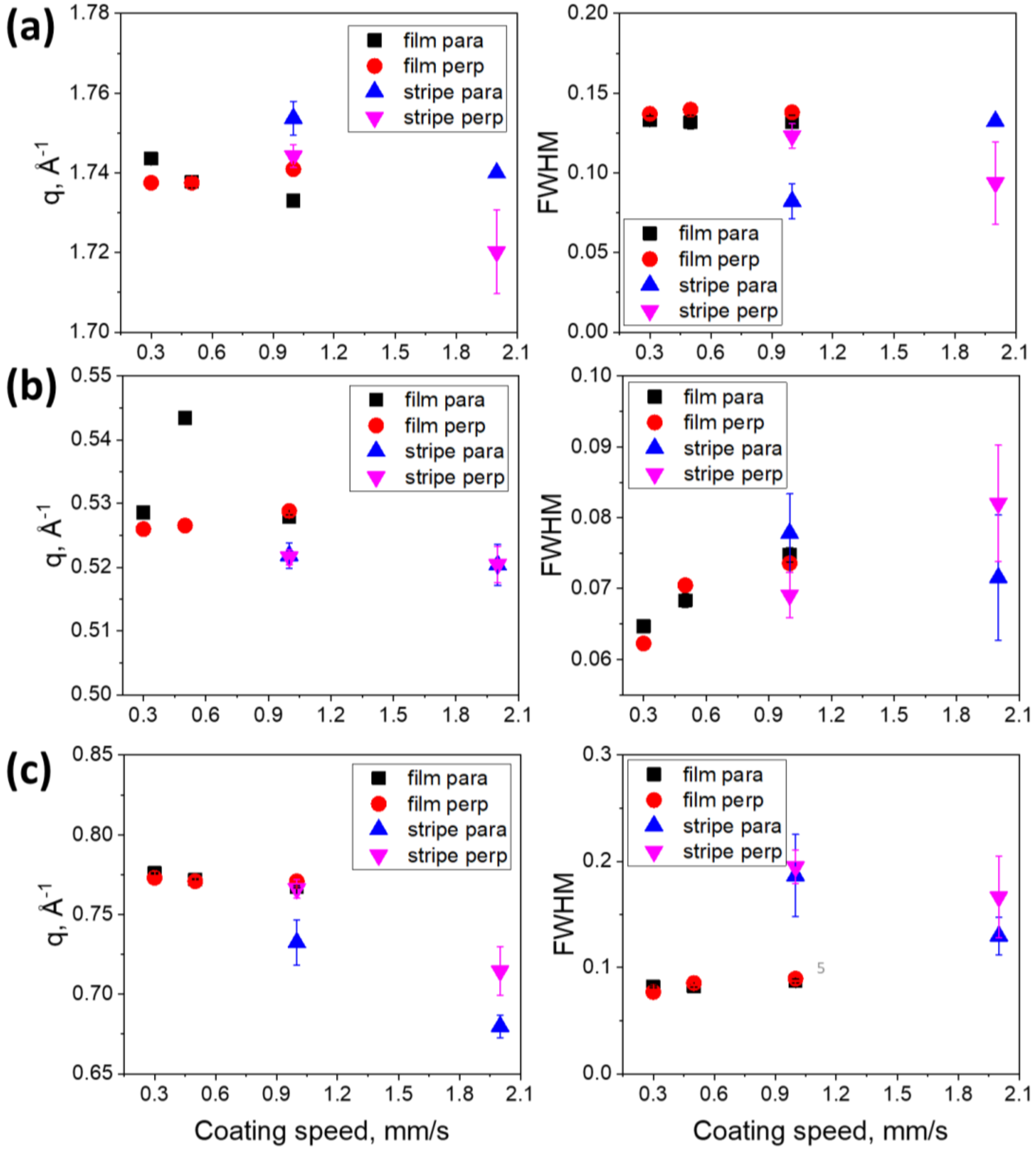

Figure C1. Reciprocal q spacing and full width at half maximum for (a) (010) in-plane π-π stacking peaks, (b) (200) and (c) (300) out-of-plane lamellar stacking peaks.

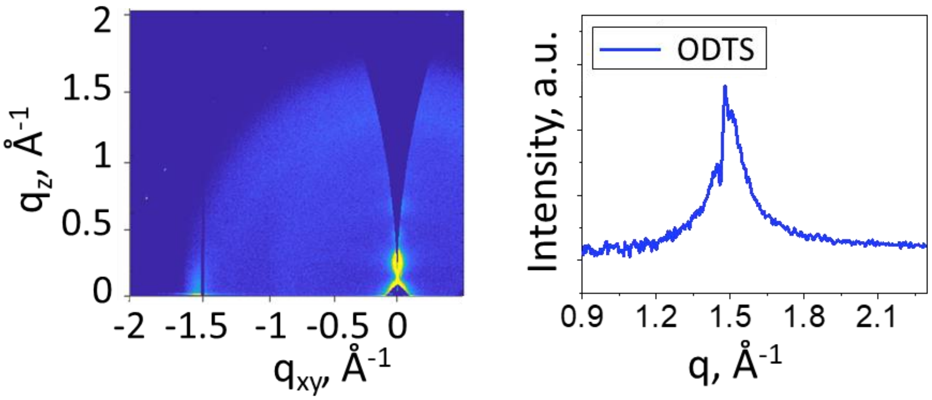

Figure C2. GIWAXS diffraction pattern of ODTS on 300 nm SiO_2 substrate and 5° sector cut of in-plane ODTS peak for background subtraction.

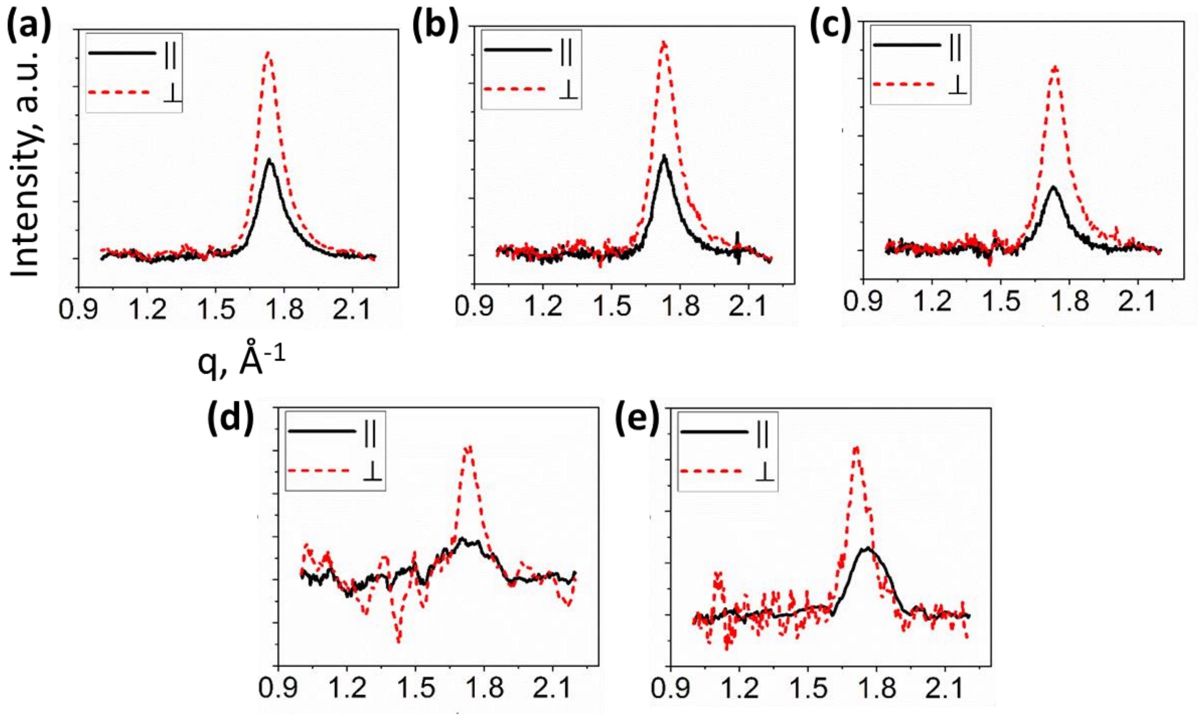

Figure C3. 5° sector cut of in-plane π-π stacking peaks for DPP2T-TT deposit at (a) 0.3 mm/s film, (b) 0.5 mm/s film, (c) 1 mm/s film, (d) 1 mm/s stripe and (e) 2 mm/s stripe

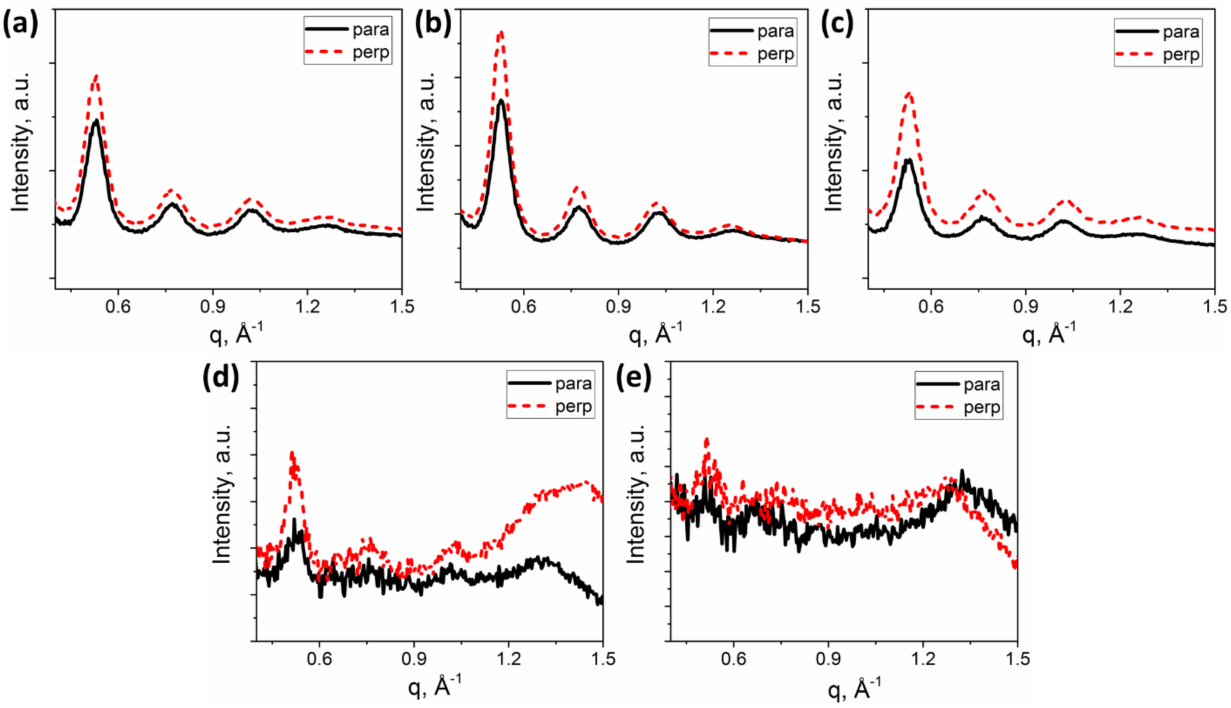

Figure C4. 5° sector cut of out-of-plane lamellar peaks for DPP2T-TT deposit at (a) 0.3 mm/s film, (b) 0.5 mm/s film, (c) 1 mm/s film, (d) 1 mm/s stripe and (e) 2 mm/s stripe

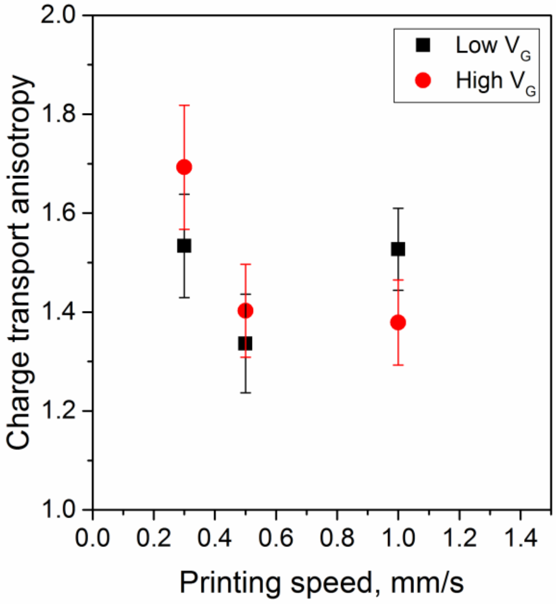

Figure C5. Charge transport anisotropy of perpendicular over parallel mobility for films coated at different speed.

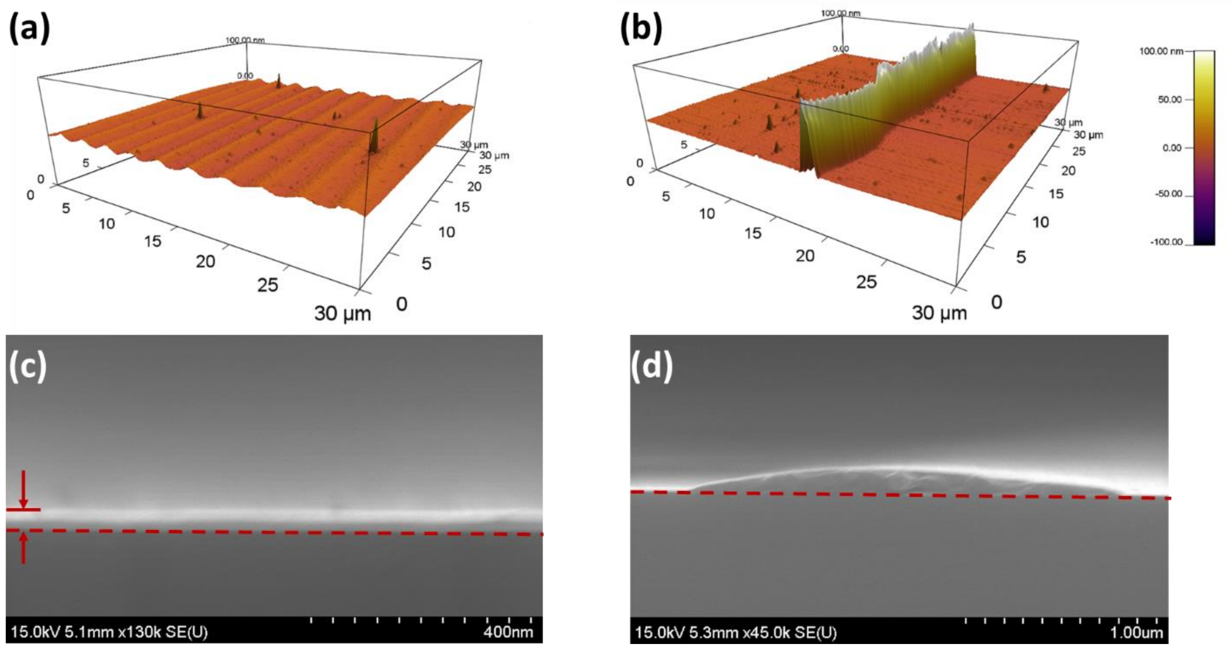

Figure C6. AFM measured height profile of (a) film surface undulation coated from 0.9 mm/s and (b) a stripe coated from 1.5 mm/s. SEM measured cross-section of (c) film coated from 0.9 mm/s and (d) a stripe coated from 1.5 mm/s.

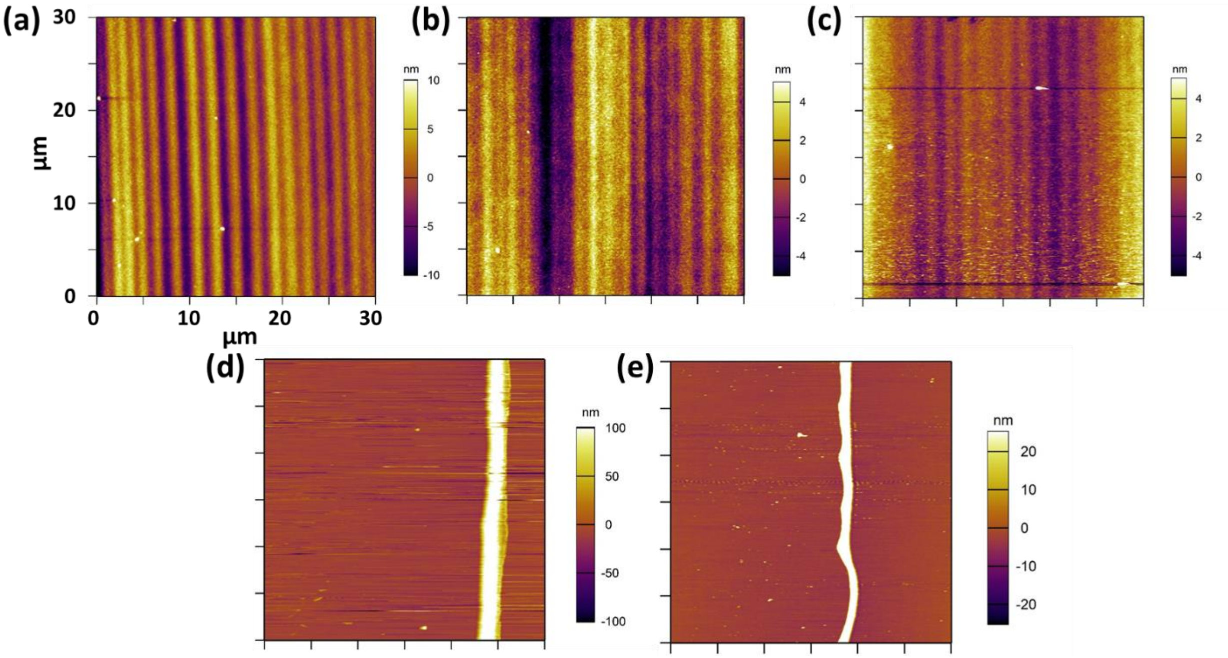

Figure C7. AFM images of (a) film coated from 0.5 mm/s, (b) film coated from 0.8 mm/s, (c) film coated from 0.9 mm/s, (d) strip coated from 0.9 mm/s and (e) stripe coated from 1.5 mm/s.

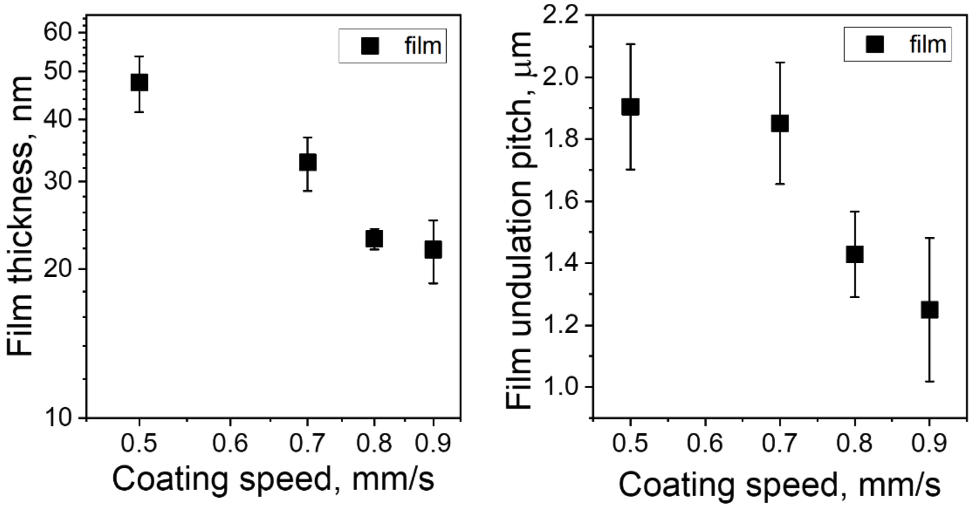

Figure C8. Film thickness and pitch of film undulations from AFM measurements at various coating speed.

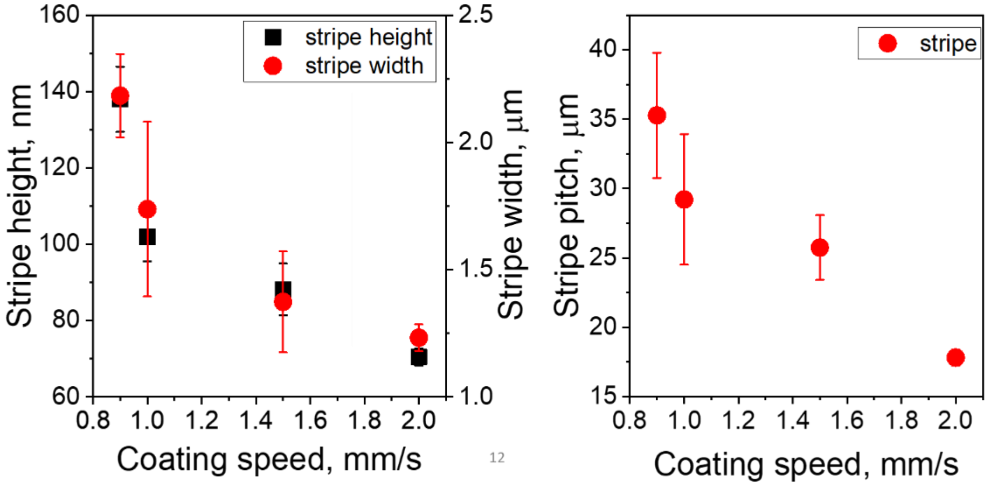

Figure C9. Stripe dimensions from AFM measurements and stripe pitch from microscopy at various coating speeds.

Table C1. Interfacial free energy values and fitted parameter for system surface energy calculations

Component	Interfacial free energy γ	Fitted parameter β
ODTS – air	21±1	$1.27 \pm 0.09 \times 10^{-4}$
DPP2T-TT – air	23±2	$9 \pm 1 \times 10^{-5}$
DPP-BTz	21.6±0.2	$1.08 \pm 0.08 \times 10^{-4}$
PII-2T	21.4±0.5	$1.2 \pm 0.6 \times 10^{-4}$
Chloroform – air	26.7±0.5	
5 mg/ml DPP2T-TT in chloroform solution – air	25.8±0.8	
ODTS – DPP2T-TT	0.07±0.01	
ODTS – solution	0.46±0.06	
DPP – solution	0.15±0.3	

High Speed Video Processing and Analysis.

Image processing for extracting arc length and drag length during meniscus stick and slip was performed with the meniscusfit.m MATLAB code. After exporting the high speed video into a set of individual frames, the range of frames to be processed (i.e. frame 200 – 4000) was input to the code. The value of fps of the video was entered to accurately correlate fitted results for each frame at the corresponding time, which is 1000 for all videos analyzed. Frames were converted into grey scaled figures and then to binary figures with a threshold value, ranging between 0.3 – 0.4 for the analyzed videos. The meniscus threshold underwent trial-and-error to accurately capture the correct shape of the meniscus. The meniscus near the contact line required a different threshold larger than that for the complete meniscus due to decrease in color contrast between the solution and air near the contact line. The contact line threshold was effective within a fixed height from the baseline to ensure smooth transition in meniscus shape near the contact line. Baseline was determined by tracking the flat substrate surface and the meniscus was tracked within the meniscus height (in pixel) where the meniscus was in contact with the blade. The meniscus height was manually determined by obtaining the vertical distance between the substrate baseline and the end of meniscus at the blade from the frames, which remained constant during the horizontal meniscus movement in each coating video. A drag threshold distance was entered to determine the range of base line to avoid mistaking meniscus as the baseline. The drag threshold distance was defined as the horizontal distance on the base line from the point of meniscus in contact with the blade. Because the horizontal length of the meniscus, as defined as drag length, was near 50 pixel for all conditions, the used drag threshold distance ranged within 50 – 70 pixels. Therefore baseline tracking would stop before meeting the meniscus to avoid obtaining inaccurate baseline. The reflective substrate gave rise to a shadow of the meniscus near the contact line, so a fuzz value was included to avoid tracking the shadow of the meniscus. The fuzz value was determined as the vertical distance between the tracked substrate base line and the position of the meniscus contact line, also remained a constant during blade movement. A frame of the meniscus side view with labeled lengths for processing was shown in **Figure C7a**.

After determining all necessary parameters, the MATLAB code was run to batch process a set of frames from one coating condition. Arc length and drag length at during the stick-and-slip motion for both film deposition and stripe deposition was obtained, example illustrated in **Figure C10b**. Due to the high frequency in film deposition and the limited frame rate, only 2-3 frames were included for each stick-and-slip cycle for film deposition. Are length and drag length for S1 and S2 were obtained by extracting local maxima and minima from the data set. For stripe deposition, distinct sticking and slipping of the meniscus reflected in the change in arc length and drag length was observed. Therefore manual recording of arc length and drag length was performed for stripe deposition. Length conversion was performed by measuring gap size (100 μm) in pixels on the frames for each coating condition and converting obtained arc length and drag length from pixels to μm. Extracted arc length and drag length for all coating conditions were include in **Table C2.** The deposit dimensions from AFM, arc length and drag length from high speed video analysis and the interfacial free energy data from droplet measurements were substituted into the system surface energy model, with the calculated system surface energy in **Table C3**.

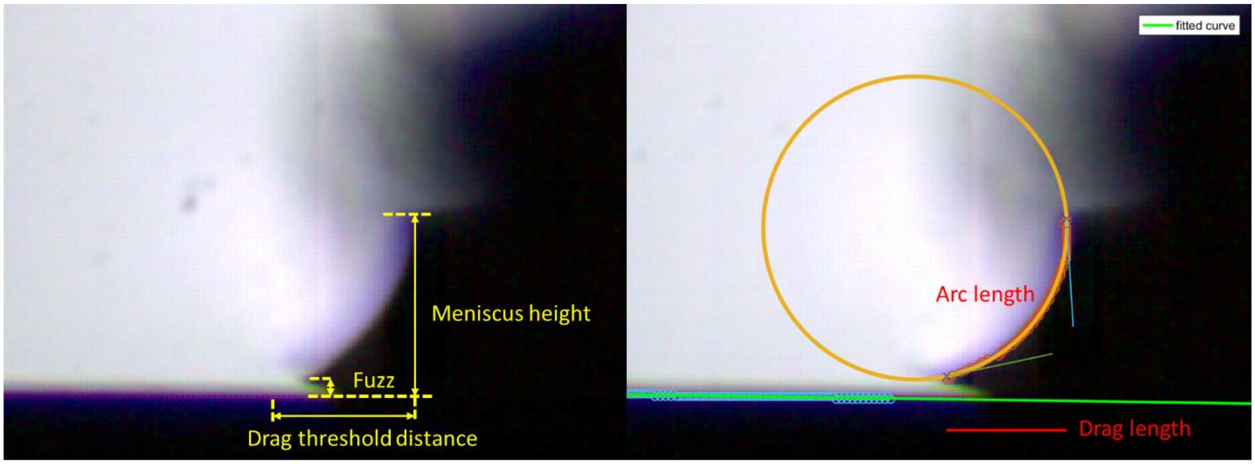

Figure C10. (a) Illustration of meniscus side view from 2 mm/s coating video with parameters for meniscus fitting. (b) Fitted meniscus for arc length and drag length extraction at 2 mm/s coating.

Table C2. Extracted arc length and drag length from solution coating videos.

	a_{f1}, µm	d_{f1}	a_{f2}	d_{f2}	a_{s1}	d_{s1}	a_{s2}	d_{s2}
0.5 mm/s	178±1	81±1	176±1	80±1				
0.7 mm/s	203±2	110±3	200±9	108±3				
0.8 mm/s	220±2	130±2	218±2	128±3				
0.9 mm/s	232±2	126±5	230±2	124±4	221±2	95±3	206±2	78±4
1 mm/s					195±2	58±3	184±2	46±3
1.5 mm/s					193±3	62±6	179±2	44±2
2 mm/s					213±3	116±6	192±4	92±3

Table C3. System surface energy for all coating conditions

	$G_{max,f}$, μJ/m	$G_{min,f}$, μJ/m	$G_{max,s}$, μJ/m	$G_{min,s}$, μJ/m
0.5 mm/s	4.6±0.1	4.6±0.2		
0.7 mm/s	5.3±0.2	5.2±0.1		
0.8 mm/s	5.7±0.2	5.7±0.2		
0.9 mm/s	6.0±0.2	6.0±0.2	5.8±0.2	5.3±0.2
1 mm/s			5.1±0.2	4.7±0.2
1.5 mm/s			5.0±0.2	4.6±0.2
2 mm/s			5.6±0.2	5.0±0.2

Appendix D. Characterization for Morphology Number Calculation for Generalized Morphology Study

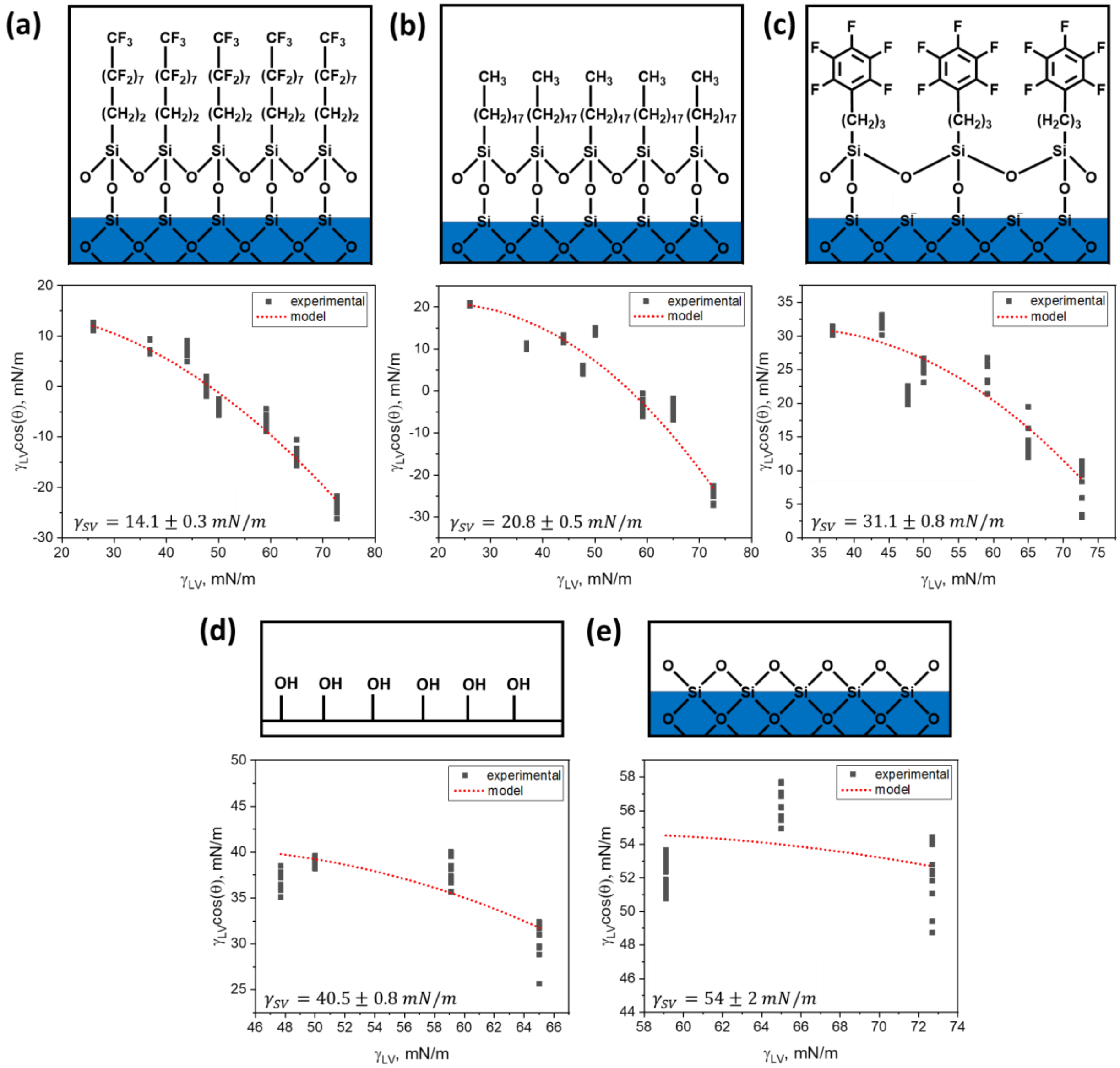

Figure D1. Substrate molecular structure and surface energy measurement results for (a) HTMS, (b) OTS, (c) FPTS, (d) PVOH and (e) SiO_2.

Table D1. Probing liquid and their surface energy used for substrate surface energy measurements.

Component	1-penthanol	[EMIM][TFSI]*	dimethyl sulfoxide	Ethylene glycol
Surface energy, mN/m	26.0	36.9	44.0	47.7
Component	diiodomethane	formamide	glycerol	water
Surface energy, mN/m	50.0	59.1	65.0	72.7

*[EMIM][TFSI] full name: 1-Ethyl-3-methylimidazolium bis(trifluoromethylsulfonyl)imide

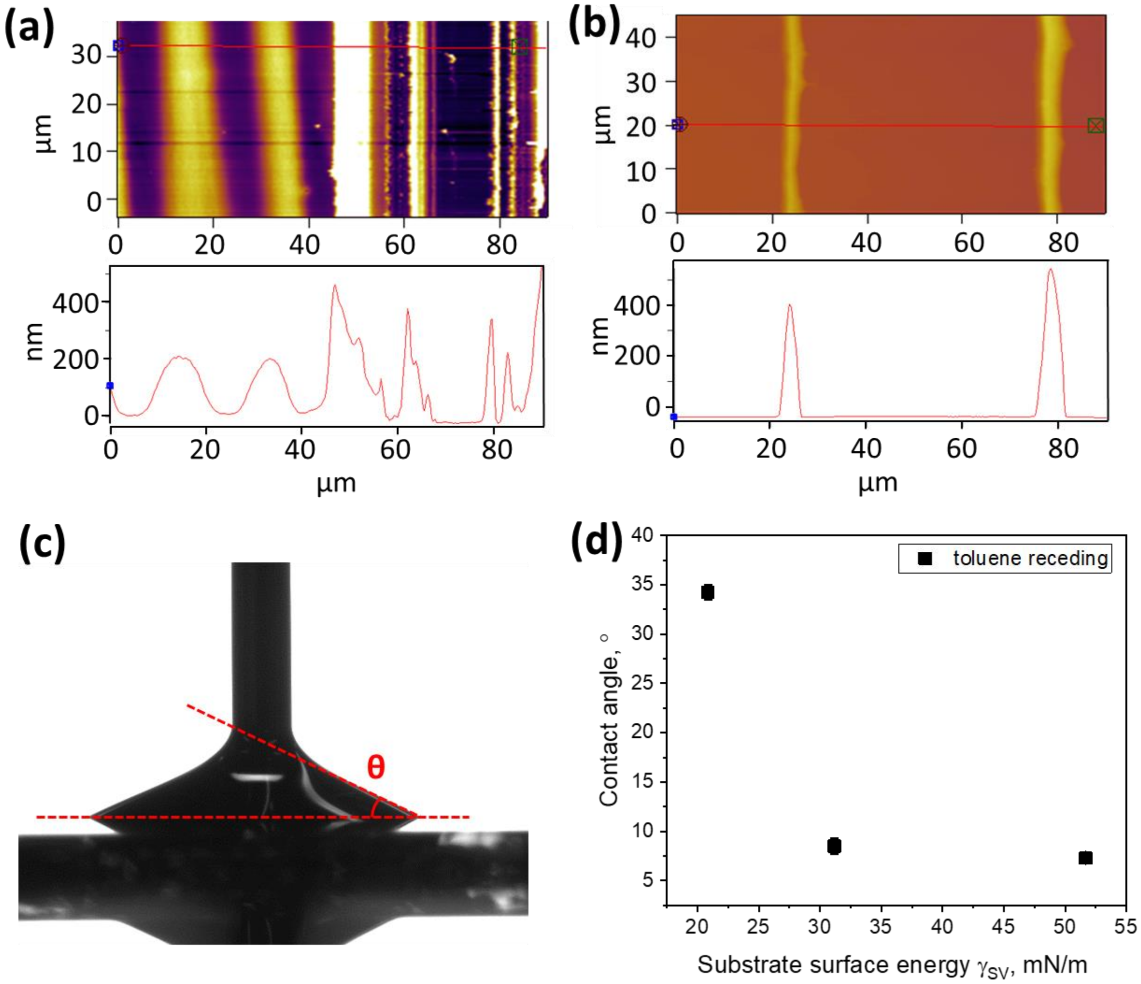

Figure D2. Example AFM measurement height contour images and cross section profiles for (a) film and (b) stripe measurments. (c) Receding contact angle measurement with microsyringe needle in the droplet and (d) receding contact angle results on OTS, FPTS and SiO_2.